

**STUDY OF TEMPERATURE CHARACTERISTICS
OF 1.3 μm STRAIN-LAYER MULTIPLE QUANTUM
WELL LASERS**

by

**Rong(Ron) Huang
B.Eng., M.Sci., M.Eng.**

**A Thesis
Submitted to the School of Graduate Studies
in Partial Fulfilment of the Requirements
for the Degree
Doctor of Philosophy**

**McMaster University
© Copyright by Rong Huang
January, 1997**

**STUDY OF TEMPERATURE CHARACTERISTICS
OF 1.3 μm STRAIN-LAYER MULTIPLE QUANTUM
WELL LASERS**

**STUDY OF TEMPERATURE CHARACTERISTICS
OF 1.3 μm STRAIN-LAYER MULTIPLE QUANTUM
WELL LASERS**

by

RONG(RON) HUANG, B.Eng., M.Sci., M.Eng.

Doctor of Philosophy(1997)
(Engineering Physics)

McMaster University
Hamilton, Ontario

Title: STUDY OF TEMPERATURE CHARACTERISTICS
 OF 1.3 μm STRAIN-LAYER MULTIPLE
 QUANTUM WELL LASERS

AUTHOR: Rong Huang, B. Eng., M. Sci., M. Eng.

SUPERVISORS: Professor J.G. Simmons
 Professor P.E. Jessop

NUMBER OF PAGES: xii, 141

ABSTRACT

This thesis presents a theoretical and experimental study of the temperature characteristics of 1.3 μm strained layer multiple quantum well (MQW) lasers over a wide temperature range. A number of achievements have been made toward understanding the temperature sensitivity of the performance of the lasers.

Under assumptions that the deterioration of optical gain with temperature dominates the temperature sensitivity of the laser performance and that the differential gain coefficient decreases linearly with temperature, two formulae, which include a maximum operating temperature, were derived to describe the threshold current, I_{th} , and the external quantum efficiency, η_{d} , as functions of temperature. The formulae produce a very good fit to the experimental data that were extracted from the short-pulse L-I characteristics of 1.3 μm 0.7% compressive strained layer MQW lasers containing varying number of wells. The maximum operating temperatures obtained from fitting the formulae to I_{th} vs. T and η_{d} vs. T data are consistent with each other, which experimentally supports the theory and the underlying assumptions. Based on the same assumptions, the conventional method of determining the internal quantum efficiency and internal loss from a set of lasers with different length was scrutinized. It was concluded that the internal quantum efficiency is a function of temperature, even if the true internal quantum efficiency is independent of temperature, and that the internal loss is a sublinear function of temperature around room temperature, as available experimental results show. The experimental results from 1.3 μm ten 0.7%

compressively strained wells lasers with varying cavity length support the theoretical conclusions.

The experimental observation of the far-field patterns for 1.3 μm 1.2% tensile strained layer MQW lasers containing 3 wells with varying ridge width over a wide temperature range indicated that the injected carriers exert little effect on the refractive index, and that the change in the far field distribution with temperature is the result of spatial hole-burning.

The final part of this thesis presents a technique to determine the temperature rise of the lasers during CW operation, which was then used to calculate the thermal impedances of different ridge width lasers. It was concluded that a wider ridge laser has a smaller thermal impedance and a lower available CW maximum operating temperature.

Table of Contents

Chapter 1: Introduction	1
1.1 Background	1
1.2 Material Covered in this Thesis	4
Chapter 2: Experimental Procedure and Laser Structure.....	7
2.1 Introduction	7
2.2 Experimental Set-ups in Pulse Mode.....	8
2.2.1 Set-up for L-I measurement	8
2.3.2 Set-up for Far Field Measurement	14
2.3.3 Set-up for Spectrum Measurement	14
2.3 Set-ups for CW Measurement	17
2.4 Computer Program Used for System Control	19
2.5 Laser Structures	20
Chapter 3: Temperature Dependence of Threshold Currents	25
3.1 Introduction	25
3.2 Temperature Dependence of Threshold Current	25
3.3 Theoretical Analysis of the Dependence of Threshold Current on Temperature	30
3.4 Experimental Results and Discussion	36
3.4.1 Experimental Characterization under CW Operation	37
3.4.2 Experimental Results under Pulse Operation	39
3.5 Conclusions	43
Chapter 4: Temperature Sensitivity of External Quantum Efficiency	45
4.1 Introduction	45
4.2 Theoretical Analysis of External Quantum Efficiency	46
4.3 Experimental Results and Discussion	47

4.4	Conclusions	54
Chapter 5: Internal Quantum Efficiency and Internal Loss		55
5.1	Introduction	55
5.2	Theoretical Analysis of Internal Quantum Efficiency and Internal Loss	57
5.3	Experimental Results and Discussion	59
5.4	Conclusions	63
Chapter 6: Experimental Observation of Far Field Patterns of 1.3μm Tensile SL-MQW Lasers with Varying Ridge Width		64
6.1	Introduction	64
6.2	Experimental Concern	65
6.3	Theoretical Slab Waveguide Analysis	66
	6.3.1 Theoretical Description of Laser Cavity Modes	67
	6.3.2 Theoretical Description of Far Field Of a Laser	71
6.4	Theoretical Calculation of Internal Cavity Modes and Far Fields.....	76
6.5	Experimental Results and Discussion	83
	6.5.1 Far-field Observation	83
	6.5.2 Spectral Measurement of the Lobes of the Far-field	90
	6.5.3 Theoretical Construction of the Far-field Pattern	92
6.6	Conclusions	94
Chapter 7: Thermal Run-away under CW Operation and Thermal Impedance		95
7.1	Introduction	95
7.2	A theoretical Model for Temperature Measurement during CW operation	97
7.3	Temperature Rise during CW operation	99
	7.3.1 Light-Current Characteristics under CW Operation.....	100
	7.3.2 I-V Characteristics under CW operation at Various Temperature	104
	7.3.3 Temperature Dependence of Threshold Current and External Quantum Efficiency	111
	7.3.4 Thermal Impedance of Different Ridge Width Lasers	117

7.4	Conclusions	120
Chapter 8: Conclusions		122
Appendix		125
A.1	Band Gap Of InGaAsP	125
A.2	Energy Correction Induced by Strain	127
A.3	Approximate Expression of Band Position	127
A.4	A Computer Program for Calculation of Quantum Well Composition	128
References		133

List of Figures

<u>Figures</u>	<u>Pages</u>
2.2.1 Schematic experimental set up for pulse measurements.	9
2.2.2 The relationship of the gate signal and the signal from the detector	10
2.2.3 The calibration curve for the laser current source in pulsed mode.	11
2.2.4 The laser assembly	13
2.2.5 The designed heating unit.	13
2.2.6 The set-up for far field measurement	15
2.2.7 The set-up used for the optical spectrum measurement	16
2.3.1 Typical L-I curves for a 10 wells 0.7% compressive SL-MQW lasers obtained using the illustrated CW set-up	17
2.3.2 The se-up for the CW measurement	18
2.5.1 The laser structure for 5 to 14 wells 0.7% compressive SL-MQW InGaAsP/InP lasers.	20
2.5.2 The laser structure for 1.2% tensile SL-MQW lasers containing 3 quantum wells. The wells are 80Å wide and the barriers 200Å thick.	21
2.5.3 Schematic illustration of band structure with (a)tensile strain, (b)no strain, and (c)compressive strain	22
2.5.4 The cross-section of the ridge waveguide lasers used in thesis	23
2.5.5 The measured far fields at 110K and 350K. The temperature has a little effect on the far field pattern.	24
3.2.1 Schematic diagram of the change in the optical gain vs. carrier density as a function of temperature.	28
3.3.1 Extracted differential gain coefficient versus temperature [Ackerman, 1995].	32
3.4.1 A room temperature optical spectrum of a compressive SL-MQW laser, which contains 10 quantum wells and is 500µm long	36
3.4.2 The L-I curves for 0.7% compressive SL-MQW laser contained 5 wells under CW operation.	37
3.4.3. The maximum operation temperature vs. the number of wells under CW operation	38
3.4.4 Typical L-I curves for a 500µm long 10 wells 0.7% compressive strain InGaAs/InP laser under pulse operation(100ns @ 10KHz)	39
3.4.5. The experimental threshold current vs. temperature data of 500µm long 0.7% compressive SL-MQW lasers ranging in well number from 5 to 14	40

3.4.6	The experimental results of the threshold current with temperature for 14 wells compressive SL-MQW lasers with variant cavity length	41
3.4.7	The length dependence of the threshold currents for 14 wells compressive SL-MQW lasers at various temperatures with the linear fitting lines	42
3.4.8	T_{\max} as a function of cavity length for the different length 14 0.7% compressively SL-MQW lasers	43
4.3.1	η_d vs. T and I_{th} vs. T for 5 well(a), 6 wells(b), 8 wells(c), 10 wells(d), 12 wells(e) and 14 wells(f)	51
4.3.2	T_{\max} deduced from η_d vs. T and I_{th} vs. T experimental data	52
4.3.3	A schematic illustration of the determination of I_{th} and η_d by the conventional method, with and without heating	53
5.3.1	The I_{th} vs. T and η_d vs. T for 500 μm , 750 μm , and 1000 μm 10 0.7% compressively SL-MQW lasers	59
5.3.2	The length dependence of T_{\max} .	61
5.3.3	The total internal loss for 0.7% compressive SL-MQW laser containing ten wells.	61
5.3.6	η_i^N vs. T for lasers with ten 0.7% compressive strain quantum wells	62
6.2.1	The far field patterns measured at room temperature with and without quartz window at several driving currents for 1.3 μm tensile strain three-well 16 μm wide ridge waveguide laser	66
6.3.1	The slab waveguide structure.	69
6.3.2	The relation of the far field and the internal cavity mode electrical field distribution	73
6.4.1	The vertical mode intensity distribution inside and outside ridge	77
6.4.2	The calculated internal cavity modes and their corresponding far field patterns for (a)2 μm , (b)4 μm , (c)8 μm , (d)16 μm , and (e)32 μm wide ridge waveguide lasers	82
6.5.1	The measured two dimensional far field pattern for 16 μm wide ridge waveguide, 1.3 μm tensile strain MQW laser operating at 110K.	83
6.5.2	The measured two dimensional far field pattern for 16 μm wide ridge waveguide, 1.3 μm tensile strain MQW laser operating at 300K.	84
6.5.3	The experimentally observed far field patterns for 1.3 μm tensile SL-MQW (a)2 μm , (b)4 μm , (c)8 μm , (d)16 μm , and (e)32 μm ridge width at different temperatures	88
6.5.4	The far field pattern for 32 μm wide ridge waveguide tensile strain MQW laser at 110K at different driving currents	89
6.5.5	Calculated and experimentally measured full width at half maximum vs. inverse ridge width.	90

6.5.6	The optical spectra of (a)right lobe, (b)middle lobe, and (c)left lobe of the far field pattern of a 32 μ m 1.3 μ m tensile SL-MQW laser at room temperature.	92
6.5.7	Constructed far field pattern by proportionately combining the far field patterns of individual internal modes of 16 μ m wide ridge waveguide lasers.	93
7.1.1	Typical L-I curves under CW operation for 1.3 μ m 1.2% three-well tensile SL-MQW laser with 2 μ m ridge width.	96
7.2.1	The schematic illustration of the L-I curve under CW operation and the L-I curve without any heating at temperature T	99
7.3.1	Light-current characteristics for (a)2 μ m, (b)4 μ m, (c)8 μ m, (d)16 μ m, and (e)32 μ m wide ridge waveguide lasers at different temperatures under CW operation	102
7.3.2	Experimental set-up for I-V characterization at varying temperature under CW or pulsed operation	104
7.3.3	The current-voltage characteristics for varying ridge width lasers at different temperatures under CW operation: (a)2 μ m, (b)4 μ m, (c)8 μ m, (d)16 μ m, and (e)32 μ m.	107
7.3.4	The power as a function of driving current delivered to (a)2 μ m, (b)4 μ m, (c)8 μ m, (d)16 μ m, and (e)32 μ m laser diodes at different temperatures	110
7.3.5	Experimentally determined temperature dependence of the threshold current and external quantum efficiency for (a)2 μ m, (b)4 μ m, (c)8 μ m, (d)16 μ m, and (e)32 μ m wide and 375 μ m long 1.3 μ m tensile SL-MQW lasers under 100ns at 10KHz pulses operation	113
7.3.6	The dependence of T _{max} extracted from fitting (3.3.11) to the experimental data on the ridge width	115
7.3.7	The relationship of the threshold current with ridge width at various temperatures.	116
7.3.8	The ridge width dependence of the external quantum efficiency at various temperatures	116
7.3.9	The temperature rise as a function of consumed power during CW operation for (a)2 μ m, (b)4 μ m, (c)8 μ m, (d)16 μ m, and (e)32 μ m lasers	119
A.1	Band lineup of the binary materials which compose InGaAsP.	125

List of Tables

<u>Table</u>	<u>Page</u>
3.4.1 The room temperature T_0 and the T_{\max} for different number well lasers	40
4.3.1 The parameters used in η_d vs. T and I_{th} vs. T fitting for different number well lasers	51
5.3.1 Fitting parameters used for Fig.5.3.1	60
6.4.1 The refractive index of different layer materials	77
6.4.2 The number of guided modes for different ridge width lasers	77
7.3.1 The roll over temperatures for different ridge width tensile SL-MQW lasers under CW operation	103
7.3.2 The fitting parameters for the threshold current and external quantum efficiency by (3.3.11) and (4.2.8)	114
7.3.3 Consumed power P_c , T_{zero} , T_{sub} , and ΔT for different ridge width lasers	120
7.3.4 The average thermal impedance for different ridge width lasers above and below threshold	121
A.I Physical Parameters of InP, InAs, GaP, and GaAs	126
A.II Bandgap nonlinearity parameters	126

Chapter 1

INTRODUCTION

1.1 Background

Semiconductor laser diodes are the key components at the heart of many new high-volume products such as compact disc players, laser printers, and fiber optic communication links. The laser diode has evolved from a simple p-n junction to strained layer multiple quantum well (SL-MQW) structure, which has resulted in the threshold current, which is a major parameter for characterizing the laser diode, being reduced by orders of magnitude. However, the expected improvement of the temperature sensitivity of the laser performance by the introduction of quantum well structures, or even strained-layer quantum well structures, has not been delivered yet [Temkin, 1993], despite occasionally reported successes [Agrawal, 1986]. Consequently, attempts to understand the high-temperature sensitivity of, especially, InP-based long wavelength lasers has attracted considerable research effort [Temkin, 1993] [Evans, 1995].

A low threshold current is desirable in practical applications, such as high power operation and direct modulation. With the improvement of crystal growth technology, the introduction of the quantum well structure, and strained quantum well

structures, the threshold current has been reduced dramatically [Henry, 1993] [Coleman, 1993] [O'Reilly, 1994]. The high-temperature characteristics of long wavelength lasers, however, have not been improved as much as expected [Seki, 1995] [Temkin, 1993]. Considerable efforts have been made to understand the origin of the high temperature-sensitivity of the threshold current in long-wavelength semiconductor lasers. Various mechanisms have been proposed to explain the temperature sensitivity, among which are temperature dependence of the optical gain [O'Gorman, 1992] [Zou, 1993] [Temkin, 1993], temperature dependence of optical absorption loss [Mikhaelashvili, 1994] [Seki, 1995], and leakage of injected carriers into confinement layers due to Auger recombination induced energetic carriers [Yano, 1980, 1981] [Asada, 1983] [Dutta, 1991] [Lui, 1993] [Li, 1995]. All these mechanisms may play a role, but it is not clear which is dominant. For example, recent experimental results [Smowton, 1995] [Hazell, 1996] have shown that higher barrier energy gaps, which should eliminate leakage of the injected carriers into the confinement layer due to thermionic emission, do not improve the high temperature performance.

The first formula to describe the relationship between the threshold current, I_{th} , and temperature, T ,

$$I_{th} = I_0 \exp(T / T_0) \quad (1.1.1)$$

was proposed by Pankove [Pankove, 1968]. Since then, the constant T_0 has been widely accepted as a parameter to characterize the temperature sensitivity of the threshold current. Due to this wide acceptance, much of the work concerning the temperature dependence of semiconductor lasers has centered on finding a physical

explanation for (1.1.1) [Ackerman, 1995] [Lui, 1993], even though in his original article Pankove indicated that “there [was] no explicit demonstration that an exponential dependence [of I_{th}] on temperature should be obtained” from the numerical results of sophisticated physical models [Pankove, 1968]. It has been long known that I_{th} increases with increasing temperature faster than that described by an exponential function, and usually a specific T_0 in (1.1.1) only permits a fit between experiment and theory over a small range of temperature. Indeed, some workers have ascribe several values of T_0 to explain their data over an extended temperature range.

The external quantum efficiency, η_d , is an important parameter for characterizing the laser diode, which determines the power output with increasing driving current, and it decreases with increasing temperature [Seki, 1995]. However, no clear functional relationship with temperature has been developed.

The main objective of the theoretical and experimental investigations of this thesis was to find dominant mechanisms in determining the temperature sensitivity of the laser performance and the functional relationships between the threshold current and temperature and the external quantum efficiency and temperature. Given these objectives, the physical mechanisms proposed by other authors to be responsible for the temperature sensitivity of I_{th} and η_d in InGaAsP/InP bases lasers were examined, and a theoretical analysis and experimental investigation was carried out. Another point that has generally not been addressed is that most studies determined η_d and I_{th} from continuous wave (CW) measurements. We will show in the thesis that CW measurements can give rise to significant rise in temperature of the active region of the laser, which means that the intrinsic values of I_{th} and η_d are not being measured. We address the problem by using short pulse technique, which minimizes heating in the active region.

1.2 Materials Covered in This Thesis

This thesis presents theoretical and experimental studies of the temperature characteristics of strained-layer multiple quantum well lasers operating at wavelengths near $1.3\mu\text{m}$. Chapter 2 details the experimental setups used to characterize the lasers. The measurements that were carried out include: continuous wave (CW) light vs current (L-I), pulsed L-I, the laser output spectra and far field intensity distributions. The facilities were capable of testing devices over the temperature range of 100–460K.

Chapter 3 - 5 presents the experimental characterization of $1.3\mu\text{m}$ wavelength, 0.7% compressive SL-MQW ridge waveguide lasers with varying well number, and the theoretical analysis of the temperature dependence of the I_{th} , the external quantum efficiency, η_d , and the internal loss, α_i .

Based on the assumptions that the differential gain coefficient decreases linearly with temperature, and that the optical gain is a dominant mechanism in determining the temperature sensitivity, a formula is derived in Chap. 3 to describe the I_{th} vs. T relationship. A parameter defined as T_{max} , which is related to the inherent physical properties of the laser, appears naturally in the formula. When the temperature approaches T_{max} , I_{th} approaches infinity, so T_{max} may be regarded as the maximum operating temperature of the laser diode. The derived formula is applied to measured I_{th} vs. T results to verify the derived formula and underlining assumptions. In Chapter 4, the same assumptions are used to derive a formula that includes T_{max} and relates η_d to temperature. When T approaches the T_{max} , the external quantum efficiency approaches zero, so the laser ceases lasing. Thus, again, it is concluded that

T_{\max} is the upper limit of temperature for laser operation. T_{\max} values were then extracted by fitting the derived formula to the measured η_d vs. T data of same group of lasers as used for the I_{th} vs. T studies. The T_{\max} values obtained in this way were found to be consistent with those obtained from I_{th} vs. T data, which gives credibility to the concept of the maximum operating temperature and underlying assumptions.

In Chapter 5, the traditional method of determining the internal quantum efficiency, η_i , and the internal optical loss, α_i , by using a set of lasers varying in length, but otherwise assumed to be the same, is scrutinized. The internal quantum efficiency determined in this way is not the expected internal quantum efficiency. It is a function of temperature, even though the true internal quantum efficiency is independent of temperature. When the temperature is much less than the maximum operating temperature, the internal quantum efficiency is equal to the true internal quantum efficiency. The internal optical loss obtained by this method is a linear function of temperature if the optical loss due to factors such as phonon scattering can be ignored.

In Chapter 6, the far field intensity distribution of $1.3\mu\text{m}$ 1.2% tensile SL-MQW ridge waveguide lasers with varying ridge width ($2\mu\text{m}$ to $32\mu\text{m}$) is measured. The measurements are then carried out at various temperatures under pulsed operation and the lateral far-field distributions calculated by using the effective refractive index method. At a fixed output power level (3mW), it was observed that the far-field pattern of a $2\mu\text{m}$ wide ridge laser remained almost constant at a testing temperature range of 110K to 400K, which indicates that injected carriers (the carrier density in quantum well at 400K is much higher than that at 110K) have very little effect on the refractive index. The $4\mu\text{m}$, $8\mu\text{m}$ and $16\mu\text{m}$ wide lasers show multiple lateral mode features in the far-field patterns at 110K. The fundamental mode gradually emerges with rising temperature; however, the $32\mu\text{m}$ laser has multiple mode features in its far-

field patterns at all testing temperatures. It is shown that the measured far-field patterns can be constructed by the proportional superposition of the calculated far-field intensity distributions.

Chapter 7 deals with heating and the resulting temperature rise, caused by the applied driving current during CW operation. By using the experimental I_{th} vs. T and η_d vs. T relations measured under short-pulse operation as the intrinsic temperature characteristics of the lasers at the temperature of the laser mount, and the L-I curves under CW operation, the internal temperature rise under CW operation was determined. From these data, the thermal impedance of the lasers was calculated. It is concluded that the wider the ridge, the lower the thermal impedance; however, because of higher temperature dependence of the threshold current, it has a lower maximum CW operating temperature.

Chapter 2

EXPERIMENTAL PROCEDURE AND LASER STRUCTURE

2.1 Introduction

In order to study the temperature characteristics of 1.3 μm strained-layer multiple quantum well lasers, a series of experiments was undertaken and various experimental set-ups for those experiments were established. Three systems capable of operation over large temperature range were assembled. One performs light-current (L-I) measurement in pulsed and continuous-wave (CW) mode, the second is for optical spectra measurement, and the third is for measurement of the far-field mode patterns. The structures of the lasers studied in thesis are also presented.

To make the measurement convenient and avoid possible human error in data collection, a fully computer-controlled system was constructed using a GPIB/IEEE 488.2 controller card in the computer and GPIB/IEEE 488.2 interfaces in various pieces of equipment used in the system. A high-resolution temperature controller, a precision laser driving current source, which could operate in CW or pulse mode, two Gated Integrator and Boxcar Averagers (GIBA), a stepper motor driven x-y-z stage, a high-resolution monochromator, and a Computer Interface, which has a precise A/D conversion (with a resolution 2.4mV) were used in the experimental set-ups. An

essential part of the set-up is a specially designed cooling system. It is a modified version of a commercial 1-litre liquid nitrogen dewar, in which a specially designed heating unit is mounted. The temperature of the cooling system is monitored by two thermocouples, one of which is attached close to the laser assembly, while the other is attached to the cold head of the dewar to monitor its thermal stability.

2.2 Experimental Set-ups in Pulse Mode

The semiconductor lasers can be tested in pulsed or CW mode. Since the heating during CW operation distorts I_{th} vs. T and η_d vs. T experimental data, the experiments to achieve I_{th} vs. T , η_d vs. T data, far field pattern versus temperature, and optical spectra were carried out in pulsed mode to minimize the heating effects. CW measurements, however, were used to study the heating during CW operation.

2.2.1 Set-up for L-I Measurement

The set-up to undertake the pulsed mode L-I measurements is schematically illustrated in Fig.2.2.1. It consists of a temperature controller, a precision laser driving source, a GIBA, and a cooling system.

When the laser driver sends a current pulse to the laser, it simultaneously sends a TTL trigger signal to the GIBA. Then, the GIBA issues an integration gate signal, the width and delay time of which could be adjusted to selectively overlap the gate signal and the signal from the detector, which measures the amplitude of the signal. The detector is terminated by a 50Ω resistor to increase its response speed. Figure 2.2.2 illustrates the relationship of the gate signal and the detector signal.

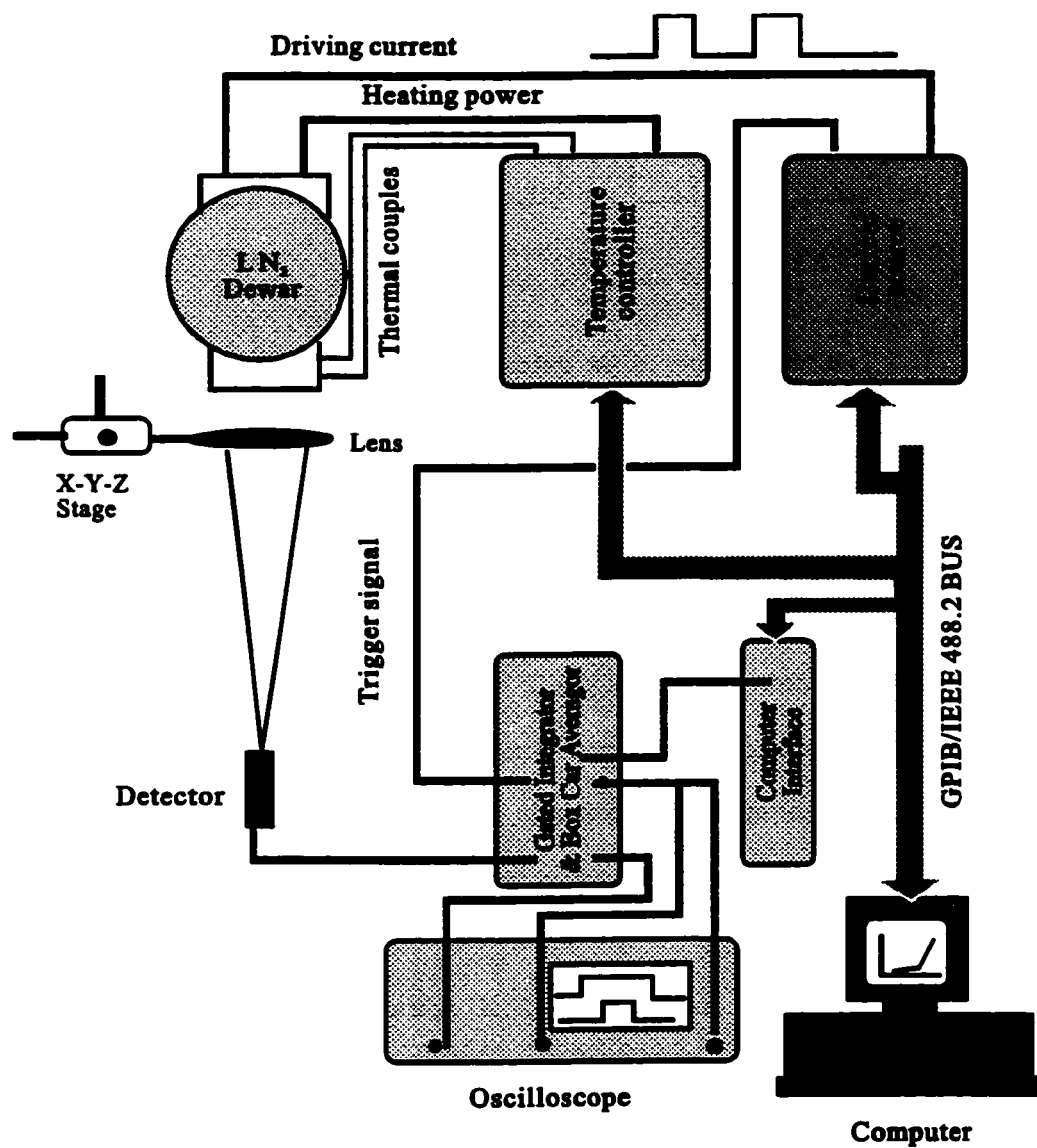


Fig.2.2.1 Schematic experimental set up for pulse measurements.

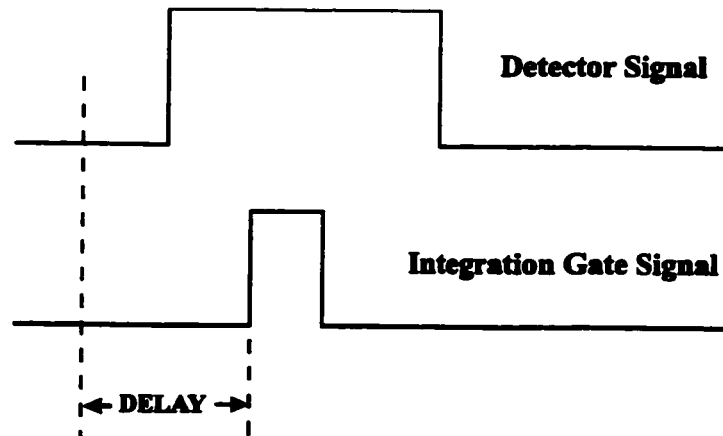


Fig. 2.2.2 The relationship of the gate signal and the signal from the detector

The temperature controller is a Lakeshore model 330. The temperature sensors are chromega/alomega thermocouples. The controlling accuracy is ± 0.01 °C below 200K and ± 0.05 K above 200K. The controller has a GPIB/IEEE 488.2 computer interface which is controlled via a IEEE bus by the computer. To achieve a stable temperature, the open ends of the thermocouple were soldered to two pieces of copper, and immersed in oil, which was in thermal balance with an ice-water mixture. This method was preferred to using the thermal electronic compensation unit in the temperature controller.

The laser driving source is an ILXLightwave LDP-3811 precision pulsed current source, which could be operated in CW or pulse mode. The maximum output current is 500mA with an accuracy $\pm 0.5\%$ full scale. The calibration curve for pulsed operation is presented in Fig. 2.2.3. It was taken by directly connecting the laser current source to the GIBA. The nominal driving currents and the measured currents are linearly related to each other. The current source also has a GPIB/IEEE 488.2 computer interface. To ensure proper impedance matching, an adjustable resistor was placed in series with the laser diode, so that the input current and subsequent optical

output were clean, square pulses. The magnitude of the series resistance plus the dynamic resistance of the diode was set approximately to 50Ω in order to match the impedance of the transmission line. An additional consideration in obtaining a clean signal was to keep the transmission line as short as possible.

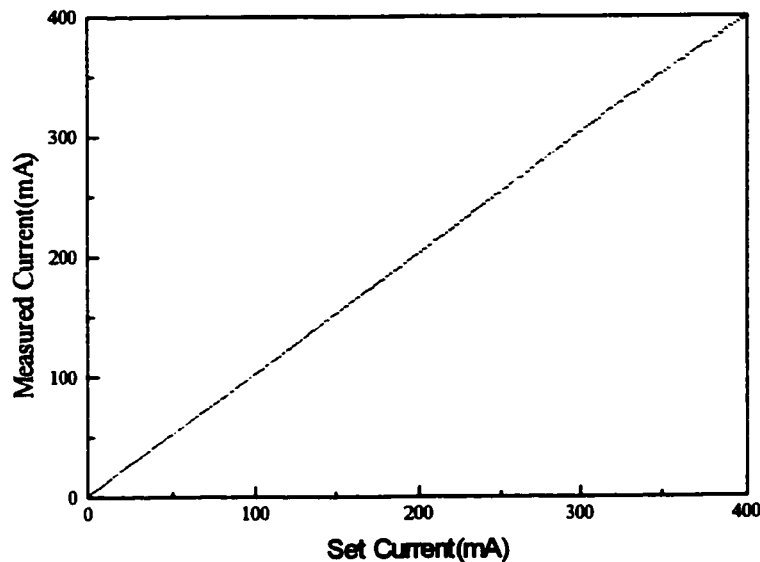


Fig. 2.2.3 The calibration curves for the laser current source in pulsed mode. The nominal driving current is consistent with the measured current.

The emitted light from the laser was collected by a large numerical aperture objective lens, and was focused on to an EG&G C30642 InGaAs large area (3mm^2) detector. The detector was biased by 1.5V, connected by a 50Ω coaxial cable to the GIBA, and terminated by a 50Ω resistor. The detector responds linearly up to 8mW input power. Since the light from quantum well lasers is polarized in a TE or TM mode, to detect high power a linear polarizer is used to attenuate incoming light.

The light intensity P is calculated in terms of the measured voltage V by

$$P(\text{mW}) = \frac{V(\text{mV})}{50(\Omega)R(\text{mA} / \text{mW})} \quad (2.2.1)$$

where R is the responsivity, which is calibrated according to the wavelength of the laser. The L-I measurement was taken in current steps of 0.2mA to a preset maximum power or a preset maximum driving current and displayed in real time on the monitor of the computer.

The lasers were bonded p-side up on a piece of silicon carbide, which was bonded on to a piece of gold-plated copper, as shown in Fig. 2.2.4. Also bonded to the copper block was a small ceramic chip (standoff) with a gold-coated top. The copper block was then epoxied to thermally conductive ceramic boards. The ceramic boards have large gold pads used for external electrical contacts. Electrical contact between the device and the pads was established by gold bond wires. This mounting design facilitates device handling, electrical contact, and testing.

The laser assembly sat on a heater (Fig. 2.2.5), which was attached to the cold header of the liquid-nitrogen-cooled dewar. The dewar was modified from a commercial one to accommodate the heater assembly. The top of the heater is a copper block, which holds a laser assembly, and beneath which is a teflon block. Embedded inside the upper half of the teflon block is an electrical wire coil as a heat source. The lower half of the teflon block acts as an insulation layer between the heat source and the cold header of the dewar. This design keeps the cooling system stable at a set temperature, even when the laser assembly was heated to high temperature (~460K).

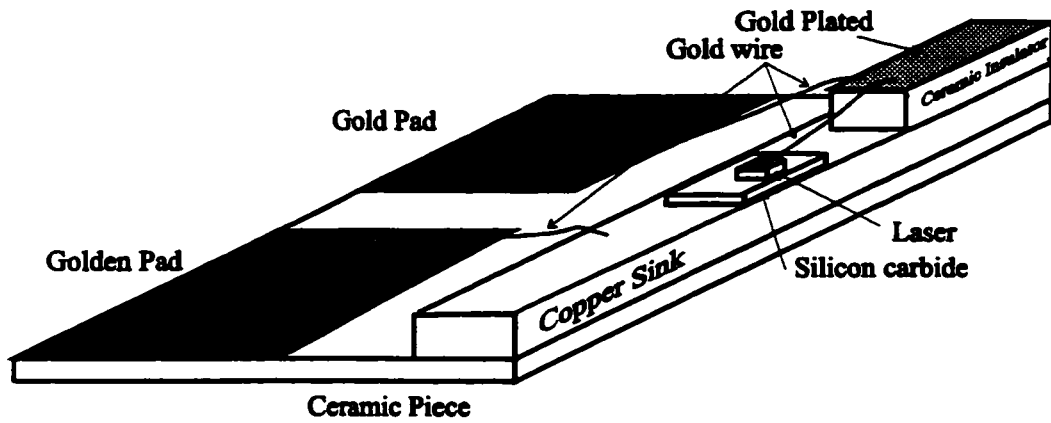


Fig.2.2.4 The laser assembly. The laser is bonded p-side up on a carbide, which is bonded to a copper.

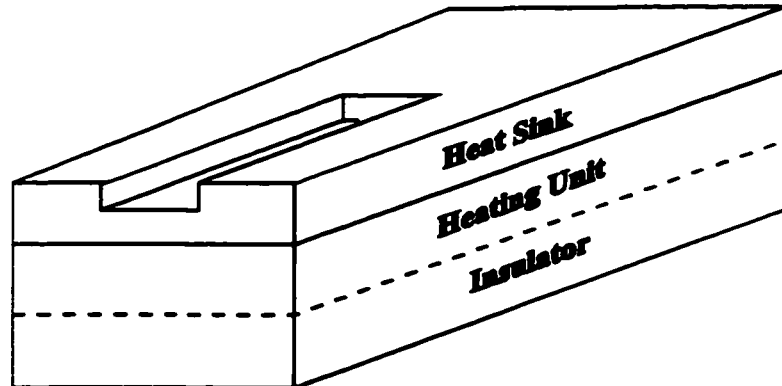


Fig.2.2.5 The designed heating unit. A heating wire coil is embedded in the top of a piece of teflon as a heating source; the partial thermal insulation provided by the lower part of the teflon block to keep the thermal stability of the system.

2.2.2 Set-up for Far-field Measurement

Far-field measurements were taken in the pulsed mode, in order to avoid heating in active region. A stepper motor and a stepper motor controller were added to the system, as schematically illustrated in Fig.2.2.6, to be used to scan the detector position. A small area InGaAs detector (0.09mm^2) biased at 1.5V was mounted on a x-y-z stage, which could be precisely moved horizontally by the stepper motor. The signal from the detector was amplified 100 times by a high-speed amplifier before it was sent to the GIBA. The stepper motor was driven by the stepper motor controller, which was controlled by the computer via the computer interface. For two-dimensional far-field measurement, the detector was moved manually in the vertical direction.

2.2.3 Set-up for spectrum measurement

Figure 2.3.4 is a schematic diagram of the set-up for spectral measurements, for which a monochromator was added to the pulse measurement set-up. The laser light was focused onto the input slit of the monochromator by a lens combination. The grating mirror in the monochromator was precisely rotated step-by-step by a stepper motor, and each step has an increment of 0.25\AA . The stepper motor was driven by a stepper controller, which was controlled by the computer via the computer interface as in the far-field set-up. The signal from detector was amplified 100 times by a high-speed amplifier and then sent to the GIBA.

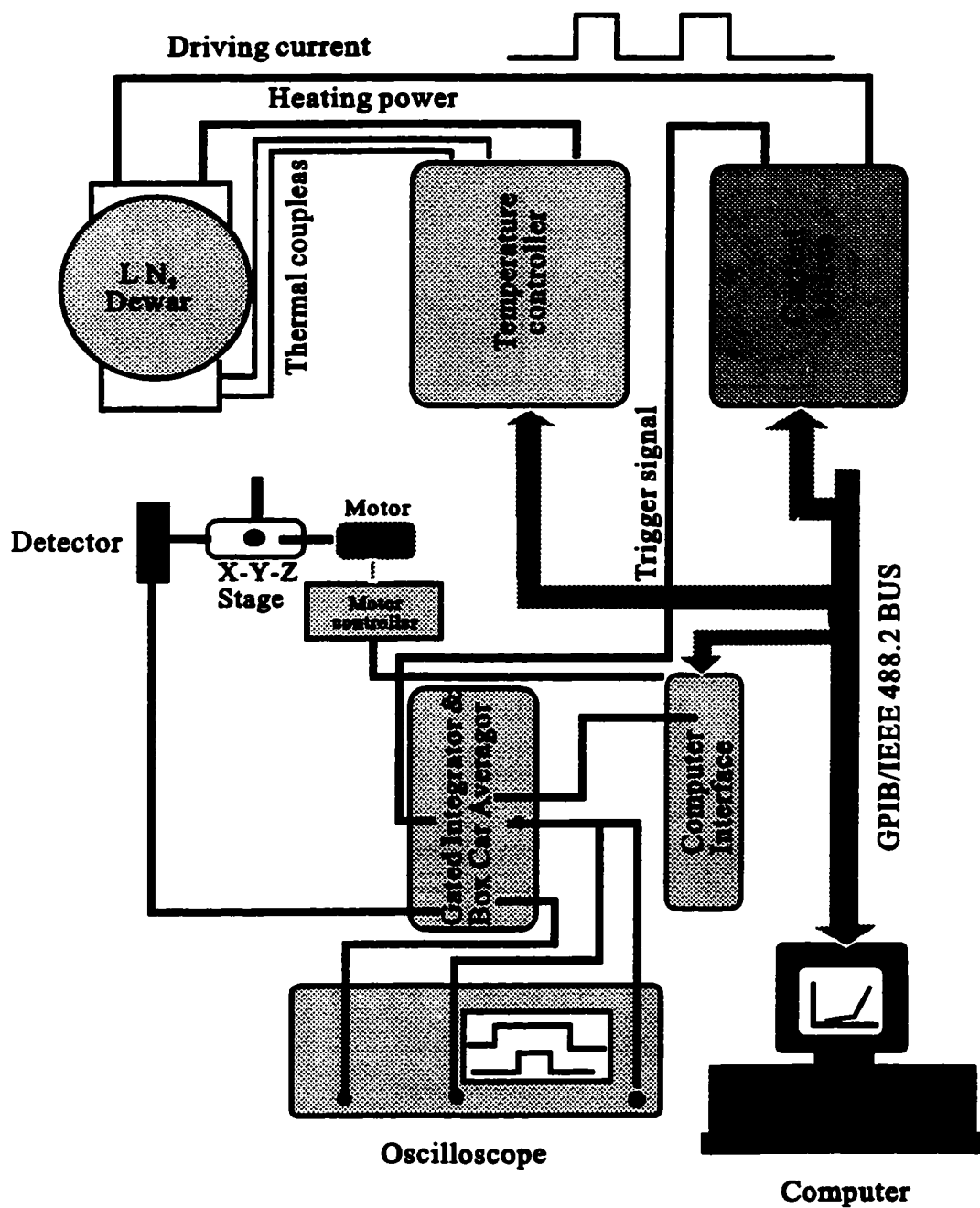


Fig.2.2.6 The set-up for far field measurement. A stepper motor was used to precisely control a x-y-z stage for horizontal movement of a small detector.

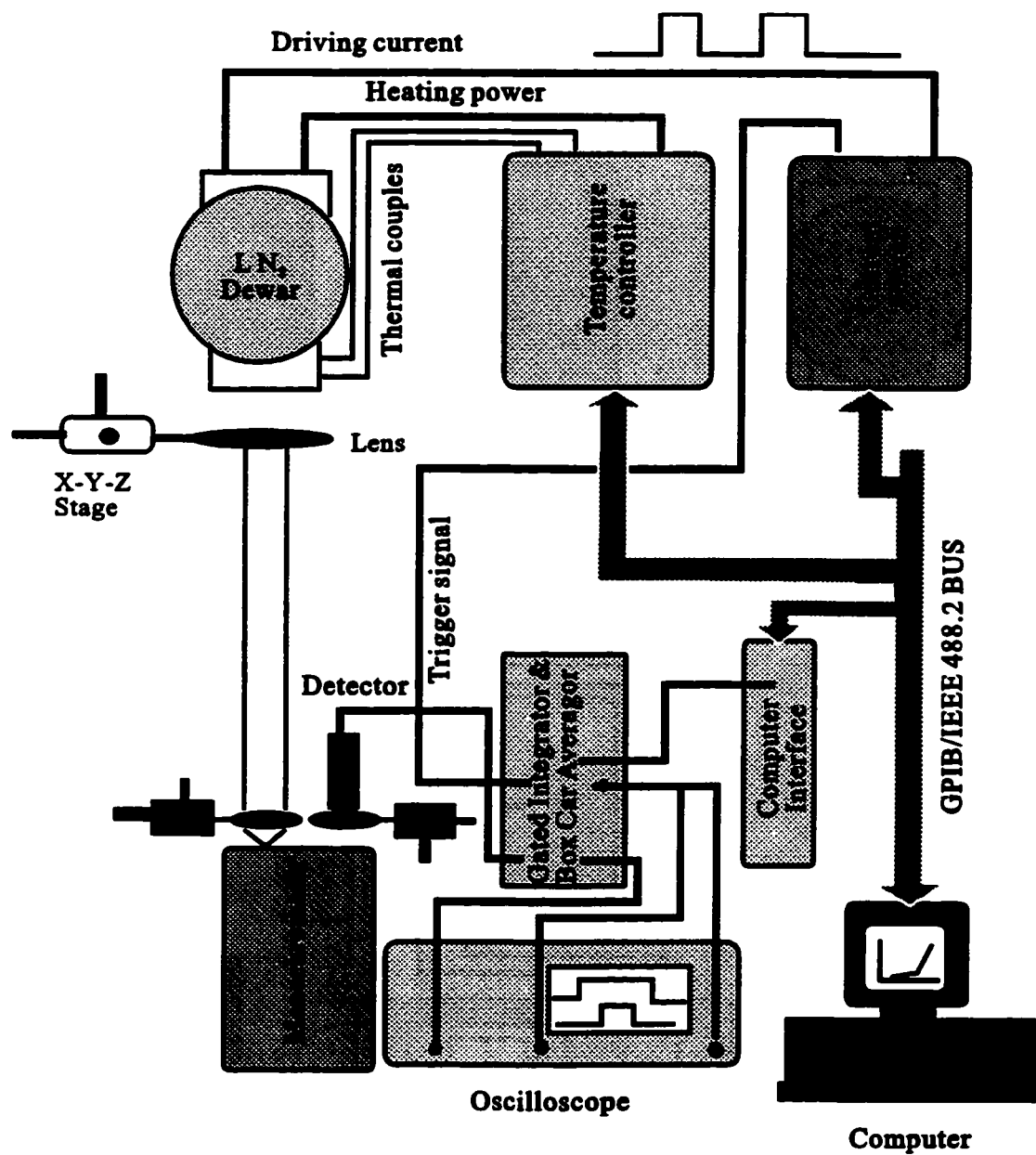


Fig.2.2.7 The set-up used for the optical spectrum measurements. The mechanical resolution is 0.25\AA , which is determined by the stepper motor and the gear assembly in the monochromator.

2.3 Set-up for CW Measurement

Figure 2.3.1 illustrates typical CW L-I curves at various temperatures of a 0.7% compressive SL-MQW laser containing 10 wells, taken using the set-up illustrated in Fig. 2.3.2. The laser driving current source was set in CW mode, and the GIBA was set in the self-trigger mode. The detector was terminated by a 50Ω resistor, which converted the incoming current signal from the detector to a voltage signal to be measured by the computer interface. The Gated Integrator and Boxcar Averager averaged the incoming signal thirty times, and then transferred the signal to the Computer Interface. The computer averaged the input signal a further twenty times to reduce noise level.

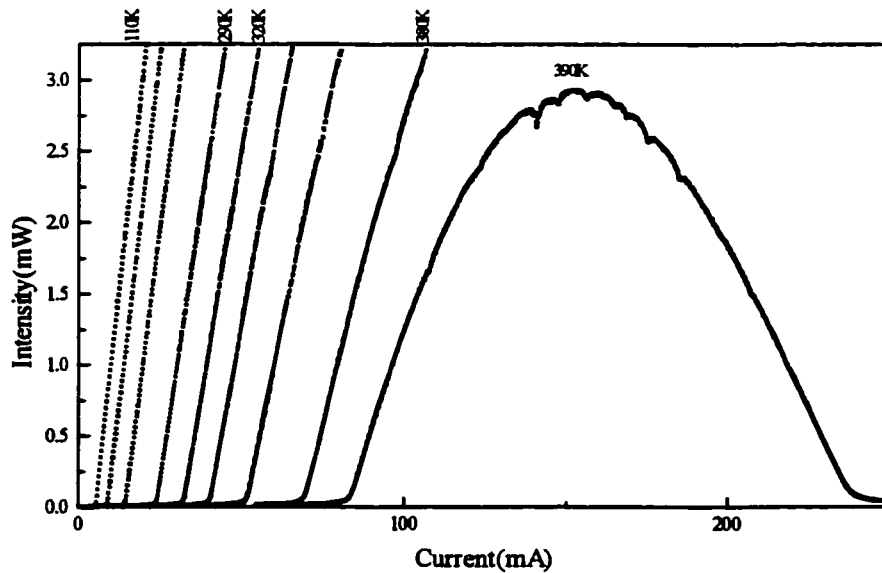


Fig.2.3.1 Typical L-I curves for a 10-well, 0.7% compressive-strain quantum well laser obtained using the illustrated CW set-up

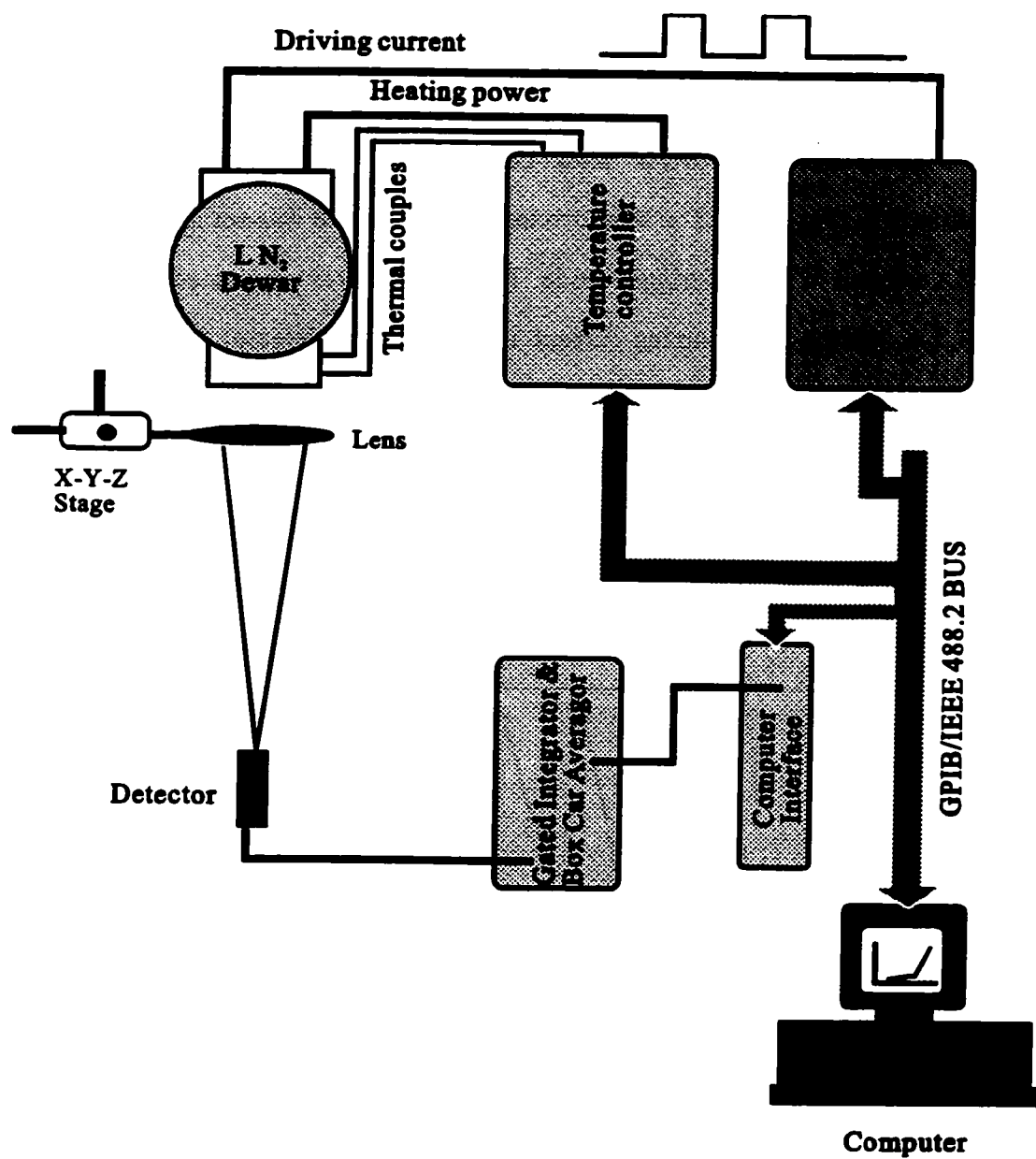


Fig.2.3.2 The set-up for the CW measurement. The laser driver is in the CW mode and the Gated Integrator and Boxcar Averager is in the self-trigger mode

2.4. Computer Program Used for System Control

To coordinate the operation of equipment and the data collection, a program written in the language C was used for all measurements. The measured results were displayed in real time on the computer screen, and stored on a disk for subsequent data processing. The program also includes the calculation of the threshold current and the external quantum efficiency for each L-I curve, by using a least squares method, on a group of selected current-intensity points above the threshold current, and the results are stored in a separate data file.

The program implements the following functions:

a) the temperature feedback control to raise the temperature of the tested laser to a set-point temperature with a preset precision. This involves reading the temperature from the temperature controller and then comparing it with the set-temperature.

b) the driving current feedback control to increase the current step-by-step to a limit, which may be set by a preset maximum power or maximum driving current.

c) pulse measurements

d) CW measurements

e) far-field measurements

f) spectrum measurements

g) detector conversion efficiency at specific wavelength

The program could be used to control the system for the L-I measurements in pulse- or CW-mode, far-field measurements, and spectral measurements over a wide range of temperatures and driving currents.

2.5 Laser Structures

The lasers investigated in this thesis are 0.7% compressive- and 1.2% tensile-strain InGaAsP/InP MQW lasers, the structures of which are shown schematically in Fig.2.5.1 and 2.5.2, respectively.

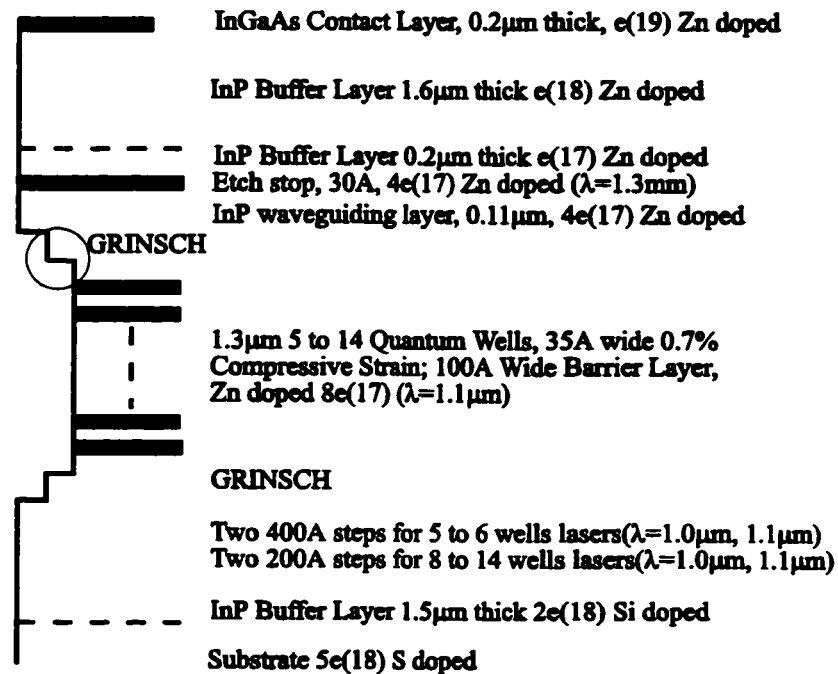


Fig.2.5.1 The laser structure for 5 to 14 wells 0.7% compressive SL-MQW InGaAsP/InP lasers.

The compressive SL-MQW lasers contain 5 to 14 35Å-wide quantum wells. The barrier layers of lasers are 100Å-wide, unstrained, and with a band gap of 1.127eV. The active region is sandwiched by two-step waveguiding layers of band gaps 1.24eV and 1.127eV. The tensile SL-MQW lasers contain 3 80Å-wide quantum wells. The barrier layers are 200Å-wide, unstrained, and with a band gap of 1.1643eV. The active region of the lasers is sandwiched by two 1300Å-wide waveguiding layers

of a band gap 1.1643eV. The two structures were grown by low pressure metalorganic vapor phase epitaxy (LP-MOCVD) on (100) oriented S-doped n-type InP substrates. Both sets of lasers have an operating wavelength of 1.3 μ m at room temperature.

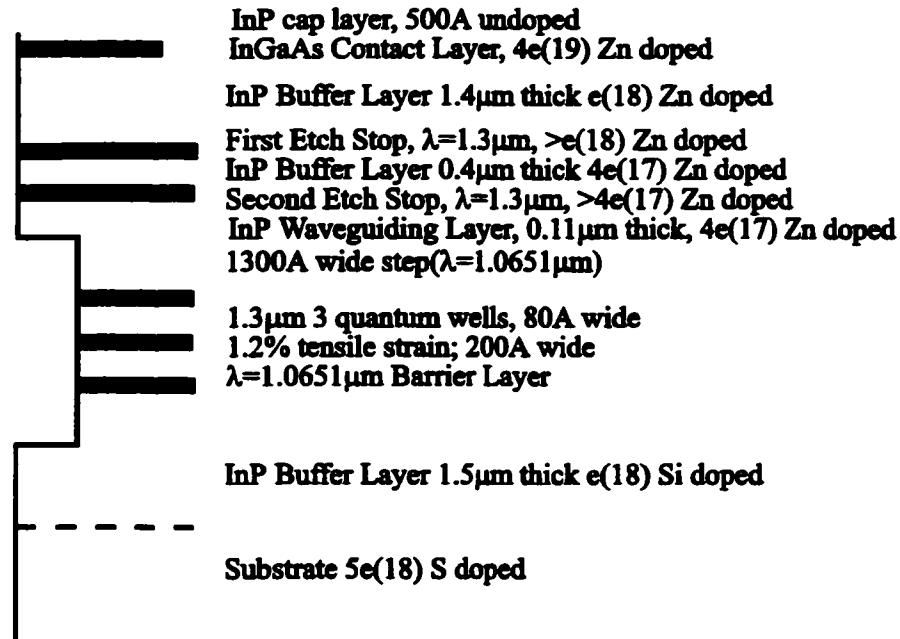


Fig.2.5.2 The laser structure for 1.2% tensile SL-MQW lasers containing 3 quantum wells. The wells are 80Å wide and the barriers 100Å thick.

Compressive strain splits the heavy and light hole bands. The band gap between the heavy hole band and the conduction band is larger than that of the light hole band and the conduction band [Morkoc, 1993], as shown in Fig. 2.5.3, and the quantum confinement effect further separates them. The splitting of heavy hole and light hole bands can improve the performance of lasers [Corzine, 1993] [Coleman, 1993], so narrower quantum wells are used in the compressive SL-MQW lasers. Tensile strain also splits the heavy and light hole band as the compressive strain does,

as shown in Fig.2.5.3. However, the band gap between the light hole band and the conduction band is larger than that of the heavy hole band and the conduction band, and the quantum confinement effect compensates for the tensile strain effect. To ensure a larger separation of the heavy hole and light hole bands, larger tensile strain and wider quantum wells are usually required in the design of tensile strained layer multiple quantum well lasers [Thijs, 1994]. To meet these criteria, the compressive SL-MQW lasers investigated in thesis have 0.7% strain and 35Å wide quantum wells, and the tensile SL-MQW lasers have 1.2% strain and 80Å wide quantum wells. The compressive SL-MQW lasers have TE polarization and the tensile SL-MQW lasers have TM polarization at all tested temperatures.

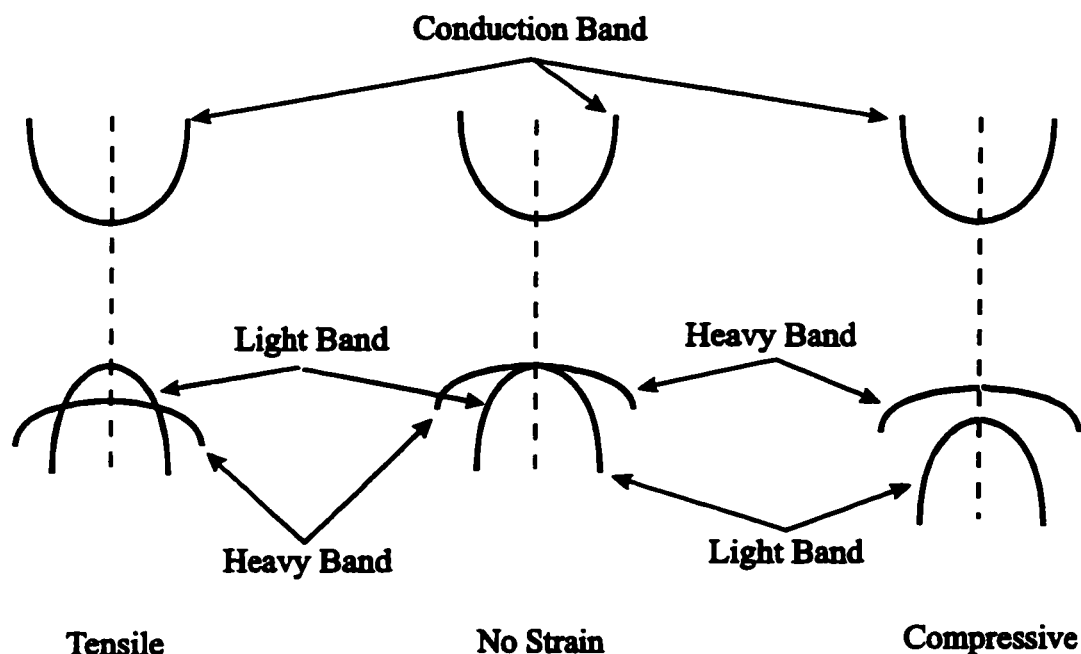


Fig.2.5.3 Schematic illustration of band structure with (a) tensile strain, (b) no strain, and (c) compressive strain

All lasers are uncoated Fabry-Perot ridge waveguide lasers, and a schematic cross section is shown in Fig.2.5.4. The ridge width is $2\mu\text{m}$ for the compressive SL-MQW lasers, and $2\mu\text{m}$ to $32\mu\text{m}$ for the tensile SL-MQW lasers. The etch depth is $2\mu\text{m}$.

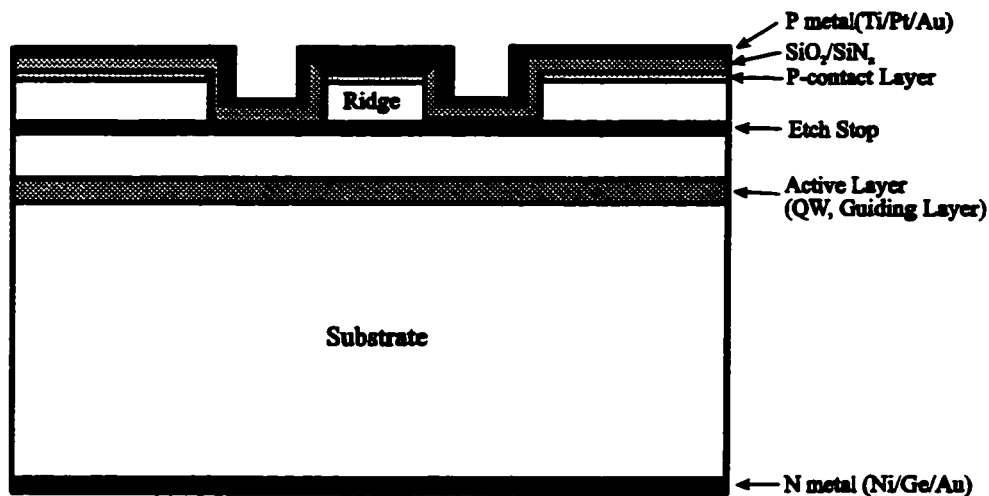


Fig.2.5.4 The cross-section of the ridge waveguide lasers used in thesis

Because of the narrow ridge width, the compressive SL-MQW lasers have single mode features in the far-field, both laterally and vertically. The experimentally measured far-field patterns at 110K and 350K for a 0.7% compressive SL-MQW laser containing 10 wells is shown in Fig 2.5.5. It shows that the injected carrier density has little effect on the far-field pattern. In appendix A, the calculation of the bandgap between the conduction band and the heavy hole band or the light hole band in terms of different alloy compositions and strain is presented. A computer program that

allows the calculation of the alloy composition of quantum well for the required emission wavelength, the width, and the strain of the well, is attached.

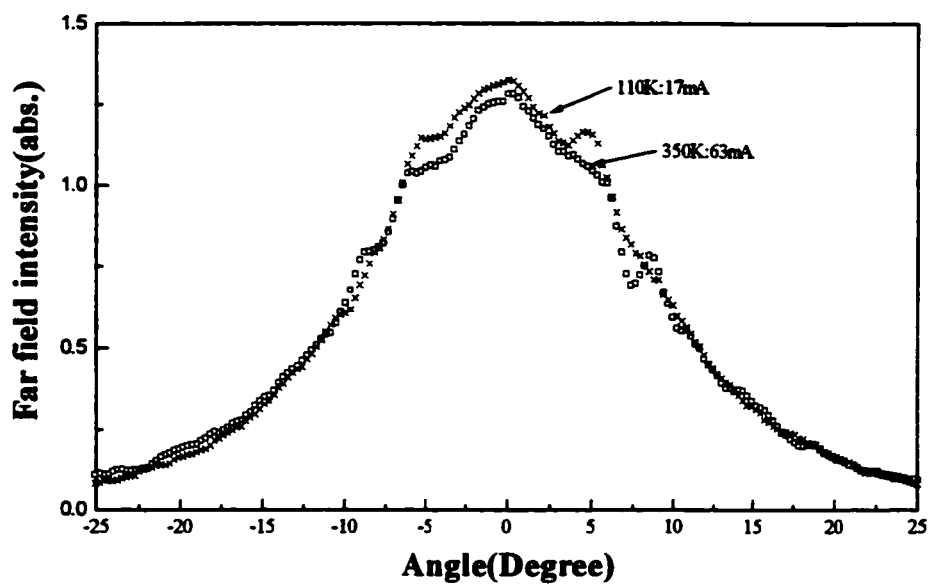


Fig.2.5.5 The measured far field at 110K and 350K. Temperature has little effect on the far field pattern.

Chapter 3

TEMPERATURE DEPENDENCE OF THE THRESHOLD CURRENTS

3.1 Introduction

Threshold current, which is an important characteristic parameter of a semiconductor laser, is analyzed in this chapter. At first, the historic studies of the threshold current as a function of temperature are reviewed. Then, after assuming that the differential gain coefficient decreases linearly with temperature T , a new formula is derived to describe the I_{th} vs. T relationship. The developed formula is then applied to the experimental I_{th} vs. T data extracted from short pulse measurement (to minimise heating in semiconductor laser) of $1.3\mu\text{m}$ 0.7% compressive SL-MQW ridge waveguide lasers with varying well number.

3.2 Temperature Dependence of Threshold Current

It is a convention to use an empirical relation, which was proposed by Pankove [Pankove, 1968], to describe the threshold current as a function of the temperature.

$$I_{th} = I_0 e^{T/T_0} \quad (3.2.1)$$

T_0 is usually used to measure the temperature sensitivity of the threshold current; the smaller the T_0 , the more sensitive the threshold current to the temperature. However, T_0 is a largely meaningless quantity in terms of either laser design or as an indicator of high-temperature performance [Temkin, 1993]. Recently, Evans *et al.* proposed an empirical relation that described threshold current density J_{th} vs. T data extracted from CW experiments over a wide range of temperature:

$$J_{th} = 1 / \left[\frac{n}{C} (T_{max} - T) \right]^{1/n} \quad (3.2.2)$$

where n and C are constants, and T_{max} is the maximum operating temperature for laser action. The maximum operation temperature T_{max} has been measured, and discussed occasionally for CW operation [Temkin, 1993] [Oohashi, 1995]. The unit of C changes with the number n . Therefore, n must be a dimensionless constant to keep C having a constant physical unit.

The threshold current has also been related to the losses of the laser in different ways. A typical equation [Larsson, 1989] is:

$$J_{th} = \frac{J_{tr}}{\eta_i} + \frac{\alpha_i}{\eta_i \Gamma \beta} + \frac{1}{\eta_i \Gamma \beta L} \ln(1/R) \quad (3.2.6)$$

where J_{tr} is the transparent current density, α_i is the internal loss, η_i is the internal quantum efficiency, Γ is the optical confinement, L the length of the laser, and R is the

reflectivity of the end facet of the laser. The assumption used in deriving (3.2.3) is that the optical gain g is a linear function of the current density J :

$$g = \beta \cdot (J - J_{tr}) \quad (3.2.7)$$

Where β is the optical gain coefficient. Another relationship is [Coleman, 1992]:

$$J_{th} = \frac{J_{tr}}{\eta_i} \exp\left(\frac{\alpha_i + \ln(1/R)/L}{\Gamma\beta J_{tr}}\right) \quad (3.2.8)$$

and

$$g = \beta J_{tr} \ln(J / J_{tr}) \quad (3.2.9)$$

was assumed. Obviously, the temperature sensitivity of β , J_{tr} , η_i , and α_i contribute to the temperature sensitivity of the threshold current.

It is widely known that the differential gain decreases with an increase in temperature [Dutta, 1982, 1983] [Zhu, 1989] [Zou, 1993]. Recently, the fact that β decreases with increasing T was recognized as a dominant mechanism in determining the temperature sensitivity of the I_{th} [Zou, 1993][Temkin, 1993][Bernussi, 1995][Seki, 1995], after an earlier failure of the calculated temperature dependence of the optical gain to explain the greater temperature sensitivity of InGaAsP [Dutta, 1982][Evans, 1994]. To compensate for the optical loss, which increases with the increasing temperature, the optical gain required to achieve lasing increases with the increasing temperature; however, to achieve a higher optical gain, a higher carrier density is required, as shown schematically in Fig. 3.2.1.

In Fig. 3.2.1, a carrier-injection-related loss is assumed to increase linearly with the carrier density [Ackerman, 1995]. The intersection point of the loss line and the optical gain line determines the threshold gain and the threshold carrier density. Since the slope of the gain line decreases with temperature, the intersection point moves to the higher carrier density until the lines cease to intersect. The temperature at which the lines first cease to intersect may be regarded as the maximum operation temperature, T_{\max} , of the laser. Therefore, the decrease of the differential gain with temperature plays a vital role in determining the temperature sensitivity of the threshold current and will be explored further in next section.

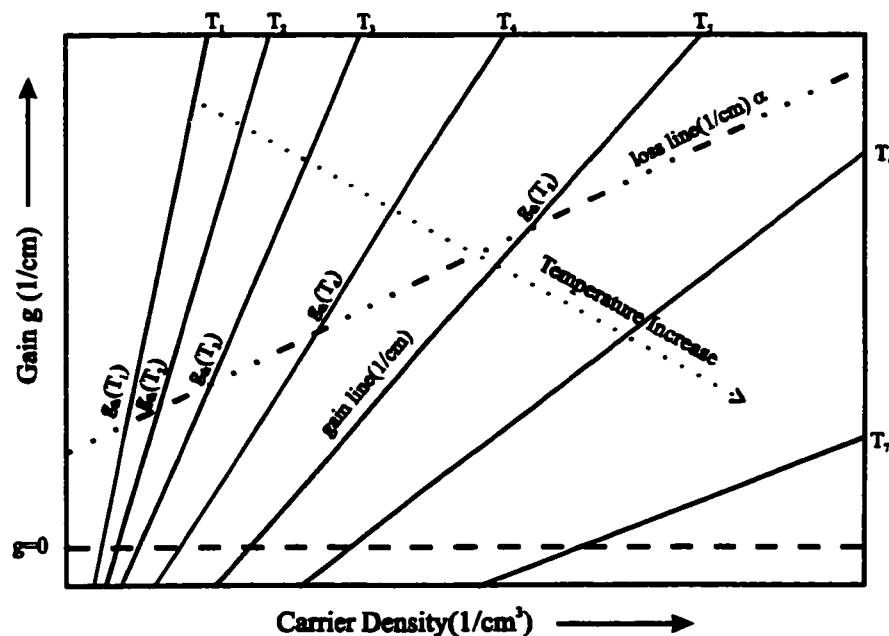


Fig. 3.2.1: Schematic diagram of the change in the optical gain vs. carrier density as a function of temperature. Since the slope of the gain vs. carrier concentration decreases with increasing temperature, as the temperature increases, more injected carriers are required in order to reach the threshold gain condition to compensate the increasing optical loss with temperature. As a result, as the temperature increases, more current is required to produce lasing, so the threshold current increases with temperature.

Another mechanism that is cited as being responsible for the temperature sensitivity of the threshold current is the increase of the optical loss with temperature. In early work [Asada, 1981, 1983][Adams, 1980], the increase of the internal loss with temperature was regarded as a dominant mechanism in determining the temperature sensitivity of the threshold current. Recently, it was proposed that the internal loss caused by the carriers spilling into the confinement region in multiple quantum well laser dominates the high temperature behaviour of the threshold current [Mikhaelashvili, 1994] [Seki, 1995]. However, the internal loss depends only moderately on temperature [Zou, 1993] [Evans, 1994], so it is unlikely that the increase of internal loss with temperature causes the rapid increase of the threshold current with temperature. The internal loss will be discussed and incorporated into a new formula to describe the temperature dependence of the threshold current in next section.

Another mechanism that has been invoked to explain the temperature sensitivity of the threshold current of InGaAsP semiconductor lasers is nonradiative Auger recombination [Dutta, 1982]. Recently, however the Auger recombination processes have been excluded from the consideration of causes of the temperature sensitivity [Zou, 1993] [Bernussi, 1995] [Seki, 1995]. Though some work still suggested that the Auger recombination plays a dominant role in determining the temperature sensitivity of the threshold current [O'Reilly, 1993][Li, 1995], it will not be included in the analysis of this thesis.

3.3 Theoretical Analysis of the Dependence of Threshold Current on Temperature

Theoretical and experimental studies suggest that the temperature dependence of the optical gain is a dominant mechanism in determining the temperature sensitivity of the semiconductor quantum well laser [Zou, 1993] [Temkin, 1993]. Assuming that the differential gain coefficient decreases linearly with temperature, a formula is developed in this section to describe the threshold current as a function of temperature.

The optical gain g may be written as [Bernussi, 1995] [Ackerman, 1995]

$$g = \beta(n - n_{tr}) \quad (3.3.1)$$

where n is the carrier density in the quantum well, β is the differential gain coefficient, which defines a rate at which the gain increases with injected carrier density ($\partial g / \partial n$), and n_{tr} is the transparent carrier density. Both β and n_{tr} are temperature dependent. In particular, the decrease of β with temperature is assumed a dominant mechanism in determining the temperature sensitivity of threshold current at high temperature.

The total loss α_{total} of a semiconductor laser usually is written as [Koren, 1987] [Ackerman, 1995]:

$$\alpha_{total} = \gamma n + \alpha_1(T) + \alpha_0 + \alpha_m \quad (3.3.2)$$

The term γn represents a loss that is linearly dependent on the carrier density. The proportionality coefficient γ is assumed temperature independent [Ackerman, 1995].

The loss is due to the free carrier scattering and the intervalence band absorption. The weakly temperature dependent loss $\alpha_1(T)$ is due to phonon scattering and any other possible temperature dependent loss. The residual loss α_0 , arising from scattering at crystal imperfections and evanescent waveguiding loss, is assumed to be temperature independent. Finally, the mirror loss $\alpha_m = \ln(1/R)/L$, where L is the length of laser and R is the reflectivity of laser facet. Since the reflectivity of the laser facet is temperature independent, the mirror loss is also temperature independent.

At threshold, the gain g_{th} must be equal to the total loss $\alpha_{total,th}$.

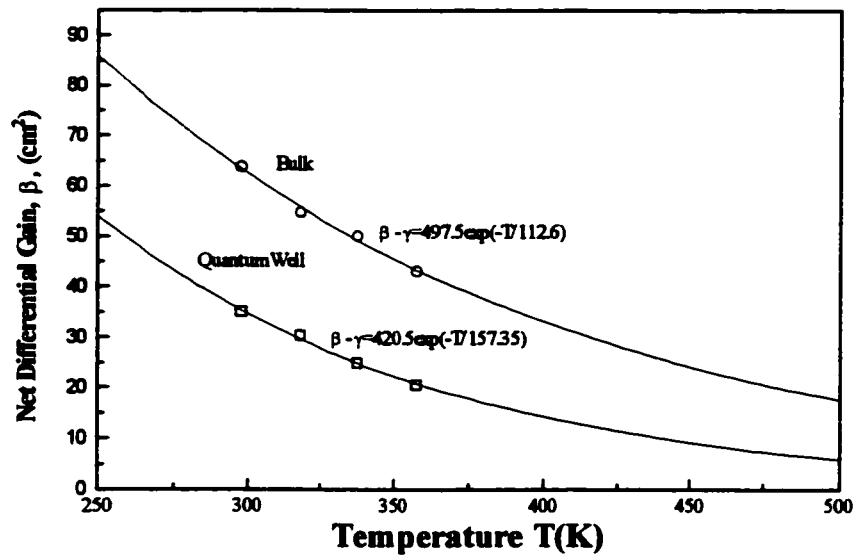
$$g_{th} = \beta(n_{th} - n_{tr}) = \alpha_{total,th} = \gamma n_{th} + \alpha_1(T) + \alpha_0 + \alpha_m \quad (3.3.3)$$

After some manipulation, (3.3.3) can be written as:

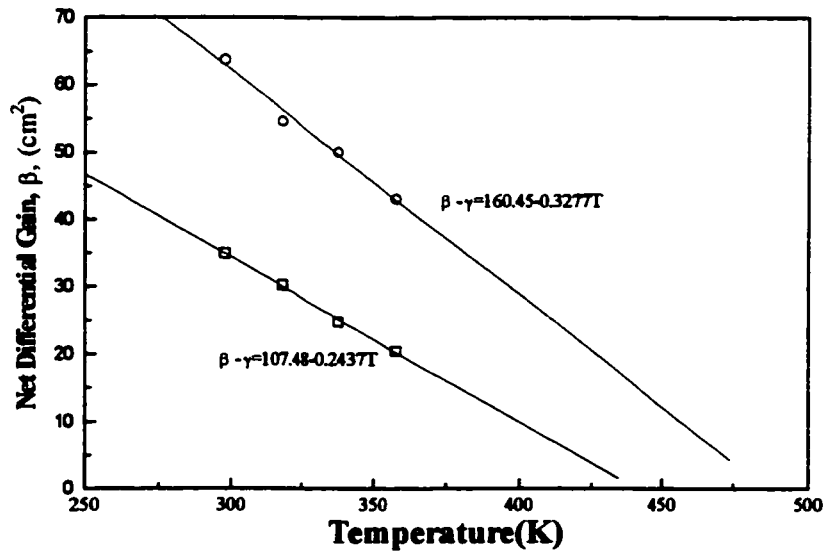
$$n_{th} = \frac{\alpha_1(T) + \alpha_0 + \alpha_m + \beta n_{tr}}{\beta - \gamma} \quad (3.3.4)$$

This equation means that for a semiconductor laser to lase, β must be larger than γ , and is similar to an equation used by Ackerman [Ackerman, 1995].

Experimentally, it is widely known that β decreases with increasing temperature. Figure 3.3.1 shows the extracted differential gain, β , versus temperature from recently published experimental results [Ackerman, 1995] of the net optical gain or loss vs. temperature. To explain the approximately exponential relation between I_{th} and T , an exponential relationship was used by Ackerman to fit β vs. T data, which is shown in Fig.3.3.1(a). In this thesis, a linear function between β and T is proposed to be used to fit β vs. T data, as shown in Fig.3.3.1(b). Based on this experimental data, assumptions are made in this thesis that β decreases linearly with temperature.



(a)



(b)

Fig.3.3.1 Extracted differential gain coefficient versus temperature [Ackerman, 1995]. The solid line in (b) is an exponential fitting curve used by Ackerman et al. and the linear fitting curve in (b) is proposed in this thesis

$$\beta(T) = \beta_0 - mT \quad (3.3.5)$$

where, m is the slope of the linear function $\beta(T)$. Then

$$n_{th} = \frac{\alpha_1(T) + \alpha_0 + \alpha_m + \beta n_{tr}}{\beta_0 - \gamma - mT} \quad (3.3.6)$$

or

$$n_{th} = \frac{\alpha_1(T) + \alpha_0 + \alpha_m + \beta n_{tr}}{m((\beta_0 - \gamma) / m - T)} = \frac{\alpha_1(T) + \alpha_0 + \alpha_m + \beta n_{tr}}{m(T_{max} - T)} \quad (3.3.7)$$

where

$$T_{max} = (\beta_0 - \gamma) / m \quad (3.3.8)$$

and is temperature independent. When T approaches T_{max} , n_{th} approaches infinity, thus, T_{max} may be regarded as a maximum temperature of operation of the laser. β and n_{tr} are linear functions of temperature. $\alpha_1(T)$, though it is difficult to formulate as a function of temperature, is expected to be only weakly temperature dependent [Zou, 1993]. α_0 and α_m are temperature independent. Therefore, the numerator in (3.3.7) can be approximated as a polynomial function of temperature to the second order.

The relationship between I_{th} and n_{th} in the quantum well lasers can be written as [Taylor, 1992] [Li, 1995] :

$$I_{th} = \frac{qVn_{th}}{\eta_i \tau} \quad (3.3.9)$$

where, V , q , and η_i are the active region volume, the electronic charge, and the internal quantum efficiency, respectively. The constant τ is defined as [Li, 1995]:

$$\tau^{-1} = (A_{nr} + Bn_{th} + Cn_{th}^2) \quad (3.3.10)$$

where A_{nr} and C describe nonradiative recombinations due to bulk or surface states and Auger processes, respectively, while B is the radiative recombination coefficient, and is assumed to be inversely proportional to n_{th} [Zou, 1993]. Compared to Bn_{th} , Cn_{th}^2 can be ignored [Bernussi, 1995][Seki, 1995]. Hence, I_{th} can be written as

$$I_{th} = qVB'n_{th} / \eta_i = qVB' \frac{\alpha_1(T) + \alpha_0 + \alpha_m + \beta n_{tr}}{m\eta_i(T_{max} - T)} \quad (3.3.11)$$

where, $B' = A_{nr} + Bn_{th}$, which, though difficult to formulate as a function of temperature, is expected to be weakly temperature-dependent [Dutta, 1983]. In (3.3.11), the numerator is a complicated temperature dependent function, which is expressed as $f(T)$, therefore, (3.3.11) becomes

$$I_{th} = \frac{f(T)}{T_{max} - T} \quad (3.3.12)$$

It is noted that the every term in the loss equation $\alpha_1(T) + \alpha_0 + \alpha_m$ makes a contribution to I_{th} , which is also modified by the factor $1/(T_{max} - T)$. Thus, when T approaches T_{max} , I_{th} approaches infinity. Therefore, a reduction of the cavity loss of a laser would reduce I_{th} dramatically at high temperature. βn_{tr} is the loss term of the

interband absorption at transparency, and can be a dominant term in determining the threshold current. The introduction of strained quantum wells into semiconductor laser structures dramatically reduces n_{tr} and then, the related interband loss βn_{tr} . Therefore, by (3.3.11) it could dramatically reduces I_{th} . In this thesis, a second order polynomial function of temperature is used for $f(T)$ to fit (3.3.12) to experimentally extracted I_{th} vs. T data.

The temperature sensitivity of I_{th} is defined as[Taylor, 1992][Evans, 1994]

$$\begin{aligned} \frac{1}{I_{th}(T)} \frac{dI_{th}(T)}{dT} &= \frac{1}{f(T)} \frac{df(T)}{dT} + \frac{1}{T - T_{max}} \\ &= \frac{\eta_i}{B'} \frac{d(B' \eta_i)}{dT} + \frac{1}{\alpha_1(T) + \alpha_0 + \alpha_m + \beta n_{tr}} \frac{d(\alpha_1(T) + \beta n_{tr})}{dT} + \frac{1}{T - T_{max}} \end{aligned} \quad (3.3.13)$$

The right hand side of (3.3.13) consists of three terms. The first term contains the temperature dependence of the internal quantum efficiency and the recombination coefficient B' . The second term is due to the internal loss and includes the interband transition loss at the transparency. It shows that the larger residual loss α_0 introduced by heavily doping active layer could reduce the temperature sensitivity, as experimentally observed[Zah, 1994]. The last term is from the fundamental properties, such as differential gain coefficient, of the laser, which set an upper limit to the high temperature sensitivity. Obviously, the temperature sensitivity defined by (3.3.13) is temperature-dependent, as observed experimentally, but in terms of (3.2.1), the temperature sensitivity is a constant T_0 .

3.4 Experimental Results and Discussion

The semiconductor lasers studied are 0.7% compressive SL-MQW lasers containing 5 to 14 quantum wells, whose structure are described in chapter 2. The nominal emission wavelength of the lasers is $1.3\mu\text{m}$ at room temperature, and a typical optical spectrum is shown in Fig.3.4.1. The reflection coefficient r can be calculated from the formula $r=(n_{\text{eff}}-1)/(n_{\text{eff}}+1)$, where the n_{eff} is the effective refractive index. n_{eff} can be obtained by the formula $n_{\text{eff}}=\lambda^2/(2\Delta\lambda L)$, where λ is the emission wavelength, $\Delta\lambda$ is the peak separation on the measured spectrum and L is the length of the laser. From Fig.3.4.1, λ is $1.311\mu\text{m}$, and $\Delta\lambda=0.4492\text{nm}$; then, $r=0.5856$, the reflectivity $R=0.3429$, and the mirror loss $\alpha_m=21.41(1/\text{cm})$ for a $500\mu\text{m}$ long laser with ten 0.7% compressive-strain quantum wells. The lasers were tested in CW and pulsed mode in which the heating in the laser is minimized.

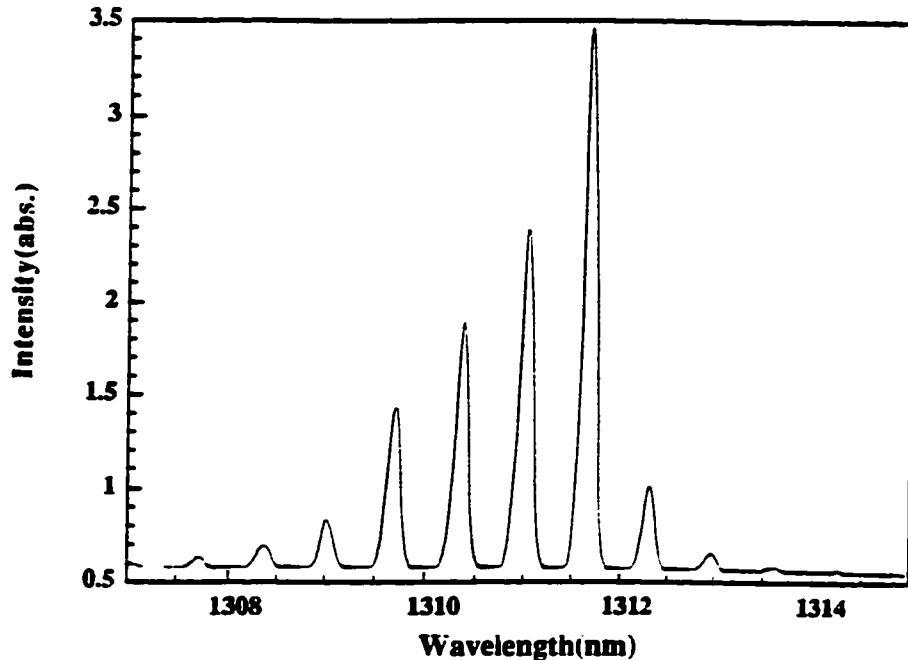


Fig. 3.4.1 A room temperature optical spectrum of a 0.7% compressive SL-MQW laser, which contains 10 quantum wells and is $500\mu\text{m}$ long. The spectrum shows a multiple longitudinal modes.

3.4.1 Experimental Characterization Under CW Operation

Figure 3.4.2 shows a typical L-I curves under CW operation of 0.7% compressive SL-MQW laser containing 5 wells. The L-I curves show premature roll-over at about 370K. The premature roll-over causes no damage to the laser. A theoretical model to explain the CW L-I roll-over is developed in Chap.7. It is the heating during CW operation that causes the premature roll-over. Thus, extra caution should be exercised in interpreting experimental data from the CW L-I curves. The heating during CW operation may seriously distort the true characteristics of the laser.

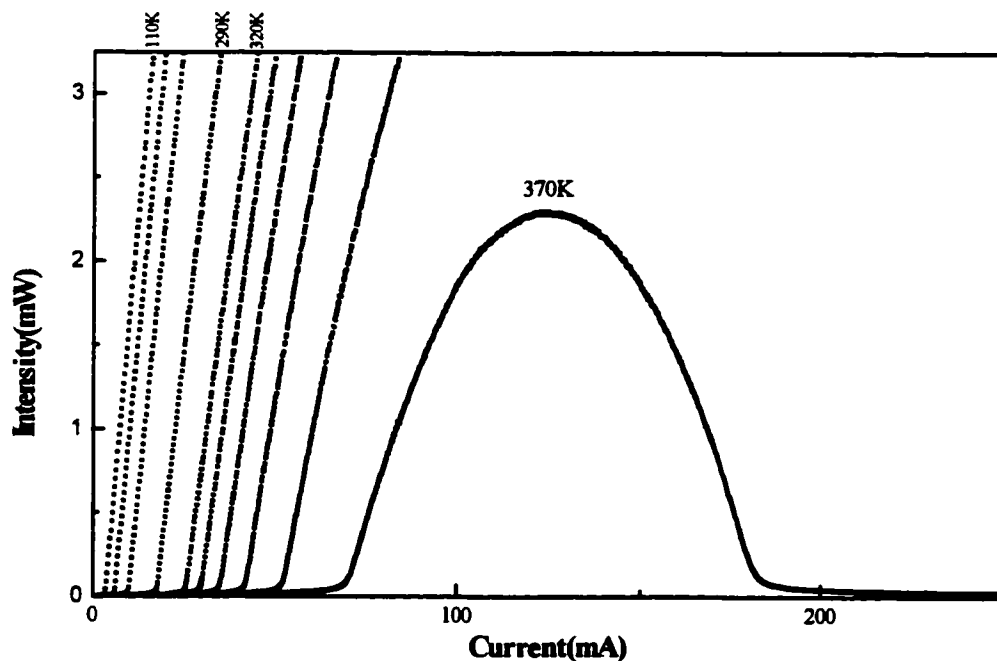


Fig. 3. 4.2 The L-I curves for 0.7% compressive SL-MQW laser containing 5 wells under CW operation. The premature roll-over is seen at 370K

Figure 3.4.3 illustrates the maximum operation temperatures of 0.7% compressive SL-MQW lasers containing 5 to 14 wells. The maximum temperature for CW operation is here defined as the roll-over temperature with 3mW maximum intensity, which is much lower than the corresponding T_{\max} under pulse operation (see next section).

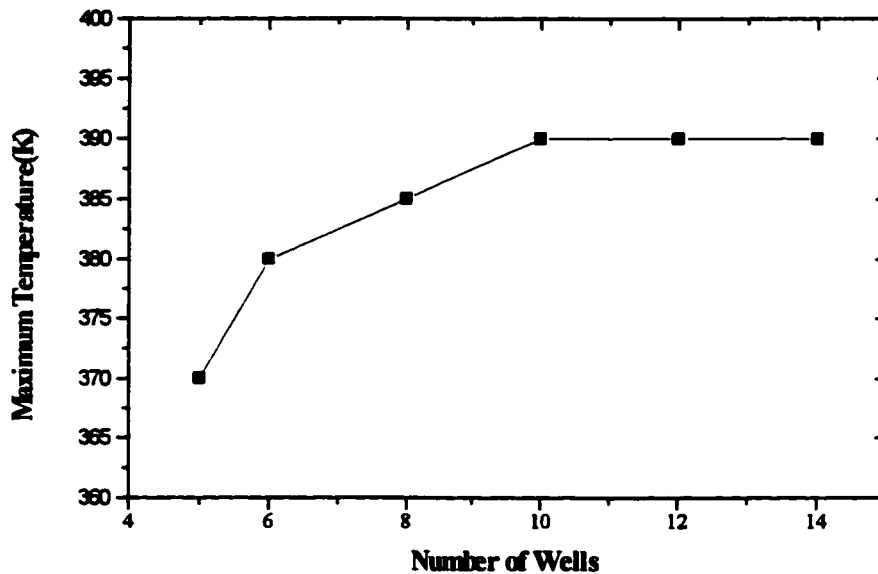


Fig. 3.4.3 The maximum operation temperature vs. the number of wells under CW operation

3.4.2 Experimental Results Under Pulse Operation

Figure 3.4.4 illustrates typical light-current (L-I) curves under pulse operation from 110K to 465K. I_{th} increases, and η_d (which is proportional to the slope of the curve above threshold) decreases with increasing temperature. In order to extract I_{th} and η_d from each L-I curve, the least squares method was applied to a set of current-

intensity points, which were selected by the criteria that the intensity is larger than one-tenth and less than one-third of the maximum intensity.

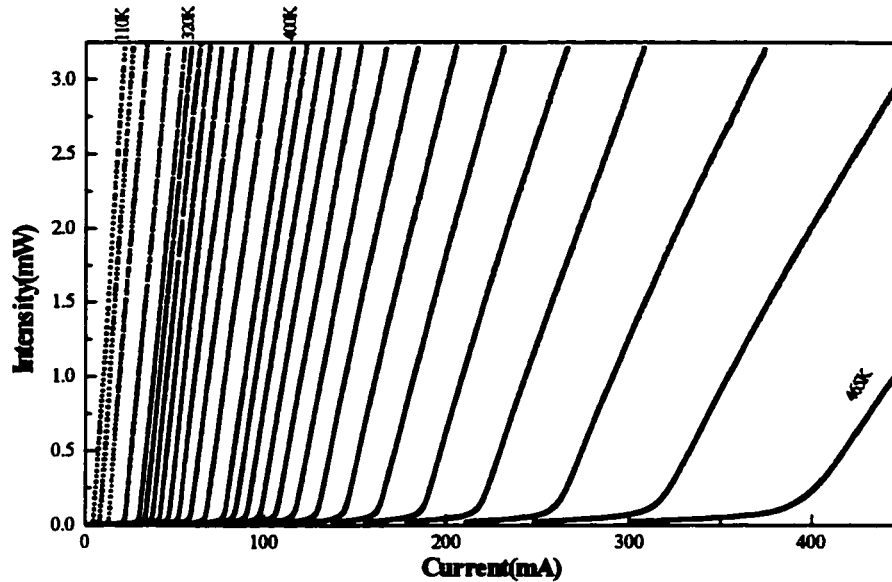


Fig.3.4.4 A typical L-I curves for a 500 μ m long 10 wells 0.7% compressive strain InGaAsP/InP laser under pulse operation (100ns @ 10KHz). The highest operation temperature in this graph is 465K.

Figure 3.4.5 illustrates the I_{th} vs. T data for 0.7% compressive SL-MQW lasers with varying well number from 5 to 14 and of length 500 μ m. The solid curves are fitted curves using equation (3.3.12). The formula fits the experimental results fairly well over the whole temperature range. The maximum operation temperature T_{max} and the room temperature sensitivity T_0 of the threshold current defined by (3.2.1) for all different number well lasers are listed in Tab.3.4.1 (T_0 is obtained by fitting (3.2.1) to the I_{th} vs. T data from 260K to 320K). The trend is that T_0 increases with the well number, and saturates for the well number above 10. The maximum

operation temperatures increases from 430K for five-well laser to 480K for ten-well laser and saturates for higher numbers of wells, in accordance with the available results [Oohashi, 1995].

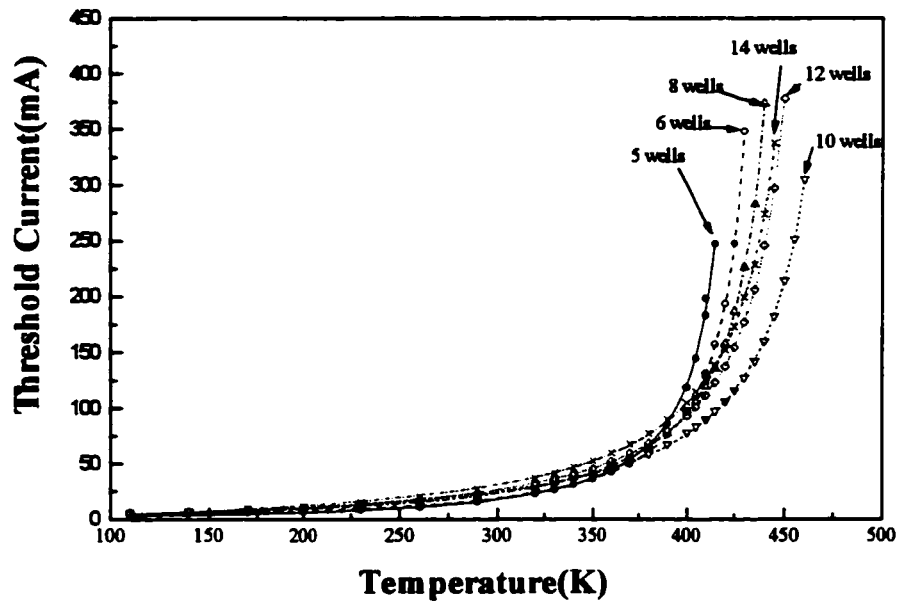


Fig.3.4.5 The experimental threshold current vs. temperature data of 500 μ m long 0.7% compressive SL-MQW lasers ranging in well number from 5 to 14. The solid curves are the fitting curves from the formula (3.3.12).

Tab.3.4.1. The room temperature T_0 and the T_{max} for different number well lasers

well number	5 wells	6 wells	8 wells	10 wells	12 wells	14 wells
T_{max}	431.4	443.8	456.7	489.5	471.1	468.6
T_0	73.0	79.6	81.1	89.5	89.4	91.7

Figure 3.4.6 illustrates I_{th} vs. T data for 0.7% compressive SL-MQW lasers containing 14 wells with cavity length varying from $250\mu\text{m}$ to $1000\mu\text{m}$. The solid lines are fitting curves obtained by using (3.3.12). The mirror loss ($=\ln(1/R)/L$) is inversely proportional to the length of the lasers. The internal loss ($\alpha_1(T)+\alpha_0+\beta n_{tr}$) is not dependent on the length of the laser. Therefore, according to (3.3.12) (V is the volume of the active region of the laser, and is proportional to the length of the laser) I_{th} increases linearly with the length of the laser cavity, which is consistent with the experimental observation, as shown in Fig. 3.4.7. The solid lines are the linear fitting curves.

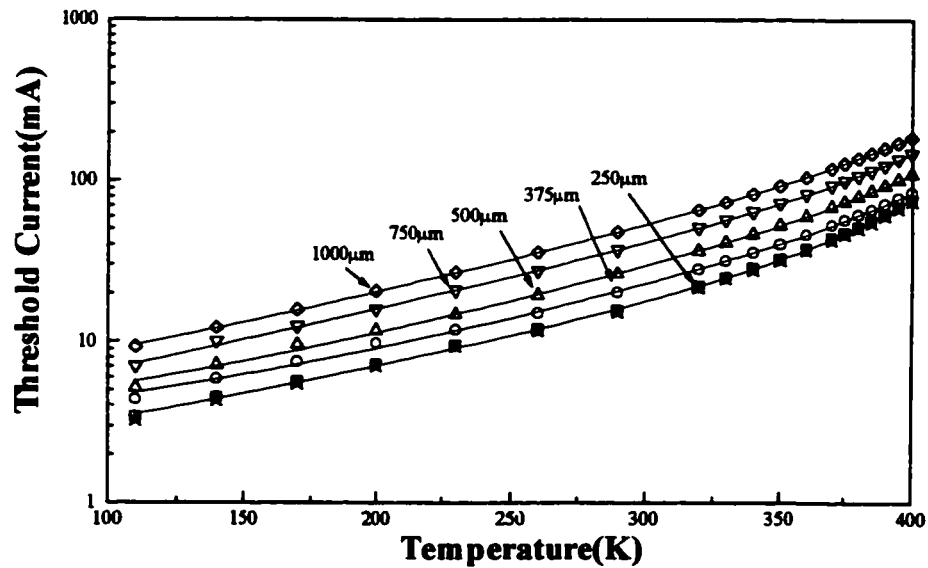


Fig.3.4.6. The experimental results of the threshold current with temperature for 14 wells compressive SL-MQW lasers with variant cavity length. The solid lines are the fitting curves from equation (3.3.12)

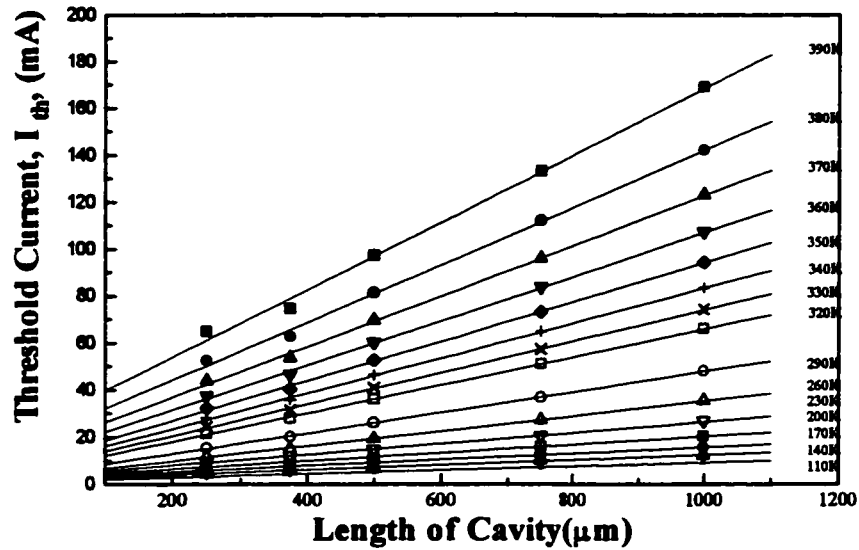


Fig.3.4.7 The length dependence of the threshold currents for 14 wells compressive SL-MQW lasers at various temperature with the linear fitting lines

T_{\max} values, which were extracted from fitting (3.3.12) to the experimental I_{th} vs. T data, for 14 wells 0.7% compressive SL-MQW lasers with varying cavity length are shown in the Fig.3.4.8. No evident cavity length dependence of the maximum operation temperature exists, which is consistent with the theoretical prediction.

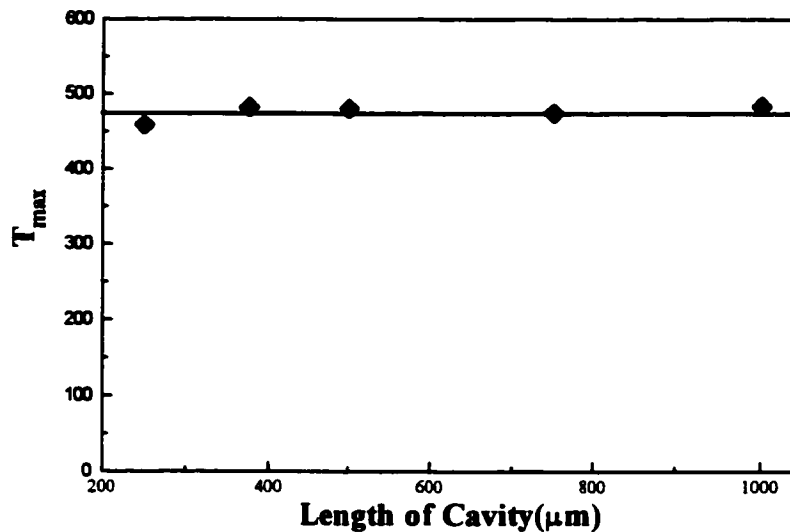


Fig.3.4.8 T_{\max} as a function of cavity length for the different length 14 wells 0.7% compressive SL-MQW lasers. As predicted by theory, no length dependence is evident.

3.5 Conclusions

A formula is derived to describe the I_{th} vs. T relation based on the assumptions that the decrease of the optical gain with temperature plays a dominant role in determining the temperature sensitivity of the threshold current, that the linear gain coefficient decreases linearly with temperature, and that Auger recombination is negligible in laser processes. A maximum operation temperature T_{\max} is naturally included in the formula, and is related to the gain coefficient. The formula was applied to the experimentally determined I_{th} vs. T results for 0.7% compressive SL-MQW $2\mu\text{m}$ wide ridge waveguide uncoated Fabry-Perot lasers, which contain 5 to 14 quantum wells. It was found that the derived formula fits the experimental results very

well over the temperature range 110K to 465K. T_{\max} was found to depend on the quantum well number, and increases from 430K for 5 quantum wells to 480K for 10 quantum wells lasers. T_{\max} was found to be independent of the cavity length of lasers, which is consistent with the theoretical prediction.

Chapter 4

TEMPERATURE SENSITIVITY OF THE EXTERNAL QUANTUM EFFICIENCY

4.1 Introduction

Substantial effort has been devoted to reducing the magnitude of the threshold current. Reductions have been achieved through improvement in material quality made possible by the introduction of more and more sophisticated crystal growth technologies (MOCVD, MBE) and the use of strain layer quantum well structures [Henry, 1993] [Lau, 1993] [Coleman, 1993]. However, in contrast to I_{th} , the external quantum efficiency, η_d , has not attracted much attention yet, even though it is just as important a parameter as I_{th} [Nabiev, 1995]. As a consequence, there are virtually no functional formulae to describe the η_d vs. T .

The external quantum efficiency η_d , which is experimentally determined by the slope of a L-I curve above threshold, is conventionally defined as:

$$\eta_d = \eta_i \frac{\alpha_m}{\alpha_i + \alpha_m} \quad (4.1.1)$$

where η_i is the internal quantum efficiency, α_i is the internal cavity loss, and α_m is the mirror loss. Physically speaking, η_i is the ratio of the number of electrons that are

converted into the laser light to the total number of electrons injected into the laser. The light in the cavity is partially emitted from the laser facets, and the remainder is lost within the laser cavity. Intuitively, it would be expected that the physical processes that affect the I_{th} would also affect η_d . In this chapter, based on the same assumptions used to obtain the I_{th} vs. T relationship (3.3.12), we will develop an expression for η_d vs. T .

4.2 Theoretical Analysis of External Quantum Efficiency

η_d is expressed in the form:

$$\eta_d = \eta_i \frac{\alpha_m}{\alpha_i + \alpha_m} \quad (4.1.1)$$

where $\alpha_i + \alpha_m$ is the total loss, as defined in (3.3.2). Therefore, at threshold α_i is defined by the following equation::

$$\alpha_i = \gamma n_{th} + \alpha_1(T) + \alpha_0 \quad (4.2.1)$$

By substituting (3.3.4) into (4.2.1) and then, substituting (4.2.1) into (4.1.1), we obtain

$$\eta_d = \eta_i \frac{\alpha_m}{\gamma n_{th} + \alpha_1(T) + \alpha_0 + \alpha_m} = \eta_i \frac{\alpha_m (\beta - \gamma)}{\beta (\alpha_1(T) + \alpha_0 + \alpha_m + \gamma n_{tr})} \quad (4.2.2)$$

Substituting (3.3.5) for β in (4.2.2) gives

$$\eta_d = \eta_i \frac{\alpha_m (T_{\max} - T)}{(\beta_0 / m - T)(\alpha_1(T) + \alpha_0 + \alpha_m + \gamma n_{tr})} \quad (4.2.3)$$

where

$$T_{\max} = (\beta_0 - \gamma) / m \quad (4.2.4)$$

as defined for I_{th} in (3.3.8).

In (4.2.3), the denominator includes the differential gain coefficient β , which decreases at a slower rate than $(T_{\max} - T)$. Therefore, when the temperature approaches the maximum temperature T_{\max} , the external quantum efficiency η_d approaches zero. Thus, η_d has the same T_{\max} as I_{th} , and provides a powerful tool to verify the concept of T_{\max} , and hence the underlying assumptions.

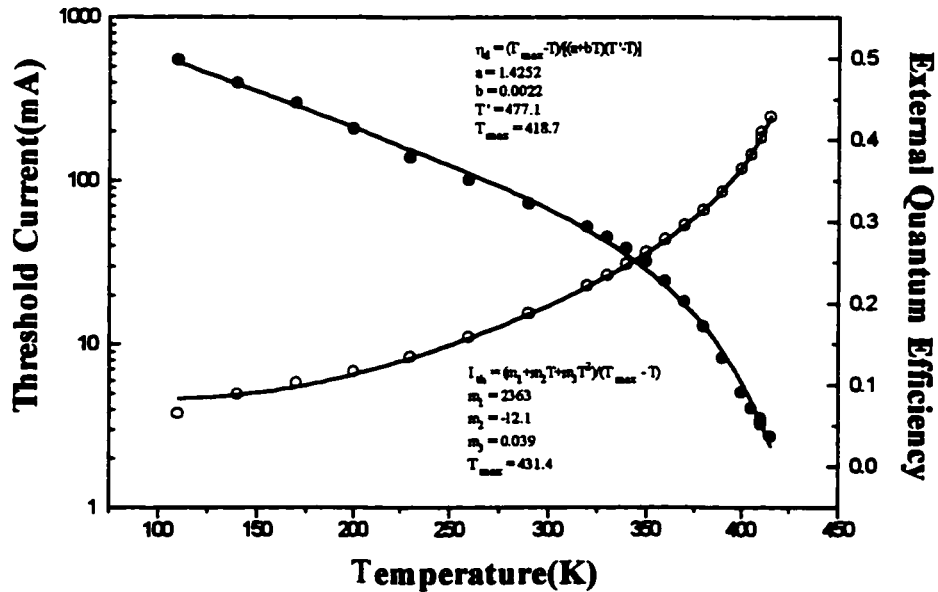
4.3 Experimental Results and Discussion

The η_d vs. T data with temperature as a parametric variable are presented in Fig. 4.3.1(a-f) for various numbers of quantum wells. The corresponding I_{th} vs. T characteristics are also presented. It is seen that η_d decreases steadily from 110K to around 400K and then the decrease accelerates above 400K.

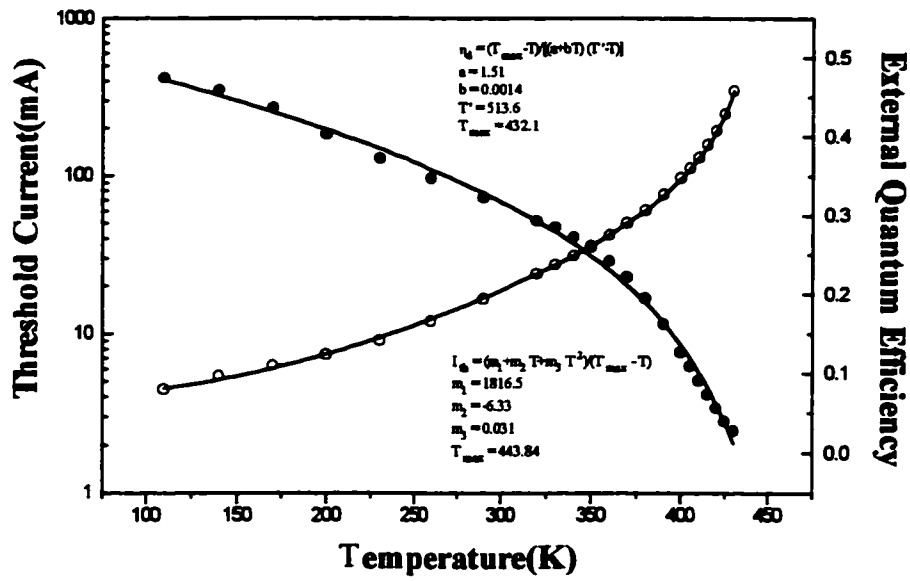
In order to fit (4.2.3) to the experimental data, some assumptions should be made. First, η_i and α_m are assumed to be independent of temperature; second, since n_{tr} is a linear function of temperature [Yariv, 1988] [Zah, 1994], the term $(\alpha_1(T) + \alpha_0 + \alpha_m + \gamma n_{tr}) / (\eta_i \alpha_m)$ is approximated by a linear function of temperature $a + bT$. Thus, (4.2.3) becomes

$$\eta_d = \frac{T_{max} - T}{(\beta_0 / m - T)(a + bT)} = \frac{T_{max} - T}{(T' - T)(a + bT)} \quad (4.3.1)$$

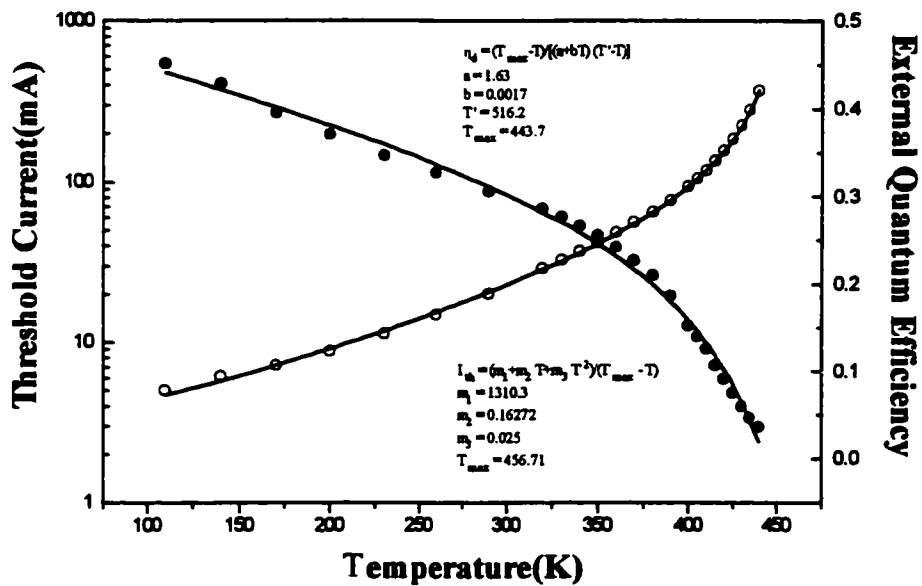
where T' is β_0/m . The solid lines in Fig.4.3.1 are the fitting curves according to (3.3.12) for I_{th} vs. T data and (4.3.1) for η_d vs. T data. It is seen that they compare very favorably with the experimental data over the entire temperature range studied. The parameters used in the threshold current and the external quantum efficiency fitting are listed in Table 4.3.1, which are statistical data from a set of tested lasers.



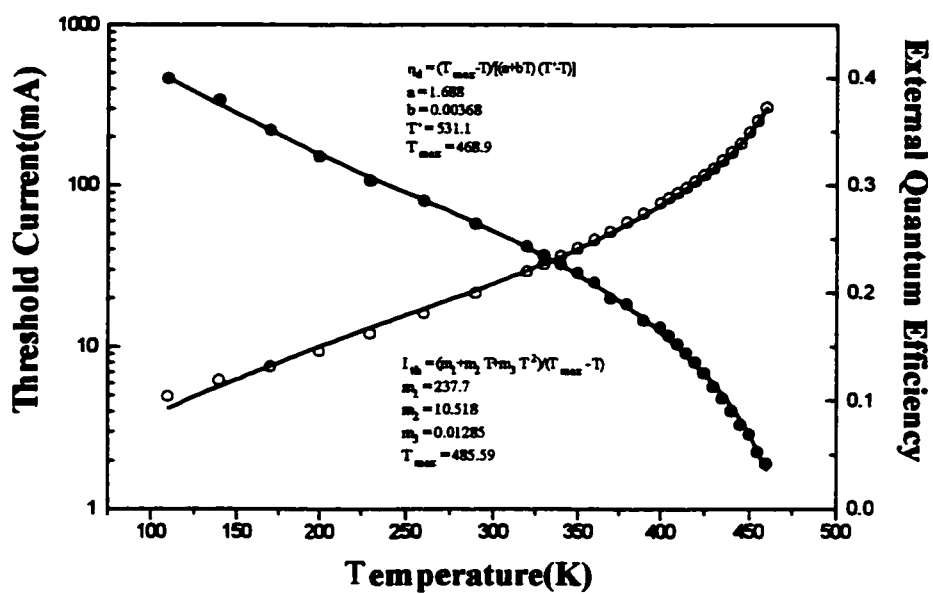
(a)



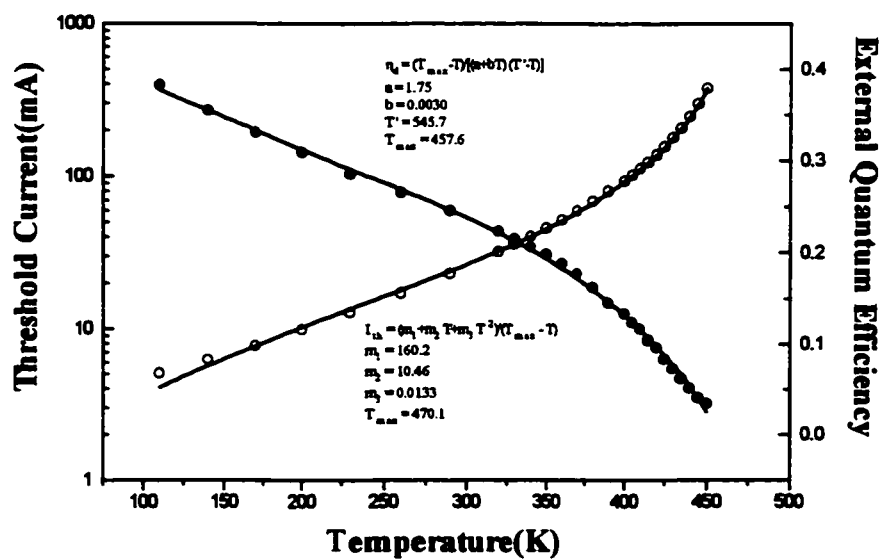
(b)



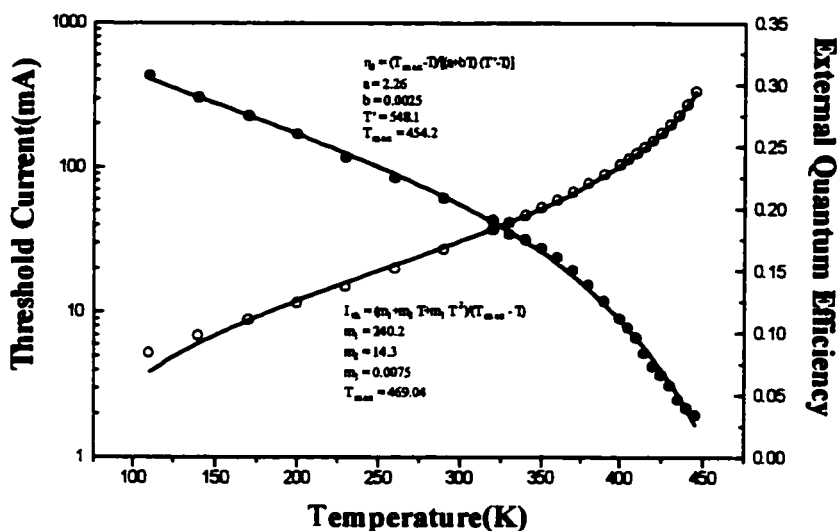
(c)



(d)



(e)



(f)

Fig.4.3.1 η_d and I_{th} vs. T for 5 well(a), 6 wells(b), 8 wells(c), 10 wells(d), 12 wells(e) and 14 wells(f). All lasers are $500\mu\text{m}$ long. The solid curves are the fitting curves and the insets show the fitting parameters.

Table 4.3.1 The parameters used in η_d vs T and I_{th} vs T fitting for different number well lasers

No. of well	5	6	8	10	12	14
a	1.4252	1.6267	1.7636	1.8409	1.8878	2.4394
b	0.0022	0.0015	0.0019	0.0025	0.0032	0.0027
T'	477.13	510.62	512.17	530.92	546.73	549.13
$T_{max}(\eta_d)$	418.72	435.13	448.70	467.89	460.55	464.15
$T_{max}(I_{th})$	431.43	446.84	458.71	482.51	476.07	480.56

The T_{max} values obtained from fitting the η_d vs. T and the I_{th} vs. T data for different number well lasers are shown in Fig.4.3.2. It is seen that T_{max} initially increases, saturates, and then decreases with the number of wells.

Although the T_{\max} values obtained from the η_d vs. T and the I_{th} vs. T data are within $\sim 2\%$ of each other, the former data are systematically lower than the latter. A possible reason for that discrepancy is shown schematically in Fig.4.3.3. Though the pulse is short (as used here 100ns), heating is inevitable when a laser is applied a driving current. Especially at high temperature, the driving current and the temperature sensitivity of the threshold current and the external quantum efficiency are very high. Because of heating, the true temperature of the laser increases with increasing driving current instead of remaining fixed at the set temperature T_1 . If I_{th} and η_d are determined graphically, heating affects I_{th} and η_d unequally. From Fig.4.3.3, The heating caused by the driving current above an elbow point reduces η_d and I_{th} simultaneously, then it is seen that the heating affects η_d more than it does I_{th} . Thus, T_{\max} obtained by fitting the η_d vs. T data is smaller than that obtained from the I_{th} vs. T data.

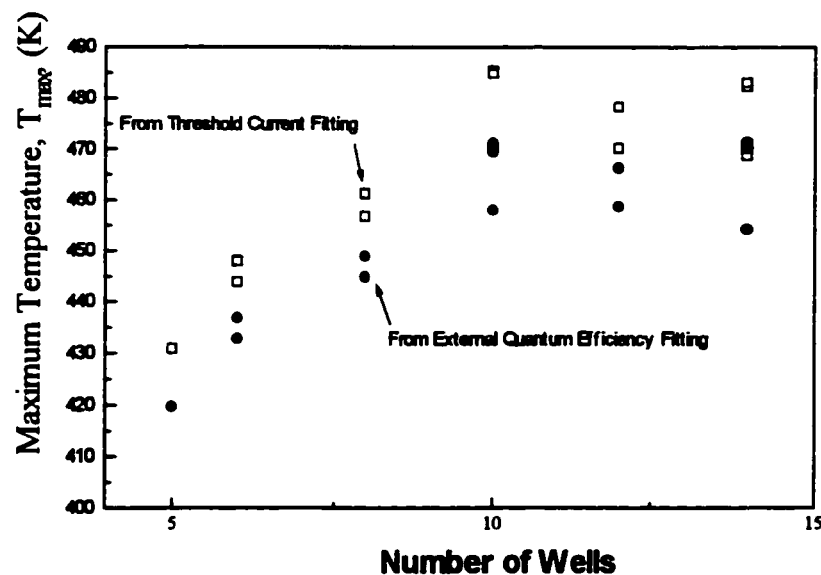


Fig.4.3.2 T_{\max} deduced from η_d vs. T and I_{th} vs. T experimental data.

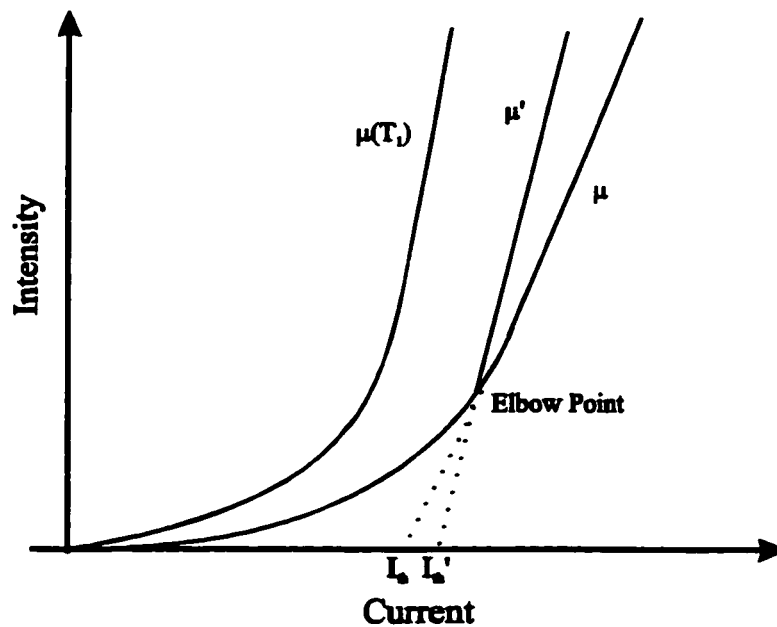


Fig. 4.3.3 A schematic illustration of the determination of I_{th} and η_d by the conventional method, with and without heating. Heating affects the threshold current less than the external quantum efficiency.

Because $a+bT$ represents $(\alpha_1(T)+\alpha_0+\alpha_m+\gamma n_{tr})/(\eta_i \alpha_m)$, the parameters a and b , which describes the linear temperature dependence of the internal loss, increase approximately with the number of wells.

The derived formula that describes the external quantum efficiency as function of temperature fits the experimental results quite well. The fact that the maximum temperature obtained by fitting the threshold current vs. temperature data agrees with the maximum temperature obtained by fitting the external quantum efficiency vs. temperature data verifies the two assumptions used in deriving (3.3.12) and (4.2.3).

4.4 Conclusions

The external quantum efficiency is as important a parameter as the threshold current in characterizing a semiconductor laser, however, it has not attracted as much attention as the threshold current. It is widely known that the external quantum efficiency decreases with temperature, however, it is not known whether a temperature limit exists for the external quantum efficiency. In this chapter, under the assumption that the differential gain coefficient decreases linearly with temperature, a formula was developed to describe the relation of external quantum efficiency with temperature. It includes the same maximum temperature as is included in the formula describing the threshold current as a function of temperature. By analyzing the experimentally extracted threshold current and external quantum efficiency for 1.3 μm compressive-strain multiple quantum well lasers at different temperatures, a maximum operating temperature for both threshold current and external quantum efficiency is experimentally verified. The excellent agreement between the theory and the experimental data indicates that the poor temperature performance of long wavelength semiconductor lasers originates from rapid deterioration of the differential gain with temperature. To my knowledge, this is first time for a formula has been developed to describe the relation between external quantum efficiency and temperature. This formula will be used in chapter 7 to derive the temperature rise during CW operation.

Chapter 5

INTERNAL QUANTUM EFFICIENCY AND INTERNAL LOSSES

5.1 Introduction

Unlike the I_{th} and the η_d , which can be determined from an L-I curve, the internal quantum efficiency, η_i , and the internal loss, α_i , which are intrinsic physical properties of a semiconductor laser, can not be directly determined from the L-I curve. η_i is a measure of the fraction of carriers that are converted into light. There are several physical processes that affect the internal quantum efficiency. Of these the leakage of the injected carriers into the confinement layers due to thermionic emission [Yano, 1980, 1981], nonradiative Auger recombination processes [Dutta, 1982] [Lui, 1993], and the carrier overflow into waveguiding layer were frequently cited [Casey, 1984] [Chik, 1990].

Conventionally, η_i and α_i are extracted from the relationship between the external quantum efficiency and device length in a set of lasers that vary in length but otherwise are equivalent. If the α_i includes a carrier-density dependent term, as defined in (3.3.2), then, as pointed out by Koren and Tanaka [Koren, 1987][Tanaka, 1995], the η_i determined in this manner is not the true internal quantum efficiency, but a *nominal* quantum efficiency.

Another method for determining α_i is according to [Ackerman, 1995]:

$$G = g - \alpha_{\text{total}} \quad (5.1.1)$$

in which G is the modal gain, and g is the material gain. At transparency, the g is zero and the modal gain is equal to the total loss α_{total} . The total loss determined by this method is:

$$\alpha_{\text{total}} = \gamma n_{\text{tr}} + \alpha_l(T) + \alpha_o + \alpha_m \quad (5.1.2)$$

which is exactly equal to the total loss determined by the conventional method. After knowing the total loss, the internal quantum efficiency is then determined by:

$$\eta_i^{-1} = \frac{1}{\eta_d} \frac{\alpha_m}{\alpha_i + \alpha_m} \quad (5.1.3)$$

The value for η_i determined in this way is exactly equal to one determined by the conventional method, which is a *nominal* internal quantum efficiency.

In this chapter, the same assumptions as were used in previous chapters are used to analyze the nominal internal quantum efficiency and the internal loss determined by the conventional method. The formula is developed for the nominal internal quantum efficiency. Even if the true internal quantum efficiency is assumed temperature independent, the nominal internal quantum efficiency is a strong function of temperature. Therefore, one must be careful to explain the experimentally determined internal quantum efficiency versus temperature results.

5.2. Theoretical Analysis of Internal Quantum Efficiency and Internal Loss

As presented in Chap. 4, the external quantum efficiency η_d can be written as:

$$\eta_d = \eta_i \frac{\alpha_m(\beta - \gamma)}{\beta(\alpha_1(T) + \alpha_0 + \alpha_m + \gamma n_{tr})} \quad (5.2.1)$$

or

$$\eta_d^{-1} = \eta_i^{-1} \frac{\beta(\alpha_1(T) + \alpha_0 + \gamma n_{tr})}{(\beta - \gamma) \ln(1/R)} L + \eta_i^{-1} \frac{\beta}{\beta - \gamma} \quad (5.2.2)$$

Thus, a η_d^{-1} vs. L plot has an intersection with the η_d^{-1} axis given by $\eta_i^{-1} \beta / (\beta - \gamma)$, and not η_i^{-1} , as would usually be expected.

Writing $\eta_i^N = \eta_i (\beta - \gamma) / \beta$, then (5.2.2) becomes

$$\eta_d^{-1} = (\eta_i^N)^{-1} \frac{\alpha_1(T) + \alpha_0 + \gamma n_{tr}}{\ln(1/R)} L + (\eta_i^N)^{-1} \quad (5.2.3)$$

Apart from a new loss term, γn_{tr} , (5.2.3) exactly looks like the equation that is widely used without considering carrier density related loss γn_{th} at threshold.

Substituting (3.3.5) in the definition of η_i^N , we obtain

$$\eta_i^N = \eta_i \frac{\beta_0 - \gamma - mT}{\beta_0 - mT} = \eta_i \frac{(\beta_0 - \gamma) / m - T}{\beta_0 / m - T} = \eta_i \frac{T_{max} - T}{T' - T} \quad (5.2.4)$$

where $T_{\max}=(\beta_0-\gamma)/m$ and $T'=\beta_0/m$, as defined in Chap. 4. According to (5.2.4), even if the true internal efficiency η_i is temperature independent, the nominal internal efficiency is strongly temperature dependent and approaches to zero when the temperature approaches the maximum temperature T_{\max} . The internal loss is determined by dividing the slope by the intersection of η_d^{-1} vs. L plot. From (5.2.3), then

$$\alpha_i = \alpha_1(T) + \alpha_0 + \gamma n_{tr} \quad (5.2.5)$$

$\alpha_1(T)$ is expected a weak temperature dependency, γ is temperature independent, and n_{tr} is linearly temperature dependent [Yariv, 1988] [Zah, 1995] and given by

$$n_{tr} = AT \quad (5.2.6)$$

Substituting (5.2.6) into (5.2.5), then (5.2.5) becomes

$$\alpha_i = \alpha_1(T) + \alpha_0 + \gamma AT \quad (5.2.7)$$

for quantum well laser. Since $\alpha_1(T)$ is assumed to be weakly temperature dependent, the measured loss α_i is expected to have an approximately linear temperature dependence, as experimentally shown [Zou, 1993]. At low temperature, the transparent carrier density n_{tr} is low, and compared to the free carrier loss, γn_{tr} , the loss $\alpha_1(T)$ may not be ignored. Thus, the linearity of the temperature dependence of the internal loss α_i may not hold at low temperature.

5.3. Experimental Results and Discussions

The lasers investigated in this chapter contain ten 0.7% compressive strain quantum wells. The lasers vary in length, but are assumed to be equivalent otherwise. The device structure has been detailed in Chap. 2.

Figure 5.3.1 shows the I_{th} vs. T and η_d vs. T data for three different length lasers. The solid lines are fitting curves for the threshold current using (3.3.11), in which a polynomial to the second order is assumed for $f(T)$, and the external quantum efficiency using (4.3.1). It is seen that they compare very favorably with the experimental data over the entire temperature range studied. The fitting parameters are listed in Table 5.3.1.

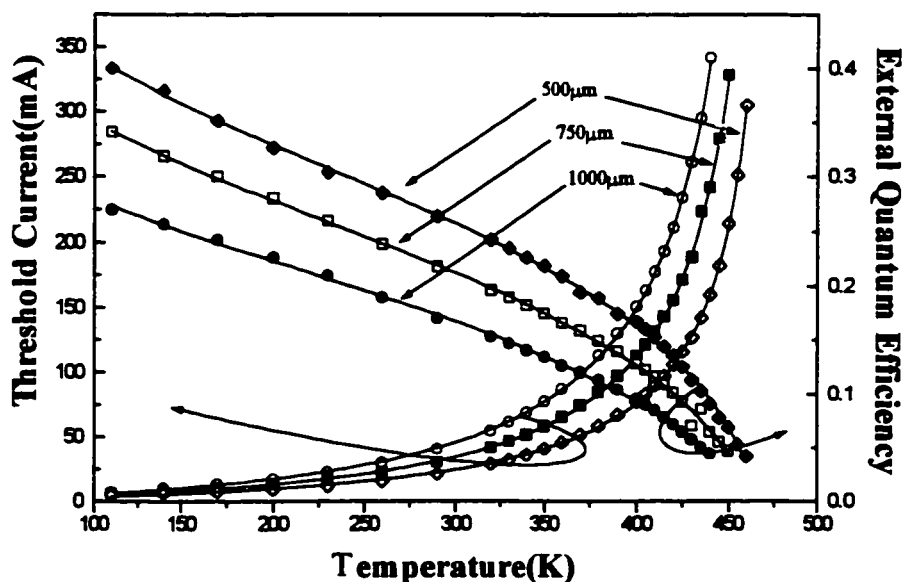


Fig.5.3.1 The I_{th} vs. T and the η_d vs. T for 500 μm , 750 μm and 1000 μm long lasers with ten 0.7% compressive SL-MQW lasers. The dashed lines are fitting curves for the threshold current by (3.3.11) and the external quantum efficiency by (4.3.8)

Table 5.3.1. Fitting Parameters Used for Fig. 5.3.1

Length(μm)	500	750	1000
a	1.84	1.98	2.14
b	0.00256	0.00377	0.00497
T'(K)	531	563	560
$T_{\text{max}}(\eta_d)$ (K)	468	467	463
$T_{\text{max}}(I_{\text{th}})$ (K)	483	484	481

All three external quantum efficiency curves show a sharp decrease beyond 400K. The values of T_{max} for 500 μm , 750 μm , and 1000 μm long lasers from the threshold current fitting are 483, 484 and 481K, respectively. The minor differences among the maximum temperatures should be regarded as the consequence of possible physical and geometrical differences among the lasers and the heating effect, which exists especially at high temperature, at which the threshold current is high, even though short current pulses were used. The T_{max} vs. L plot is presented in Fig.5.3.2, in which it is seen that there is no apparent length dependence of T_{max} .

The internal loss, as determined by (5.2.3), is shown as a function of temperature in Fig.5.3.3. The loss curve separates into two regions of very different slope. The solid lines are a speculative allocation of total loss into two terms. $\alpha_1(T) + \alpha_0$ represents a weakly temperature dependent loss $\alpha_1(T)$ and a temperature independent α_0 . γAT stands for the free carrier related loss.

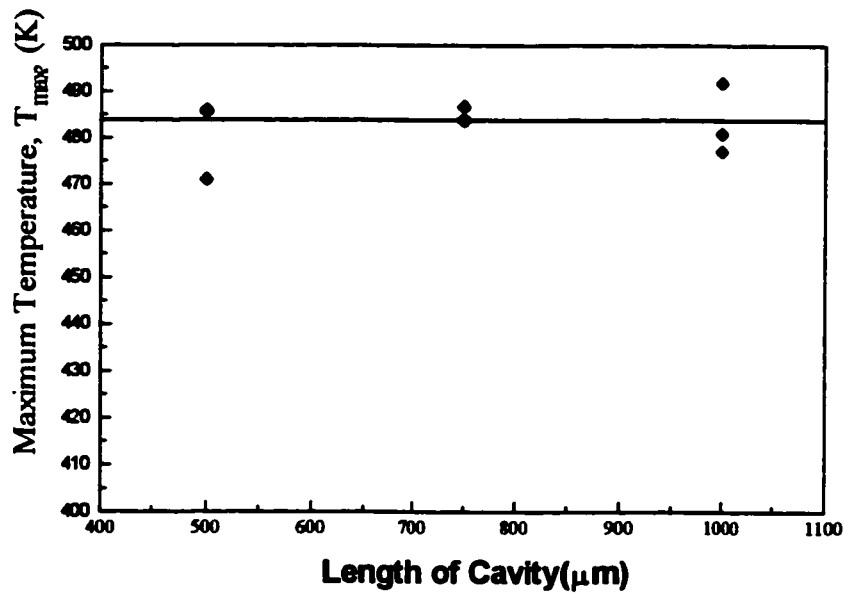


Fig.5.3.2. The length dependence of T_{\max} .

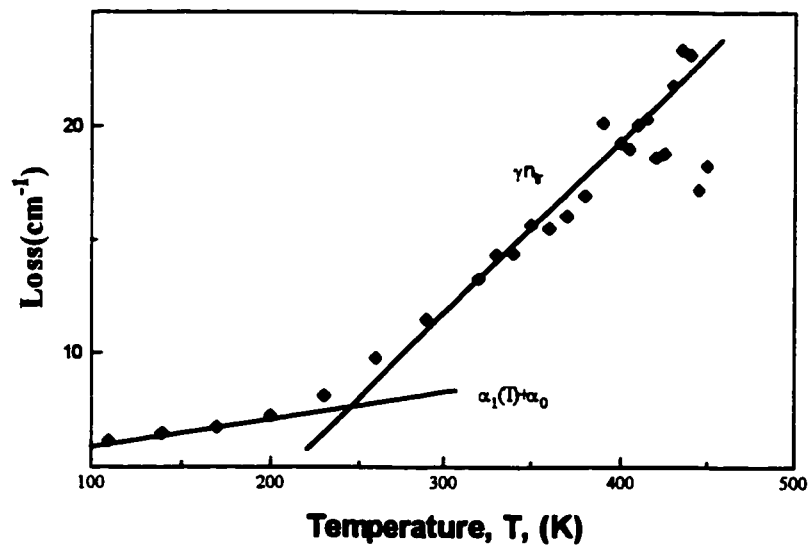


Fig.5.3.3 The total internal loss for 0.7% compressive SL-MQW laser containing ten wells. The lower line represents the loss $\alpha_1(T) + \alpha_0$, which is weakly temperature dependent. The upper line stands for the loss term γAT , which is due to free carrier scattering and intervalence band absorption.

The nominal internal quantum efficiency, as determined by (5.2.3), is presented as a function of temperature in Fig. 5.3.6. The solid line is the fitting curve using (5.2.4), assuming the internal efficiency η_i is a constant. The fit is reasonably good. The measured nominal internal efficiency shows sharp decrease around 400K, which matches the turning point on the external quantum efficiency versus temperature curve. The T_{\max} from the nominal internal efficiency fitting is 10 degrees less than the one derived from threshold current fitting. Equation (5.3.4) suggests that the external quantum efficiency's turning point around 400K is the result of the carrier density dependence of internal loss and the sharp decrease of differential gain with increasing temperature. The true internal quantum efficiency is very weakly temperature dependent, if at all.

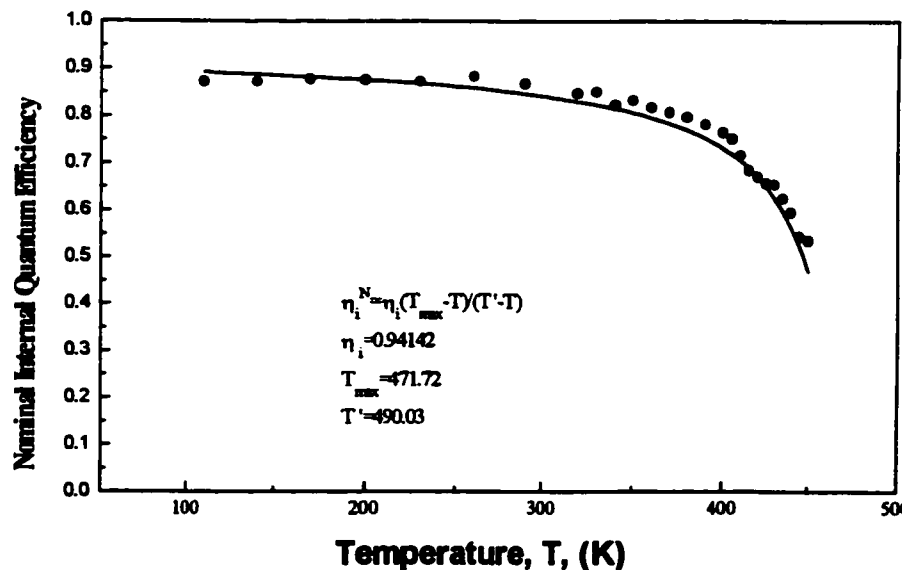


Fig. 5.3.6 η_i^N vs. T for lasers with ten 0.7% compressive strain quantum wells

5.5 Conclusions

In summary, using the same assumptions as were used in deriving the I_{th} vs. T and η_d vs. T relationships, we derived a formula for nominal internal efficiency, η_i^N , which is usually extracted from the relation of η_d^{-1} vs. L . The η_i^N is a strong function of temperature at high temperature, even though the true internal quantum efficiency, η_i is temperature independent. The η_i^N has the same maximum operation temperature as the threshold current and the external quantum efficiency.

Chapter 6

EXPERIMENTAL OBSERVATION OF FAR FIELD PATTERNS OF 1.3 μm TENSILE SL-MQW LASERS WITH VARYING RIDGE WIDTH

6.1 Introduction

In the previous three chapters, the threshold current, the external quantum efficiency, and the internal quantum efficiency were discussed. In this chapter, the emission pattern or far field, which is another important parameter for characterizing a semiconductor laser is studied for multiple quantum well ridge waveguide lasers with varying ridge width. The lasers that were studied operated at a wavelength of 1.3 μm and contained three 1.2% tensile strain quantum well.

The far field is associated with the internal cavity modes, which are determined by the laser cavity structure. Experimental observations and theoretical studies have been carried out mostly on broad-area lasers [Hohimer, 1988] [Champagne, 1989] [Lang, 1991] [Marciante, 1996] [Hess, 1996]. The broad area laser has no intentional lateral optical confinement structure. Optical confinement is provided by the injected carrier induced optical gain. The number of transverse modes, and, hence, the far field patterns vary with increasing injection current. In practical applications ridge

waveguide lasers, which have strong lateral optical confinement provided by lateral effective index variation, are used. To achieve single-mode operation, ridge widths of the order $2\mu\text{m}$ are required. However, only a relatively small amount of research has been carried out on the lateral far field patterns of ridge waveguide lasers [Wu, 1995]. In this chapter, an experimental study and theoretical analysis are presented on the temperature dependence of the lateral modes of $1.3\mu\text{m}$ tensile strained multiple quantum well ridge waveguide lasers with varying ridge width.

6.2 Experimental Concerns

The semiconductor lasers used in this study are $1.3\mu\text{m}$ 1.2% tensile SL-MQW lasers, whose structure was detailed in Chap 2. The experimental set-up for far field measurement was also described in Chap. 2. The lateral intensity variation of the laser light was measured through a large quartz window on the dewar by a small area InGaAs detector mounted on a stepper driven x-y-z stage. To estimate the effect of quartz window on the measurement, the room temperature far field patterns were measured with and without the window at several driving currents; and the results are shown in Fig.6.2.1. The quartz window has negligible effect on the measured far field. To avoid any possible disturbance from the detector, the detector was set an angle to the laser facet. The measurements were carried out in pulse mode so that the effect of heating on the far field pattern was minimized.

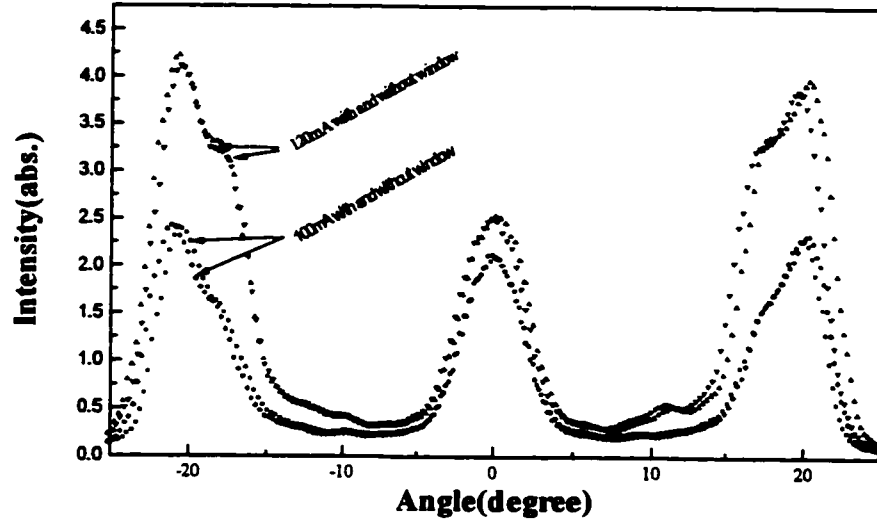


Fig.6.2.1 The far-field measured at 280K with and without the quartz window at several driving currents for 1.3 μm tensile strained three-well 32 μm wide ridge waveguide laser. The window is seen to have negligible effect on the measured far fields

6.3 Theoretical Slab Waveguide Analysis

The experimentally observed far field distributions are related to the internal modes of the laser cavity, and are the Fourier transformation of the two-dimensional internal cavity electrical field distribution. Ideally, the laser cavity modes can be calculated by solving coupled electrical wave propagation equations, carrier transportation equations, and laser transition equations [Wilt, 1981] [Lundstrom, 1983] [Li, 1995]. The passive slab waveguide theory only provides one dimensional solutions, but it can give insight into the laser cavity modes, especially for strongly refractive index guided laser structures for which the injected carriers have little effect

on the refractive index. The laser cavity modes can be simply calculated by solving the one-dimensional wave equation.

6.3.1 Theoretical Description of Laser Cavity Modes

The source-free, time-dependent Maxwell equations (in MKSA unit) are:

$$\nabla \cdot \mathbf{D} = 0, \quad \nabla \cdot \mathbf{B} = 0, \quad \nabla \times \mathbf{E} = -\frac{\partial \mathbf{B}}{\partial t}, \quad \nabla \times \mathbf{H} = \frac{\partial \mathbf{D}}{\partial t} \quad (6.3.1)$$

and the material constitutive equations for a dielectric waveguide are:

$$\mathbf{D} = \epsilon \mathbf{E}, \quad \mathbf{B} = \mu_0 \mathbf{H}; \quad (6.3.2)$$

where the dielectric constant ϵ is:

$$\epsilon = \epsilon_0 n^2(x, y) \quad (6.3.3)$$

Assuming \mathbf{E} and \mathbf{H} to be periodically time dependent according to $\mathbf{E} \exp(i\omega t)$ and $\mathbf{H} \exp(i\omega t)$, two wave equations for electrical and magnetic field can be obtained:

$$\begin{aligned} \nabla^2 \mathbf{E} + \mu_0 \epsilon \omega^2 \mathbf{E} + \nabla(\mathbf{E} \cdot \nabla \ln \epsilon) &= 0 \\ \nabla^2 \mathbf{H} + \mu_0 \epsilon \omega^2 \mathbf{H} + (\nabla \ln \epsilon) \times (\nabla \times \mathbf{H}) &= 0 \end{aligned} \quad (6.3.4)$$

Equation (6.3.4) are subject to boundary conditions at surfaces where abrupt changes of the material constants occur. With the unit vector \mathbf{e}_n chosen perpendicular to the

surface and in the absence of surface charges and surface currents, the boundary conditions are:

$$\mathbf{e}_n \cdot (\mathbf{B}_1 - \mathbf{B}_2) = 0, \mathbf{e}_n \cdot (\mathbf{D}_1 - \mathbf{D}_2) = 0, \mathbf{e}_n \times (\mathbf{E}_1 - \mathbf{E}_2) = 0, \mathbf{e}_n \times (\mathbf{H}_1 - \mathbf{H}_2) = 0 \quad (6.3.5)$$

The transverse index gradients described by $\nabla \ln \epsilon$ tend to couple the components of the vector fields \mathbf{E} and \mathbf{H} . But the longitudinal field components are decoupled from the transverse components. By separating the field into transverse ($\mathbf{E}_t, \mathbf{H}_t$) and longitudinal ($\mathbf{E}_z, \mathbf{H}_z$) components, the modal fields may be written in the form:

$$\mathbf{E} = (\mathbf{E}_t + \mathbf{E}_z)e^{-i\beta z}, \quad \mathbf{H} = (\mathbf{H}_t + \mathbf{H}_z)e^{-i\beta z} \quad (6.3.6)$$

By substituting (6.3.6) into (6.3.4), the two wave equations separated into their transverse and longitudinal components can be written as:

$$\begin{aligned} \nabla_t^2 \mathbf{E}_t + \nabla_t (\mathbf{E}_t \cdot \nabla_t \ln \epsilon) + (\omega^2 \epsilon \mu_0 - \beta^2) \mathbf{E}_t &= 0 \\ \nabla_t^2 \mathbf{H}_t + (\nabla \ln \epsilon) \times (\nabla \times \mathbf{H}_t) + (\omega^2 \epsilon \mu_0 - \beta^2) \mathbf{H}_t &= 0 \\ i\beta \mathbf{E}_z &= \nabla \cdot \mathbf{E}_t + \mathbf{E}_t \ln \epsilon \\ i\beta \mathbf{H}_z &= \nabla \cdot \mathbf{H}_t \end{aligned} \quad (6.3.7)$$

Consider a planar slab waveguide, where a film of thickness $2h$ and uniform refractive index n_f is sandwiched between a substrate of uniform index n_s and a cover layer of uniform index n_c , as shown in Fig.6.3.1.

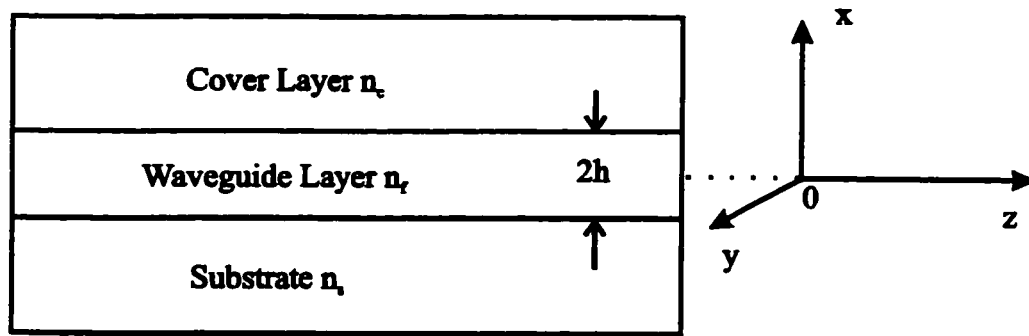


Fig.6.3.1 The slab waveguide structure, in which a $2h$ thick uniform thin film sandwiched by two uniform infinite thick dielectric materials

In each of the uniform regions the wave equation can be reduced to

$$\frac{d^2 E}{dx^2} + (\omega^2 \epsilon \mu_0 - \beta^2) E = 0 \quad (6.3.8)$$

In accordance with the wave equations, various transverse decay constants and propagation constant are defined by

$$\kappa_c^2 = n_c^2 k^2 - \beta^2 = -\gamma_c^2, \quad \kappa_f^2 = n_f^2 k^2 - \beta^2, \quad \kappa_s^2 = n_s^2 k^2 - \beta^2 = -\gamma_s^2 \quad (6.3.9)$$

For TE modes, whose electrical field lie in the y direction,

$$H_y = E_x = E_z = 0, \quad H_x = -\left(\frac{\beta}{\omega\mu_0}\right)E_y, \quad H_z = \left(\frac{i}{\omega\mu_0}\right)\frac{\partial E_y}{\partial x} \quad (6.3.10)$$

with the E_y component obeys (6.3.8).

The boundary conditions demand that E_y (and thereby H_x) and $\partial E_y / \partial x$ (and thereby H_z) be continuous across the film boundaries at $x=\pm h$. For guided modes, the solutions to (6.3.8) are

$$\begin{aligned} E_y &= E_s \exp(\gamma_s(x+h)), & x < -h \\ E_y &= E_c \exp(-\gamma_c(x-h)) & x > h \\ E_y &= E_f \cos(\kappa_f x - \phi), & -h < x < h \end{aligned} \quad (6.3.11)$$

Applying the boundary conditions and using the definitions, (6.3.9) gives

$$\begin{aligned} m\pi + \kappa_f h - \phi &= \tan^{-1}\left(\frac{\gamma_s}{\kappa_f}\right) & m \text{ is a integer} \\ n\pi + \kappa_f h + \phi &= \tan^{-1}\left(\frac{\gamma_c}{\kappa_f}\right) & n \text{ is a integer} \end{aligned} \quad (6.3.12)$$

with the dispersion relation

$$(m+n)\pi + 2\kappa_f h = \tan^{-1}\left(\frac{\gamma_c}{\kappa_f}\right) + \tan^{-1}\left(\frac{\gamma_s}{\kappa_f}\right) \quad (6.3.13)$$

and the phase angle

$$\phi = \frac{1}{2}\left((m-n)\pi + \tan^{-1}\left(\frac{\gamma_c}{\kappa_f}\right) - \tan^{-1}\left(\frac{\gamma_s}{\kappa_f}\right)\right) \quad (6.3.14)$$

The relation between the peak fields E_s , E_f , and E_c are

$$E_c = E_f \cos(\kappa_f h + \phi), \quad E_s = E_f \cos(\kappa_f h - \phi) \quad (6.3.15)$$

The power P carried by a mode per unit guide width is calculated as follows:

$$P = -2 \int_{-\infty}^{\infty} E_y H_x dx = N \sqrt{\frac{\epsilon_0}{\mu_0}} E_f^2 \cdot h_{\text{eff}} \quad (6.3.16)$$

where

$$h_{\text{eff}} = 2h + \frac{1}{\gamma_s} + \frac{1}{\gamma_c} \quad (6.3.17)$$

is the effective thickness of the waveguide.

6.3.2 Theoretical Description of Far-field of a Laser

The far-field distribution of a diode laser can be determined by treating it as a diffraction problem [Zeng, 1993]. For this purpose, a three-dimensional monochromatic scalar wave expressed by $\Psi(\mathbf{r}, t) = u(\mathbf{r}) \exp(-i\omega t)$ is considered. In a vacuum the space-dependent part $u(\mathbf{r})$ satisfies the Helmholtz equation, i.e.,

$$\nabla^2 u(\mathbf{r}) + k^2 u(\mathbf{r}) = 0 \quad (6.3.18)$$

where $k = 2\pi/\lambda$ is the propagation constant.

A solution of the above equation can be expressed in terms of its boundary values [Nie-Vesperinas, 1991]

$$u(\mathbf{r}) = -\frac{1}{2p} \int_s u(\mathbf{r}') \frac{\partial G(\mathbf{r}, \mathbf{r}')}{\partial \mathbf{n}} ds \quad (6.3.19)$$

where

$$G(\mathbf{r}, \mathbf{r}') = \exp(ik|\mathbf{r} - \mathbf{r}'|) / |\mathbf{r} - \mathbf{r}'| \quad (6.3.20)$$

The symbol s denotes the boundary surface (i.e., the diffracting screen), \mathbf{r}' takes on the values of \mathbf{r} on the boundary surface, and \mathbf{n} is the local outward normal to this surface. Equation (6.3.19) is the first Rayleigh-Sommerfeld integral formula, and corresponds to Dirichlet boundary conditions.

A Cartesian coordinate system (x, y, z) relative to a diode laser is defined in Fig.6.3.2. The boundary surface is defined by the x - y plane, (i.e., $z=0$) and coincides with the front laser mirror, which radiates in the half-space $z>0$, so that

$$\frac{\partial G(\mathbf{r}, \mathbf{r}')}{\partial \mathbf{n}} = \frac{\partial G(\mathbf{r}, \mathbf{r}')}{\partial z} \quad (6.3.21)$$

Substituting (6.3.20) and the definition of the boundary surface into (6.3.19) yields

$$u(\mathbf{r}) = -\frac{1}{2\pi} \int_{-\infty}^{\infty} \int_{-\infty}^{\infty} u(\mathbf{r}') \frac{z}{|\mathbf{r} - \mathbf{r}'|^3} \times (ik|\mathbf{r} - \mathbf{r}'| - 1) \exp(ik|\mathbf{r} - \mathbf{r}'|) dx' dy' \quad (6.3.22)$$

where $\mathbf{r} = xi + yj + zk$ and $\mathbf{r}' = x'i + y'j$, the latter being the argument for the source field distribution at the end face of the diode laser.

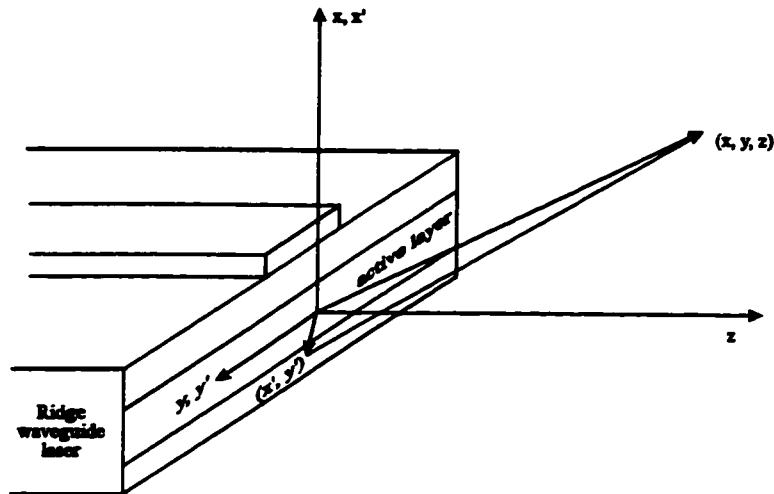


Fig.6.3.2 The relation of the far field and the internal cavity mode electrical field distribution

Because the source is limited to a very small region, when considering the far-field distribution, the following approximation can be made:

$$k|r - r'| \gg 1 \quad \text{and} \quad \frac{1}{|r - r'|} \approx \frac{1}{|r|} \quad (6.3.23)$$

In the phase of the integrand, a Taylor series expansion allows the introduction of the following simplification:

$$|r - r'| \approx |r| + (\nabla|r|) \cdot r' = |r| + \frac{1}{|r|} r \cdot r' \quad (6.3.24)$$

The above relations invoke the approximation that the distance from the source to the observation point is much larger than the wavelength as well as the size of the source. These approximations are reasonable for diode lasers, as the beam shaping is usually attempted at distances significantly larger than the wavelength.

Substituting (6.3.23) and (6.3.24). into (6.3.22), yields

$$u(x, y, z) = -\frac{iz}{\lambda r} \frac{e^{ikr}}{r} \int_{-\infty}^{\infty} \int_{-\infty}^{\infty} u(x', y') \times \exp\left(-\frac{ik(xx' + yy')}{r}\right) dx' dy' \quad (6.3.25)$$

where $r = (x^2 + y^2 + z^2)^{1/2}$.

For one-dimension far-field observation(e.g., along the diode laser junction plane), $x=0$ and $u(x', y')$ can be written as the product of two functions, each dependent on only one of the two transverse coordinates(x' or y'). Then, (6.3.22) became

$$u(0, y, z) = -\frac{iz}{\lambda r} \frac{e^{ikr}}{r} \int_{-\infty}^{\infty} u(x') dx' \int_{-\infty}^{\infty} u(y') \exp\left(-\frac{iky y'}{r}\right) dy' \quad (6.3.26)$$

To calculate the $u(x')$ and $u(y')$, the effective index method can be used [Tamir, 1991]. The laser cavity can be treated as two symmetrical slab waveguides, one in x -direction and another in y -direction. Assuming $u(y')$ to have the planar TE waveguide mode (for TM mode, the similiar result can be achieved), then the far field is

$$u(0, y, z) = -\frac{iz}{\lambda r} \frac{e^{ikr}}{r} \int_{-\infty}^{\infty} u(x') dx' \times \left[\frac{E_c e^{\gamma_c h}}{\gamma_c - \frac{iky}{r}} e^{-(\gamma_c - \frac{iky}{r})h} + E_f \left(\frac{e^{-i\phi}}{\kappa_f - \frac{k}{r}y} \sin\left((\kappa_f - \frac{k}{r}y)h\right) + \frac{e^{i\phi}}{\kappa_f + \frac{k}{r}y} \sin\left((\kappa_f + \frac{k}{r}y)h\right) + \frac{E_s e^{\gamma_s h}}{\gamma_s + \frac{iky}{r}} e^{-(\gamma_s + \frac{iky}{r})h} \right) \right] \quad (6.3.27)$$

where $r = (y^2 + z^2)^{1/2}$. Assuming $u(x')$ to be in fundamental mode, then the integration of $u(x')$ is a constant.

The cavity mode of a laser as a periodic function of time is written as

$$u(x, y, t) = u(x, y)\exp(i\omega t) \quad (6.3.28)$$

then, the far-field of two cavity mode superposition is:

$$u(0, y, z, t) = -\frac{iz}{\lambda_i r} \frac{\exp(ik_i r)}{r} \int_{-\infty}^{\infty} u_i(x') dx' \int_{-\infty}^{\infty} u_i(y') \exp(-ik_i yy') dy' \exp(i\omega_i t) \\ - \frac{iz}{\lambda_j r} \frac{\exp(ik_j r)}{r} \int_{-\infty}^{\infty} u_j(x') dx' \int_{-\infty}^{\infty} u_j(y') \exp(-ik_j yy') dy' \exp(i\omega_j t) \quad (6.3.29)$$

Because the experimentally observed far-field is the intensity distribution instead of E-field distribution, the observed intensity distribution, then, is

$$|u(0, y, z, t)|^2 = \left| \frac{z}{\lambda_i r} \frac{1}{r} \int_{-\infty}^{\infty} u_i(x') dx' \int_{-\infty}^{\infty} u_i(y') \exp\left(-\frac{ik_i yy'}{r}\right) dy' \right|^2 \\ + \left| \frac{z}{\lambda_j r} \frac{1}{r} \int_{-\infty}^{\infty} u_j(x') dx' \int_{-\infty}^{\infty} u_j(y') \exp\left(-\frac{ik_j yy'}{r}\right) dy' \right|^2 \quad (6.3.30)$$

plus a cross term:

$$\begin{aligned}
& -\frac{iz}{\lambda_i r} \frac{\exp(ik_i r)}{r} \int_{-\infty}^{\infty} u_i(x') dx' \int_{-\infty}^{\infty} u_i(y') \exp\left(-\frac{ik_i yy'}{r}\right) dy' \exp(i(\omega_i - \omega_j)t) \\
& \times \left(\frac{iz}{\lambda_j r} \frac{\exp(ik_j r)}{r} \int_{-\infty}^{\infty} u_j(x') dx' \int_{-\infty}^{\infty} u_j(y') \exp\left(-\frac{ik_j yy'}{r}\right) dy' \right)^* + \text{c. c.}
\end{aligned} \tag{6.3.31}$$

The cross term includes a term $\exp(i(\omega_i - \omega_j)t)$. Since each mode of laser cavity has its unique frequency, and usually, the measurement time of the far-field is much longer compared to $2\pi/(\omega_i - \omega_j)$, the cross term (6.3.31) does not contribute to the observed far-field. Hence, the observed far field is expected to be the summation of individual far fields of cavity modes.

6.4 Theoretical Calculation of Internal Cavity Modes and Far-field Patterns

The laser structure investigated in this chapter allows only a single cavity mode in the x-direction(perpendicular to the junction plane, here called vertical mode). However, in the lateral direction, the cavity modes are determined by the width of ridge. The laser cavity can be treated laterally as a symmetrical slab waveguide, whose refractive index can be calculated by using the effective index method. The refractive indices of layers in the laser structure are listed in Table.6.4.1. The dependence of refractive index on composition was taken from Adachi [Adachi, 1989(I), 1989(II), 1988]. The effect of doping concentration and carrier injection on the refractive indices was ignored in the calculation. Numerical calculation [Jessop, 1995] indicates that the laser supports only a single vertical mode both inside and outside of the ridge, and illustrated in Fig. 6.4.1 .

Table 6.4.1. The refractive index of different layer materials

Material	In ₅₃ Ga ₄₇ As	InP	In ₅₇ Ga ₄₃ As ₉₀ P ₁₀	In ₈₉ Ga ₁₁ As ₇₇ P ₈₇	In ₄₉ Ga ₅₁ As ₇₇ P ₂₈
Index n	3.3478	3.2021	3.3749	3.3173	3.6190

The number of guided lateral modes for different ridge widths determined by numerical calculation [Jessop, 1995] is listed in Table. 6.4.2

Table 6.4.1 The number of guided modes for different ridge width lasers

ridge width	2 μ m	4 μ m	8 μ m	16 μ m	32 μ m
No. of modes	1	2	4	7	13

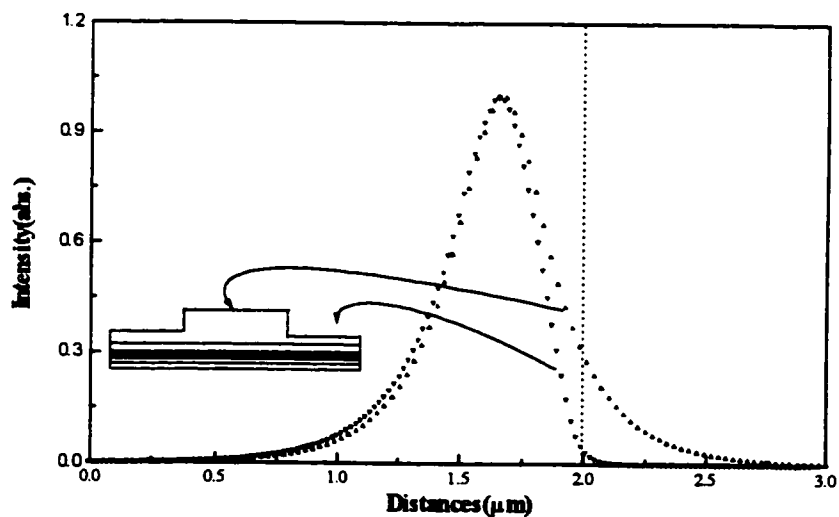
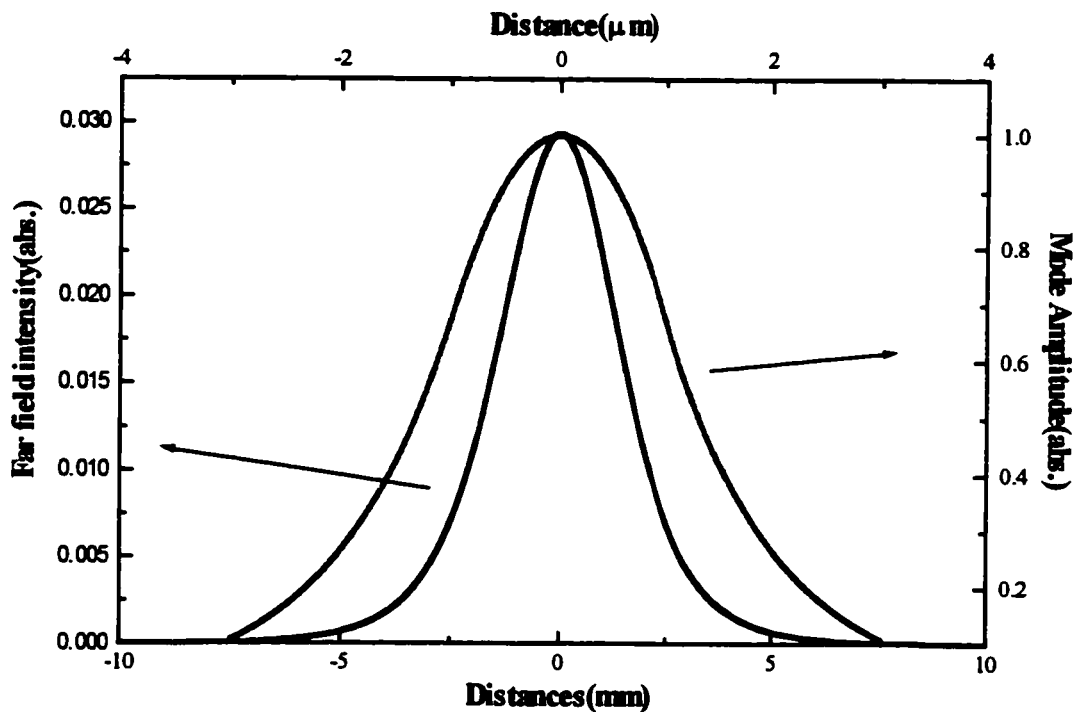
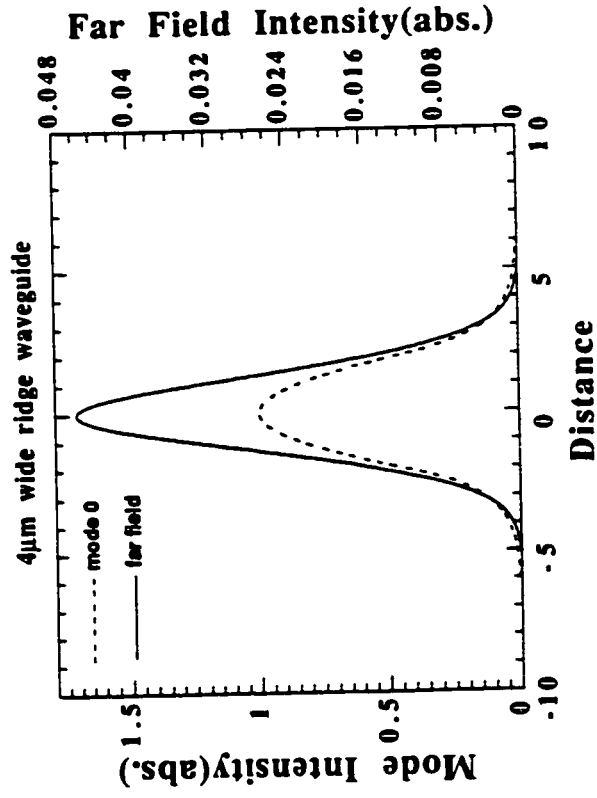
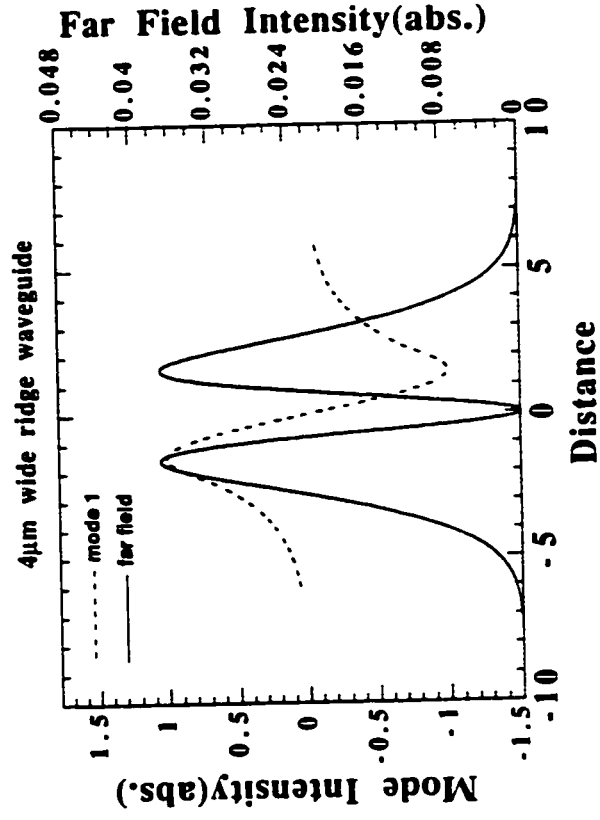


Fig.6.4.1 The vertical mode intensity distribution at ridge and outside ridge

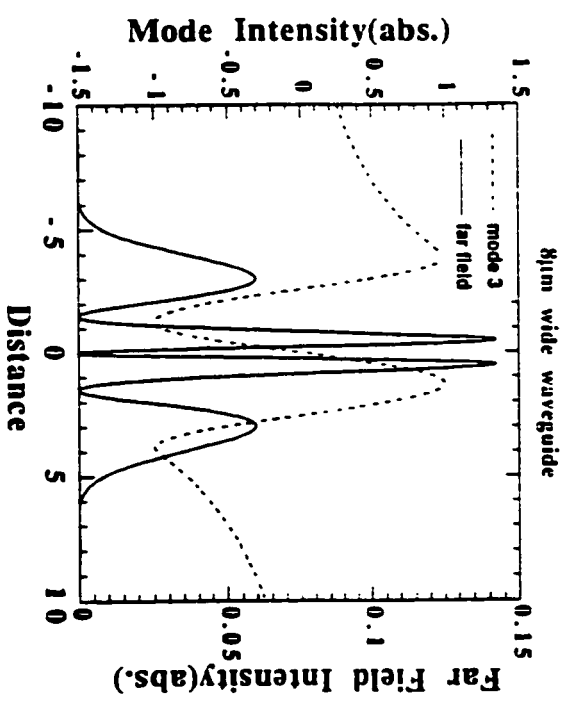
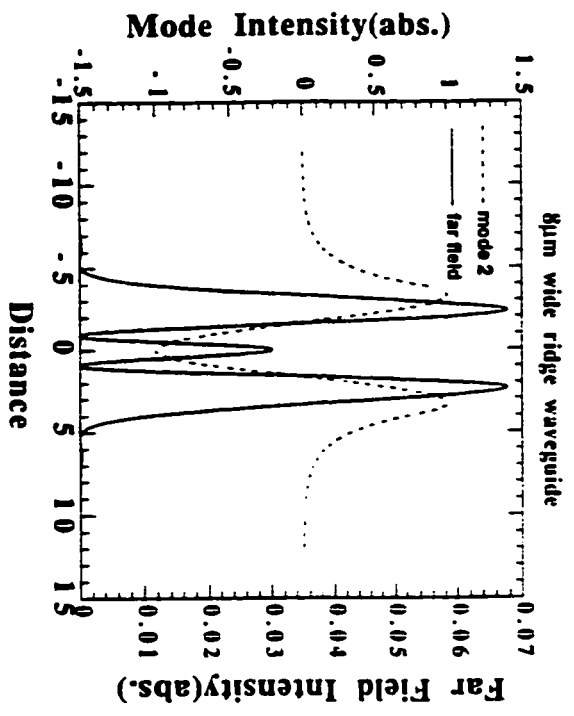
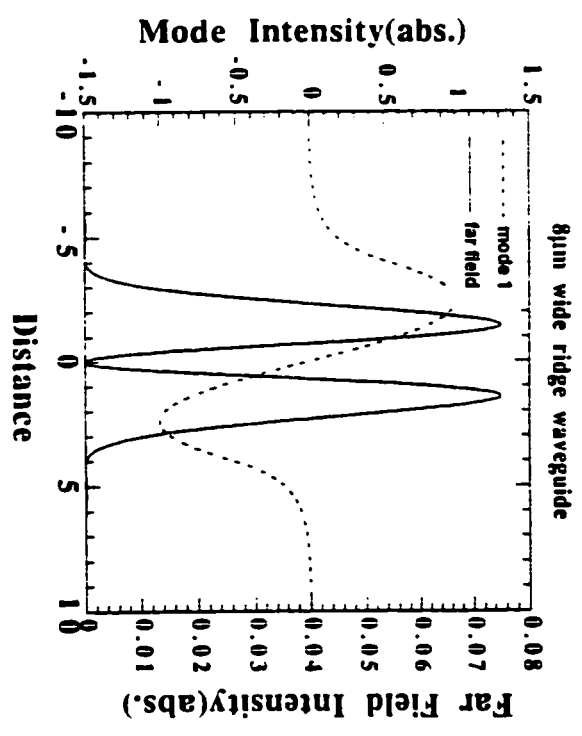
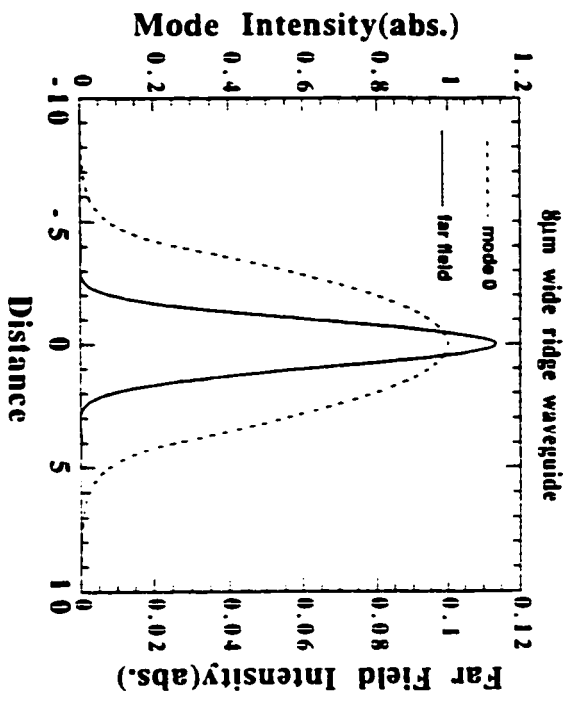
Figure 6.4.2(a), (b), (c), (d) and (e) show the calculated far fields using (6.3.27) with the corresponding internal cavity mode calculated using (6.3.11) for $2\mu\text{m}$, $4\mu\text{m}$, $8\mu\text{m}$, $16\mu\text{m}$ and $32\mu\text{m}$ wide ridge waveguide tensile SL-MQW lasers, respectively. Except for the fundamental mode, the far-field of the higher internal cavity modes show two major lobes with some peaks between the two bigger lobes, the total number of peaks corresponding to the order of mode. It is seen that the narrower the ridge width, the narrower the peaks.



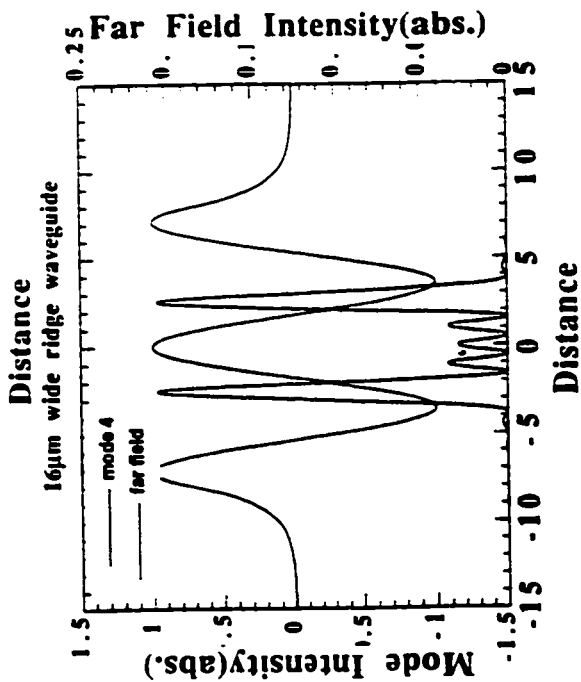
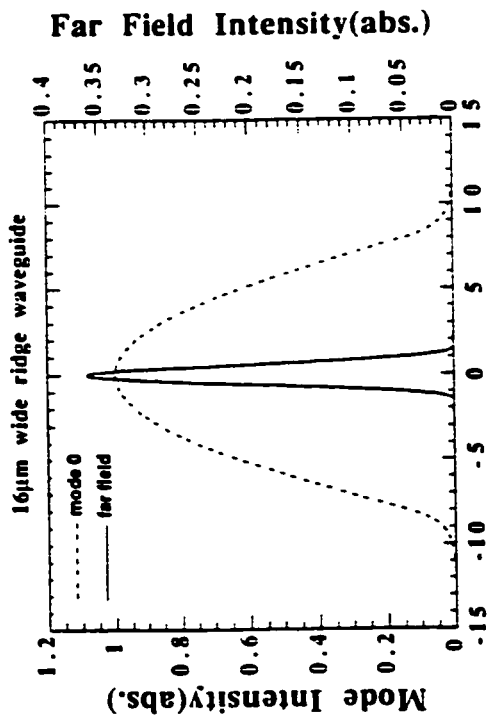
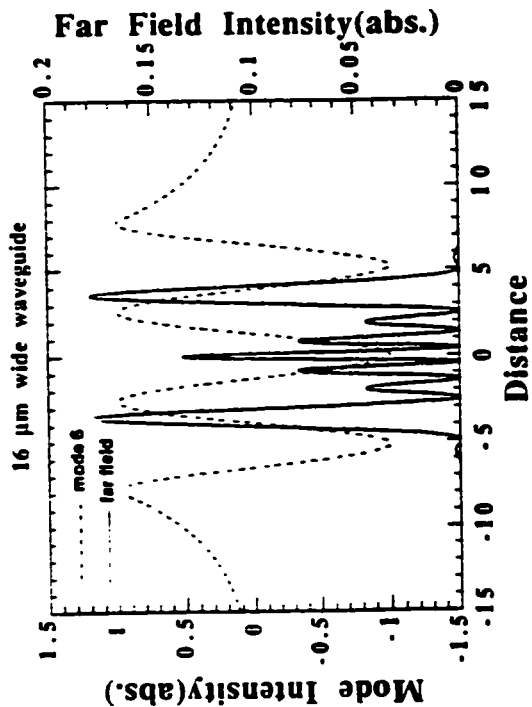
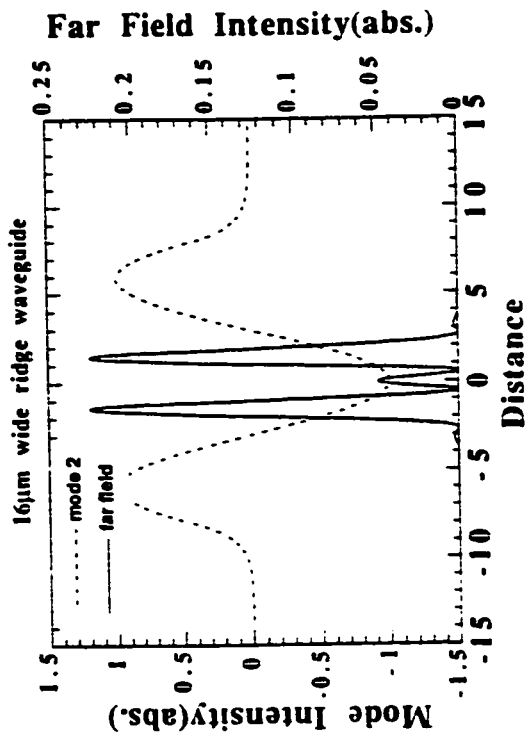
(a)



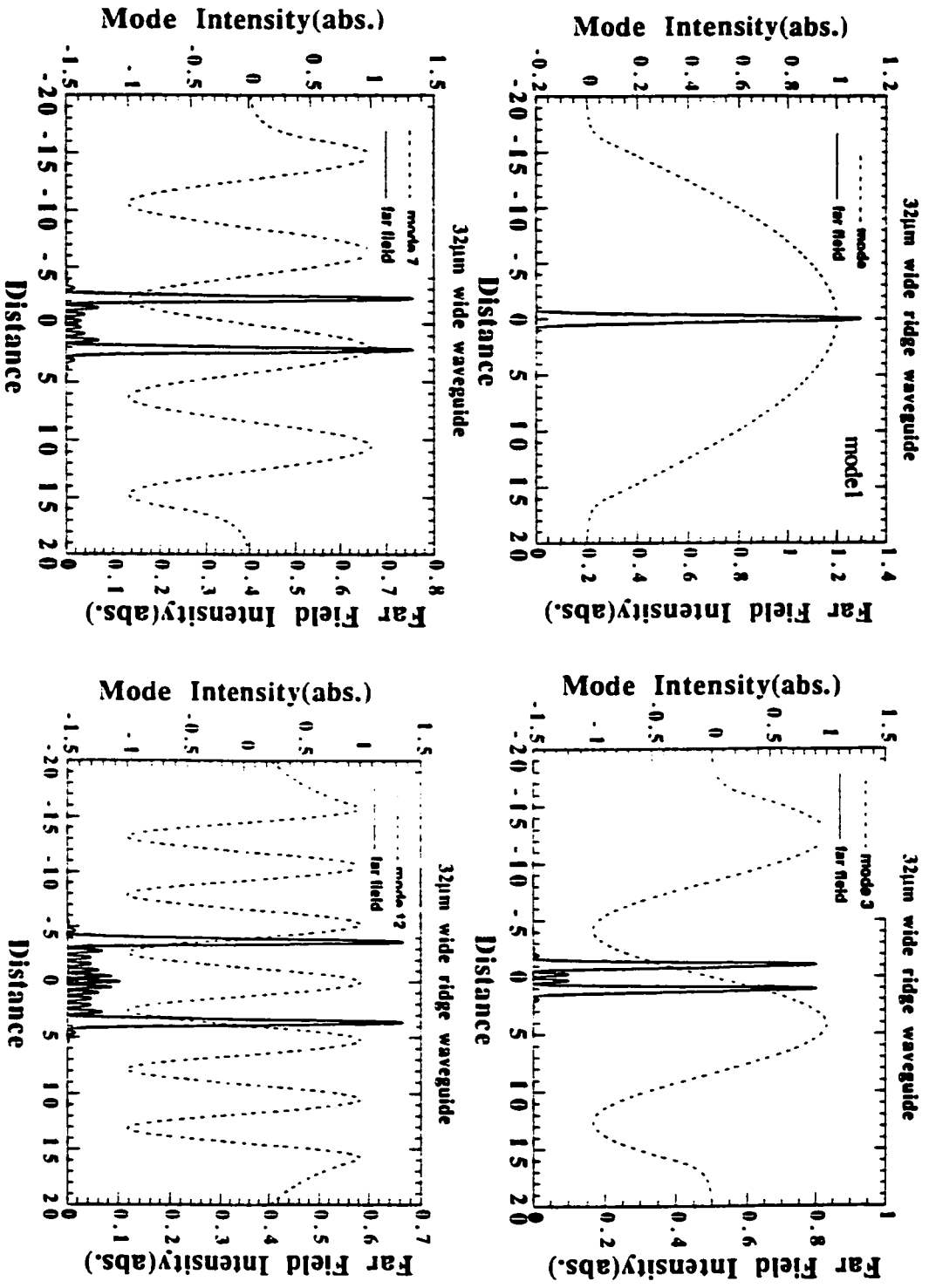
(b)



(c)



(d)



(e) Fig.6.4.1 The calculated internal cavity modes and their corresponding far field patterns for 2µm(a), 4µm(b), 8µm(c), 16µm(d) and 32µm(e) wide ridge waveguide lasers: the horizontal axis scale is 1µm for internal cavity modes and mm for far field(assuming an observation distance 14 m.)

6.5 Experimental Results and Discussion

The far-field and spectral measurements were carried out by the set-up illustrated in Chap. 2 at a series of different temperatures. The measured far-field patterns were compared with the calculated patterns.

6.5.1 Far-field Observation

As expected, the wide ridge waveguide lasers were observed to have far field distributions that had multiple lobes in the lateral direction. Figure 6.5.1 is the measured two-dimensional far field for 16 μm -wide ridge waveguide laser operating at 110K.

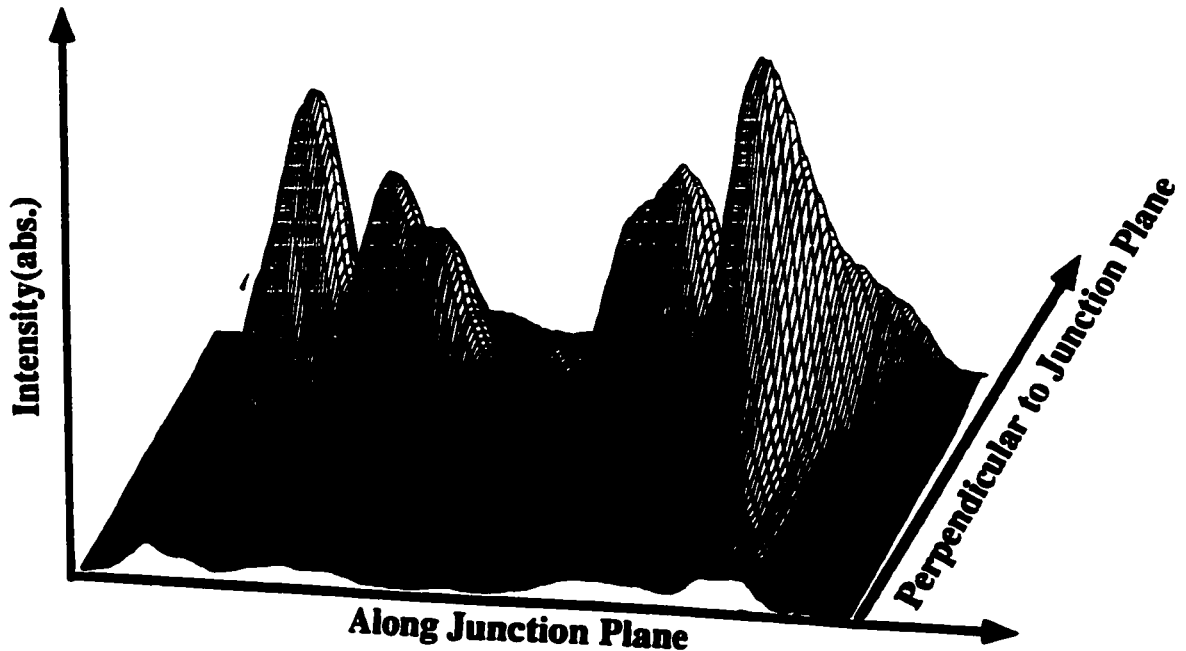


Fig.6.5.1 The measured two-dimensional far-field pattern for 16 μm wide ridge waveguide, 1.3 μm tensile strained multiple quantum well laser operating at 110K. The pattern shows multiple peaks and mirror symmetry in the lateral direction.

The far field, which is in the fundamental vertical mode, shows multiple peaks and mirror symmetry in the lateral direction when operating at 110K with an output power 3mW. After raising the temperature of the laser to 300K, the measured two-dimension far field pattern manifests a single narrow peak, as shown in Fig. 6.5.2.

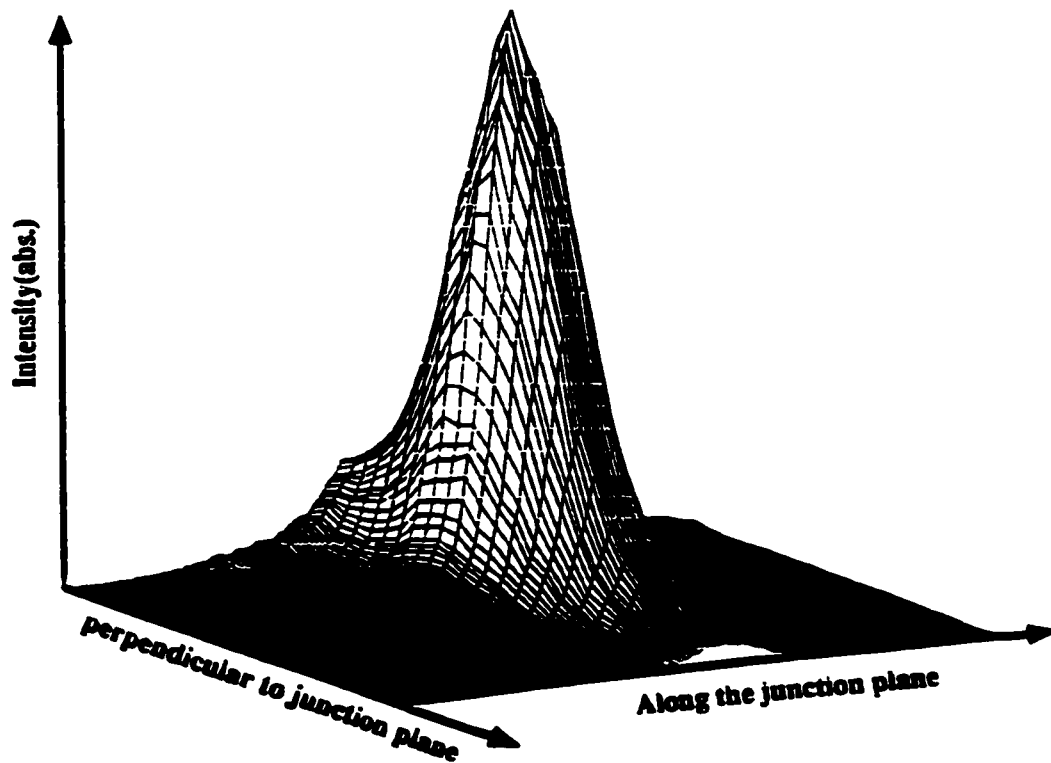


Fig.6.5.2 The measured two-dimensional far field pattern for 16 μ m wide ridge waveguide 1.3 μ m tensile strained multiple quantum well laser at 300K. The pattern shows a single narrow peak.

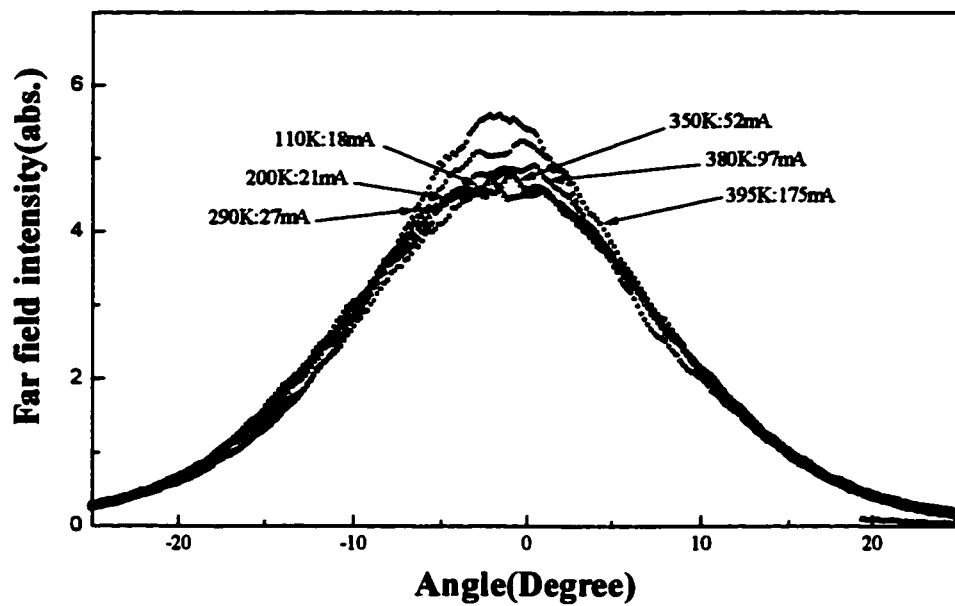
The experimental observation indicates that at low temperatures the laser tends to oscillate in higher cavity modes, while at high temperature the laser tends to oscillate in lower cavity modes. Since the far field patterns were observed in pulse mode, and the duration and the duty cycle of the pulse were 100ns and 0.01% respectively, the effect on the far field of heating could be ignored [Hunziker, 1995].

Every cavity mode has its unique threshold gain, and its modal gain can be determined by [Agrawal, 1984]

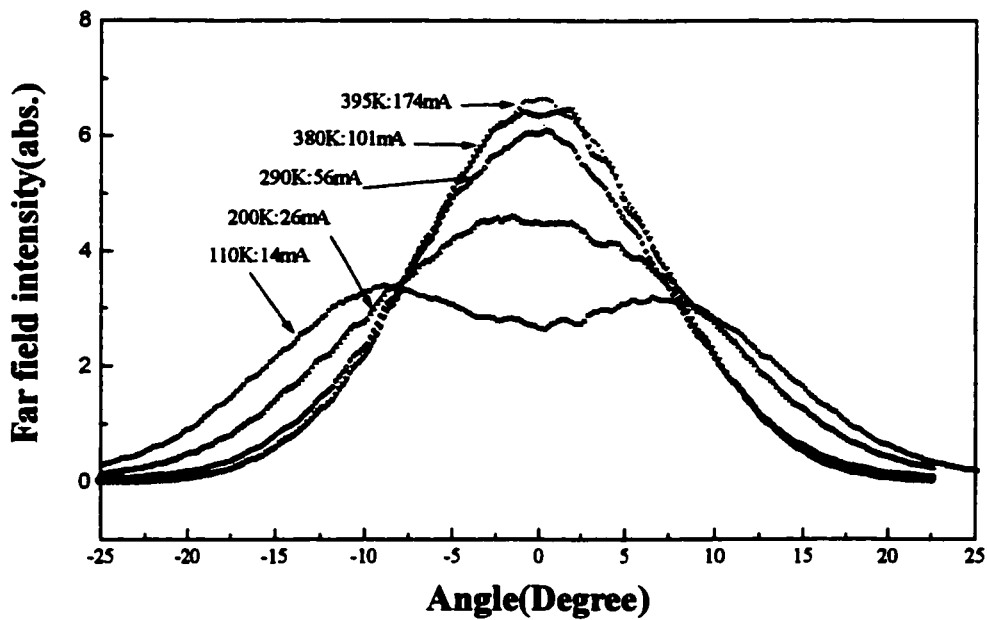
$$G_i = \frac{\iint_s [\beta(n(x, y) - n_0) - \gamma n(x, y) - \alpha_i(T) - \alpha_{i0} - \alpha_{im}] |E_i(x, y)|^2 dx dy}{\iint_s |E_i(x, y)|^2 dx dy} \quad (6.5.1)$$

where G_i is the i th optical mode gain, β is the gain coefficient and n is the electron density at (x, y) . n_0 is the transparent carrier density, which is independent of the position. $\gamma n(x, y)$, as defined in previous chapters, is the carrier related loss, which is independent of mode. $\alpha_i(T)$ is a temperature-dependent loss, e.g., phonon scattering. α_{i0} is the residual loss due to crystal imperfections and surface scattering and α_{im} is the mirror loss. $\alpha_i(T)$, α_{i0} , and α_{im} are mode dependent. $E_i(x, y)$ is the electrical field. The modal gain g_i determines the threshold condition for i th mode. If $G_i > 0$, the i th mode could oscillate and its far field could be detected. Comparing Fig.6.5.1 with Fig.6.5.2, it can be speculated that the modal gain of fundamental mode at 110K is lower than that of higher order mode, and the opposite is true at 300K.

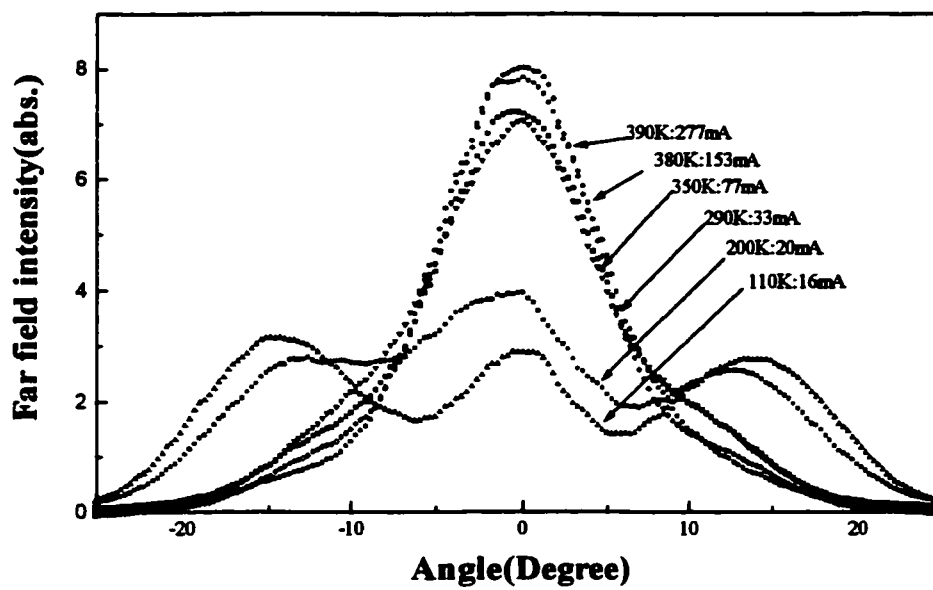
The experimentally observed far field patterns for varying ridge width are shown in Fig.6.5.3 for 1.3 μ m tensile strained multiple quantum well lasers with varying ridge width at different temperatures at an output power 3mW. For the 2 μ m wide ridge laser, the far field pattern stays almost the same at all temperatures. Thus it can be concluded that the effect of the injected carrier on the refractive index is negligible. For 4 μ m, 8 μ m and 16 μ m wide ridge waveguide lasers, the far field pattern narrows with increasing temperature. At 110K, the lasers oscillated in multiple modes, but at high temperature they oscillated in the fundamental mode.



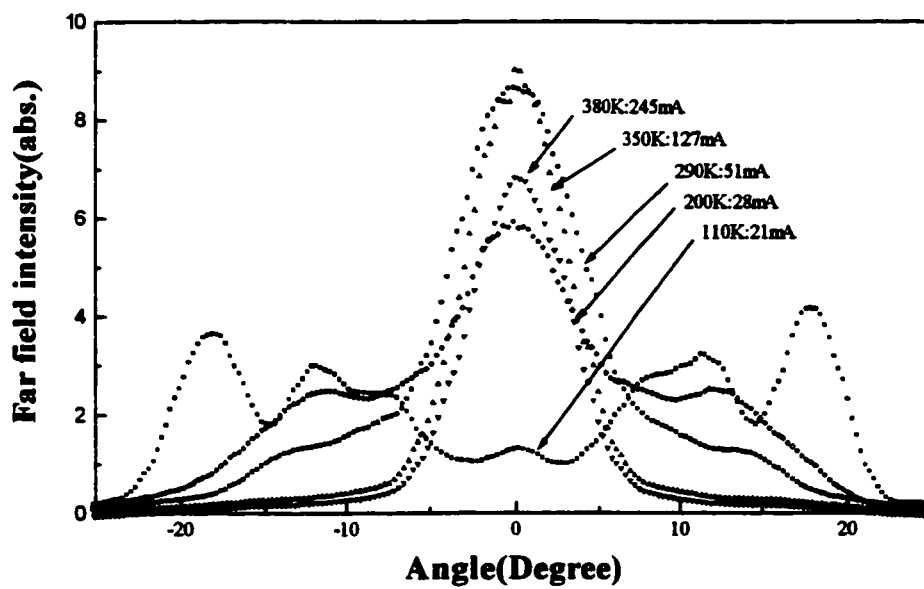
(a)



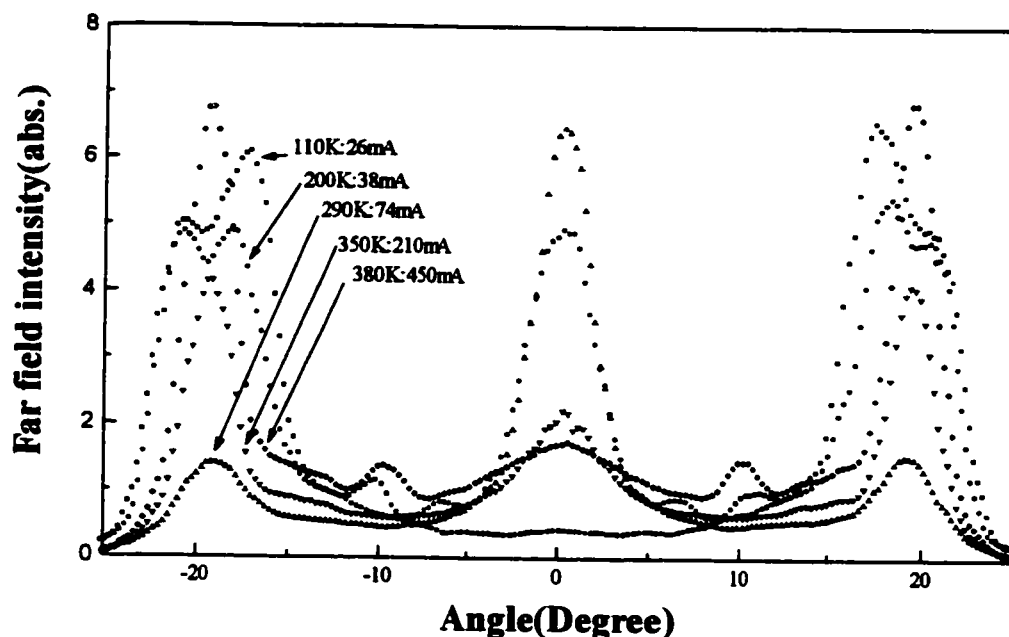
(b)



(c)



(d)



(e)

Fig.6.5.3. The experimentally observed far fields for $1.3\mu\text{m}$ tensile SL-MQW lasers with (a) $2\mu\text{m}$, (b) $4\mu\text{m}$, (c) $8\mu\text{m}$, (d) $16\mu\text{m}$, and (e) $32\mu\text{m}$ ridge width at different temperatures. The output power was at 3mW.

For $32\mu\text{m}$ wide ridge laser, at 110K, it oscillated completely in higher modes, but at high temperature (>290), it oscillated in both a higher mode and the fundamental mode. Figure 6.5.4 shows the far fields for $32\mu\text{m}$ wide ridge laser at 110K at different driving currents, and the inset shows L-I characteristics. The left or right side lobe of the far field pattern consists of a few peaks, and each peak corresponds to a different higher order mode. The far field pattern is virtually unchanged with increasing driving current. No kinks were observed on the L-I characteristics, which was reported to exist for stripe-geometry lasers in high-power operation [Lang, 1979] [Thompson, 1980].

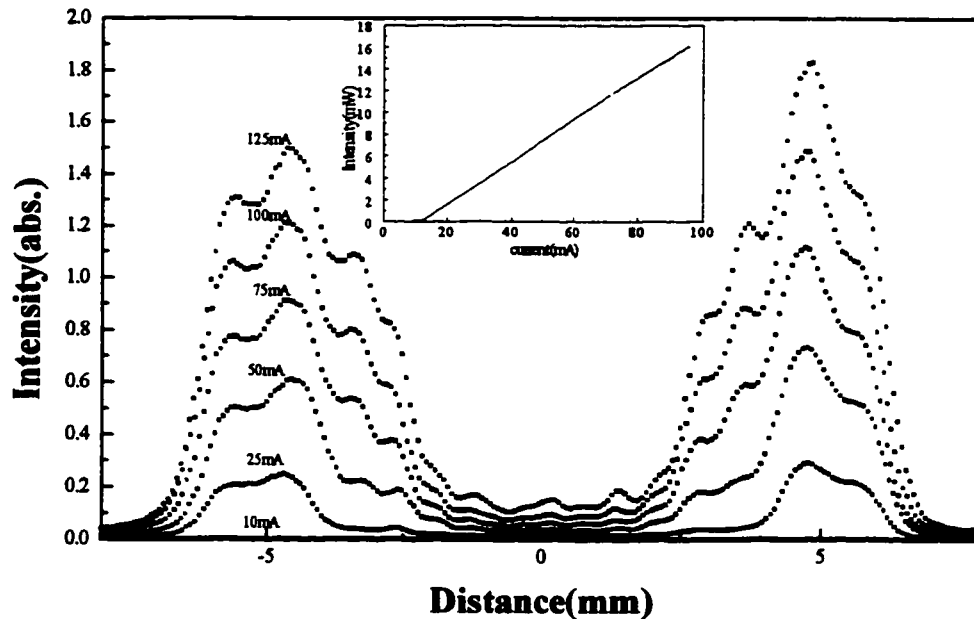


Fig. 6.5.4 The far field pattern for $32\mu\text{m}$ wide ridge waveguide tensile strained multiple quantum well laser at 110K at different driving currents. The inset is L-I characteristics at 110K

The measured and calculated full width at maximum height (FWHM) (the height normalized to one) for the far field of the fundamental mode for varying ridge width are shown in Fig. 6.5.5. The observation distance is 14.5mm. The theoretically calculated FWHMs agree very well with the experimentally measured ones for all different ridge width lasers.

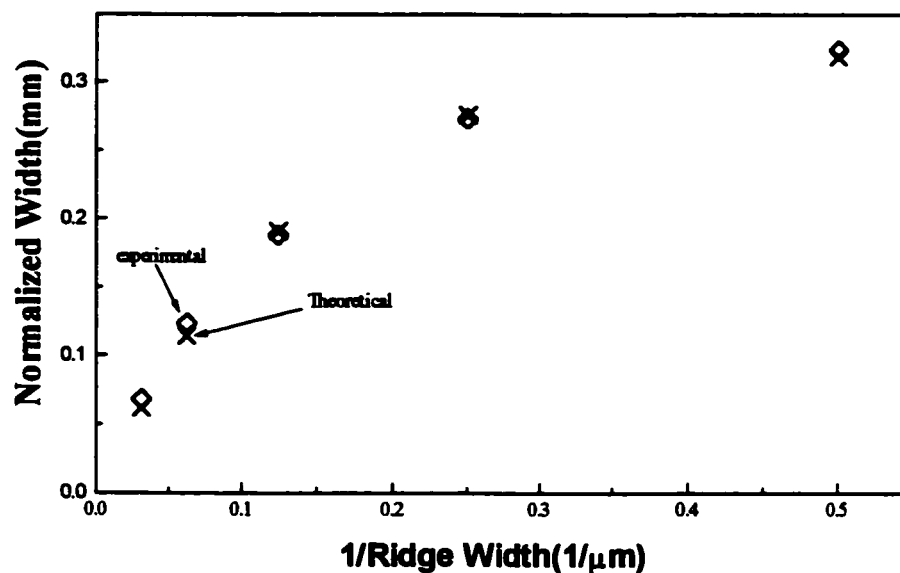
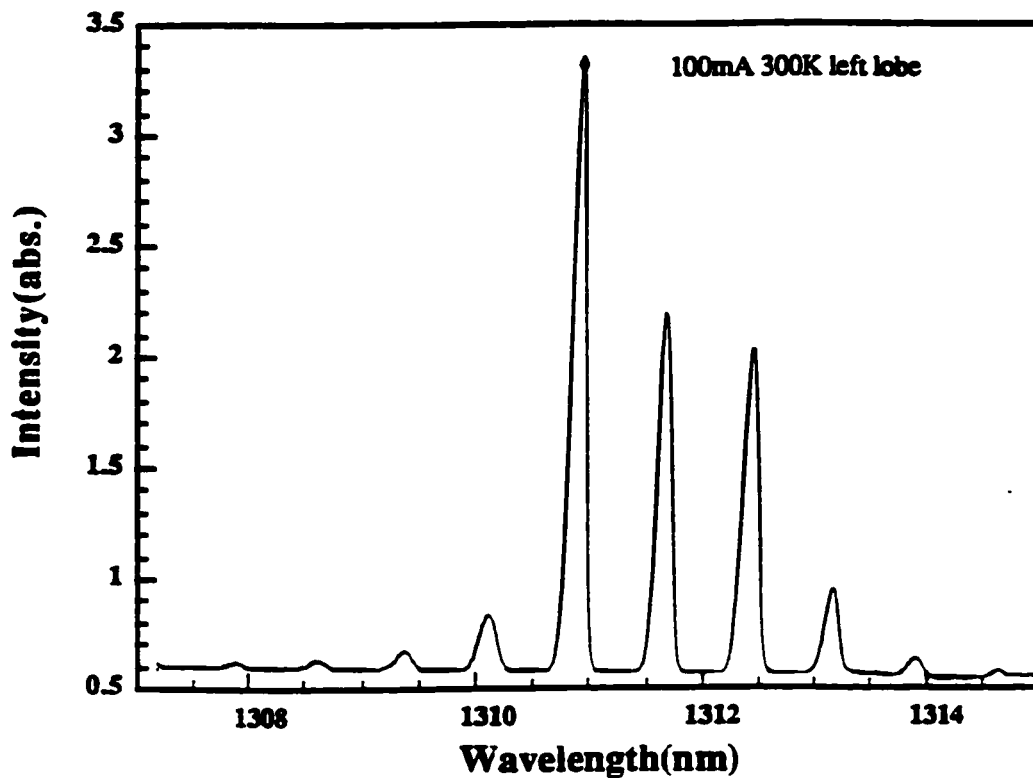


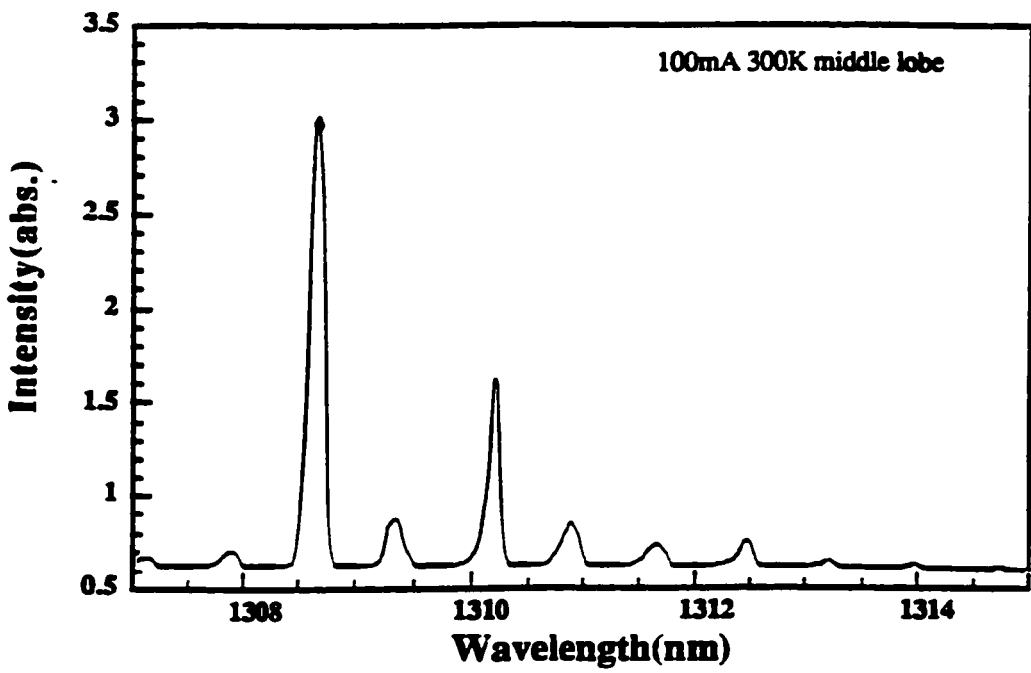
Fig.6.5.5 Calculated and experimentally measured Full width at half maximum vs. inverse ridge width

6.5.2 Spectral Measurement of the Lobes of the Far-field

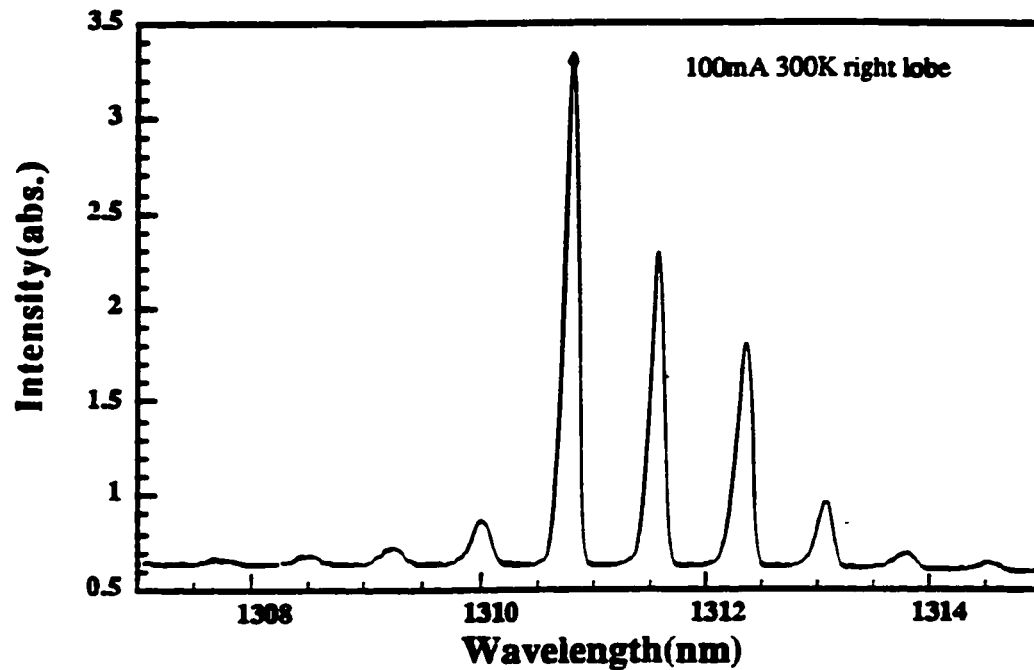
For 32μm wide laser, its room temperature far-field pattern shows three peaks, spectra of which are shown in Fig.6.5.6. The right and left lobes have same spectrum, which shows that they are from a same internal cavity mode, and the middle lobe has a different spectrum, which is from the fundamental internal cavity mode. It can be speculated that since the carrier distribution in the quantum well causes a band gap variation, and the different modes have different traveling paths in the active region, the different modes have different oscillating frequencies.



(a)



(b)



(c)

Fig.6.5.6 The optical spectra of (a)right lobe, (b)middle lobe, and (c)left lobe of the far field of a 32 μ m 1.3 μ m tensile SL-MQW laser at room temperature. The spectra of the right and left lobes are same, since they come from the same higher order internal cavity mode. The spectrum of the middle lobe is different from that of the right and left lobes. It comes from the fundamental mode

6.5.3 Theoretical Construction of the Far-field Pattern

As pointed out before, each far field pattern is the sum of the far field patterns of individual internal modes. Therefore the far field distribution, $F(y)$, can be written as

$$F(y) = \sum_{\text{all guided modes}} a_i F_i(y) \quad (6.5.1)$$

where $F_i(y)$ is the far field pattern of i th mode, and a_i is a weighting factor. Figure 6.5.7 shows the theoretically constructed far field patterns at different temperatures from the superposition of the far fields of individual internal modes of $16\mu\text{m}$ wide ridge waveguide laser. The construction was carried out by adjusting the parameters a_i until the far field pattern looks close to the experimental one. The component of higher mode decreases with increasing temperature. The theoretically constructed far field pattern is very similar to the measured one, as shown in Fig. 6.5.3(d).

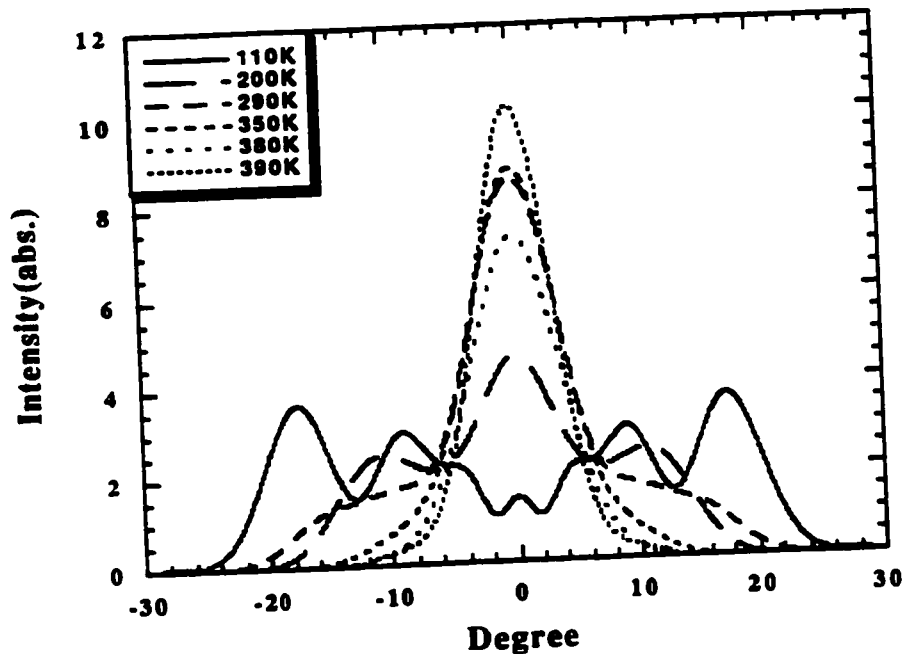


Fig.6.5.7 Constructed far field by proportionately combining the far fields of individual internal modes of $16\mu\text{m}$ wide ridge waveguide lasers. The component of higher mode decreases with increasing temperature.

6.6 Conclusions

In this chapter, the experimental observation and theoretical analysis using simple passive slab waveguide theory for far field patterns for $1.3\mu\text{m}$ 1.2% tensile strained layer multiple quantum well lasers with varying ridge widths were described. It was observed that the injected carriers have little effect on the effective refractive index. The $4\mu\text{m}$, $8\mu\text{m}$ and $16\mu\text{m}$ wide ridge waveguide lasers were shown to oscillate in a combination of the fundamental mode and higher order modes at 110K for 3mW output power, but with rising temperature, they tended to oscillate in the fundamental mode. The $32\mu\text{m}$ wide ridge waveguide laser oscillates exclusively in higher modes at 110K, and in a combination of the fundamental mode and higher order modes at high temperature. The observed multiple lobes are the result of higher mode oscillation rather than the fragmentation or antiguiding suggested in stripe lasers [Paxton, 1991][Beernink, 1991]. The change of the far field distribution with temperature may probably be attributed to spatial-hole burning [Garret, 1987]. However, it is extremely difficult to predict the oscillating modes at given output power and temperature because of the complicated interaction between the injected carriers and the optical field distribution, and the unknown individual modal loss. For example, the laser always oscillates in one or the combination of its eigenmodes; however, the precise prediction of the lasing modes needs the consideration of gain guiding and spatial hole burning [Nappi, 1994].

Chapter 7

THERMAL RUN-AWAY UNDER CW OPERATION AND THERMAL IMPEDANCE

7.1 Introduction

Heating is a particular concern in continuous wave operation because it affects the magnitude of the threshold current, the available output power, the wavelength of oscillating modes, as well as the operation reliability. Figure 7.1.1 shows a typical plot of output power vs. current for a laser under a continuous wave excitation. The L-I curve not only deviates from linear but rolls over to zero at a high temperature and driving current. This deviation is caused by the heating during CW operation .

The extent of heating-up is related to the steady-state thermal properties, which have generally been evaluated in terms of the thermal resistance of the laser. The thermal resistance is sensitive to laser structure and laser packaging. In addition to various experimental methods to measure the temperature rise [Manning, 1981], some theoretical computation has been used to calculate the temperature distribution around the active region of laser, and this indicated that the thermal properties are particularly sensitive to the ridge width of the laser [Duda, 1978] [Piprek, 1989].

The heat produced by the driving current applied to the laser results in a temperature rise, say ΔT , in the active region relative to the heat sink. The ratio of this temperature rise to the net input power is defined as the thermal impedance,

$R_{th} = \Delta T / (IV - P_0)$, where I , V , and P_0 are the CW driving current, voltage, and emitted optical power, respectively [Manning, 1981]. P_0 , which is usually several milliwatts or less, may generally be ignored since the input power IV is a few hundred milliwatts.

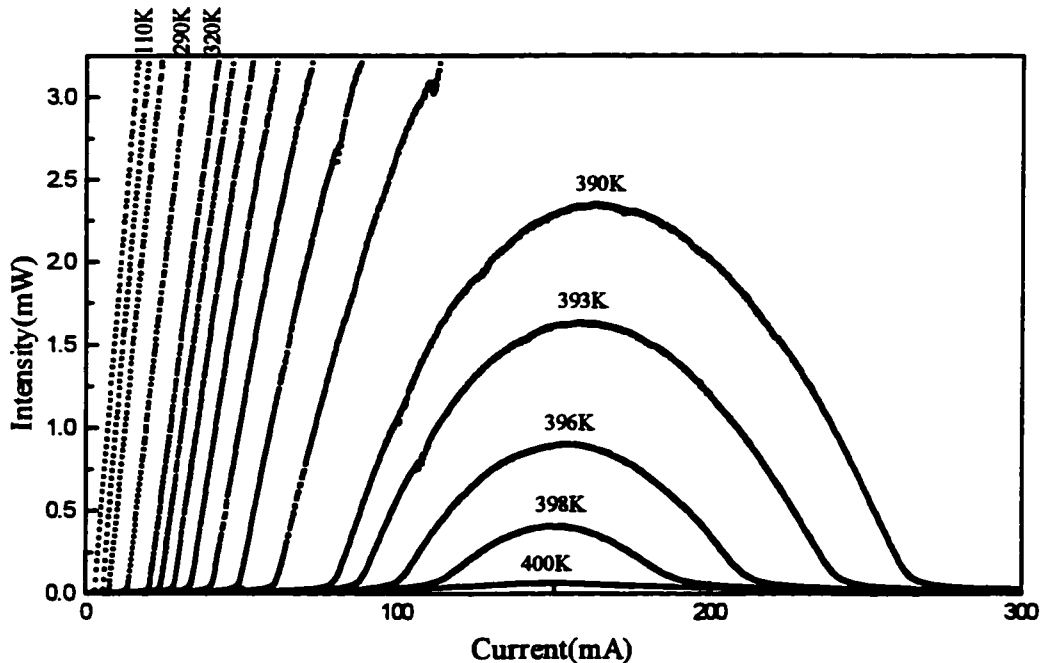


Fig.7.1.1 Typical L-I curves under CW operation for 1.3 μ m 1.2% three-well tensile SL-MQW laser with 2 μ m ridge width. The L-I curve at 390K shows a premature roll over caused by internal heating.

Though to measure the temperature rise caused by the driving current is theoretically interesting and practically very useful, it is difficult to measure the active region temperature directly, and the temperature changes may be deduced from various optoelectronic parameters which are sensitive to the temperature of the active region. Such parameters include the wavelength of the longitudinal modes and the peak of the emission spectrum [Suyama, 1981] [Ito, 1981], the lasing threshold current [Laff, 1978] [Ritchie, 1979], the terminal voltage, and the emitted optical

power. The temperature rise during CW operation may be deduced from a comparison of these parameters under CW and pulsed operation (such as 100ns and 0.1% duty cycle used in this research) of the laser, since the diode is essential at the temperature of the heat sink during operation with short pulses and low duty cycle.

In this chapter, a theoretical model is developed to measure the temperature rise during CW operation of different ridge width tensile SL-MQW lasers, and then their thermal impedances are deduced.

7.2 A Theoretical Model for Temperature Measurement Under CW Operation

It is noted that power output under a short pulse operating conditions is virtually a linear function of driving current above threshold current in all experiments. The output power P of a laser under pulsed operation(the pulse must be short enough to make heating negligible) is

$$P = \frac{h\nu}{q}(I - I_{th}(T)) \times \eta_d(T) \quad (7.2.1)$$

where $h\nu$ is the emission energy, q is the electron charge, I is the driving current, $I_{th}(T)$ is the threshold current, and $\eta_d(T)$ is the external quantum efficiency of the laser at temperature T . Both the I_{th} and η_d are strongly temperature-dependent and in short pulse operation, could be assumed independent of the driving current I . Therefore, from pulsed L-I measurement, the I_{th} vs. T and η_d vs. T can be determined as isothermal characteristics. Thus, the output power of the laser at any temperature for a given driving current can be determined.

Under CW operation, if a driving current I is applied to a laser, the temperature of the laser rises to T , which is the sum of T_{sub} and ΔT caused by the driving current I applied (so, the temperature of a laser is a function of substrate temperature T_{sub} and I). The output power P_{CW} is determined by (7.2.2), as schematically illustrated in Fig.7.2.1:

$$P_{\text{CW}} = \frac{h\nu}{q}(I - I_{\text{th}}(T)) \times \eta_{\text{d}}(T) \quad (7.2.2)$$

where $I_{\text{th}}(T)$ and $\eta_{\text{d}}(T)$ are the threshold current and the external quantum efficiency at temperature T , which can be determined from the measured L-I curve at temperature T under short pulse operation. To find out the temperature change of the laser with the driving currents I , after differentiating (7.2.2) with respect to I and with some mathematical manipulation, (7.2.2) can be written as:

$$\frac{dT}{dI} = \frac{(h\nu/q)(dP_{\text{CW}}/dI) - \eta_{\text{d}}(T)}{(I - I_{\text{th}}(T))(d\eta_{\text{d}}(T)/dT) - (dI_{\text{th}}(T)/dT)\eta_{\text{d}}(T)} \quad (7.2.3)$$

or

$$T = T_{\text{th}} + \int_{I_{\text{th}}}^I \frac{(h\nu/q)(dP_{\text{CW}}/dI) - \eta_{\text{d}}(T)}{(I - I_{\text{th}}(T))(d\eta_{\text{d}}(T)/dT) - (dI_{\text{th}}(T)/dI)\eta_{\text{d}}(T)} dI \quad (7.2.4)$$

where, T is the temperature of the laser at the driving current I , and T_{th} is the temperature of the laser at the threshold current under CW operation. From (7.2.3), it is seen that the temperature rise during CW operation causes a deterioration of η_{d} and an increase in I_{th} . The underlying assumptions in deriving (7.2.4) are that the

temperature is uniform around the active region and the external quantum efficiency of the laser is a unique function of temperature, independent of the driving current applied. The former assumption is questionable, however an average temperature around the active region is assumed.

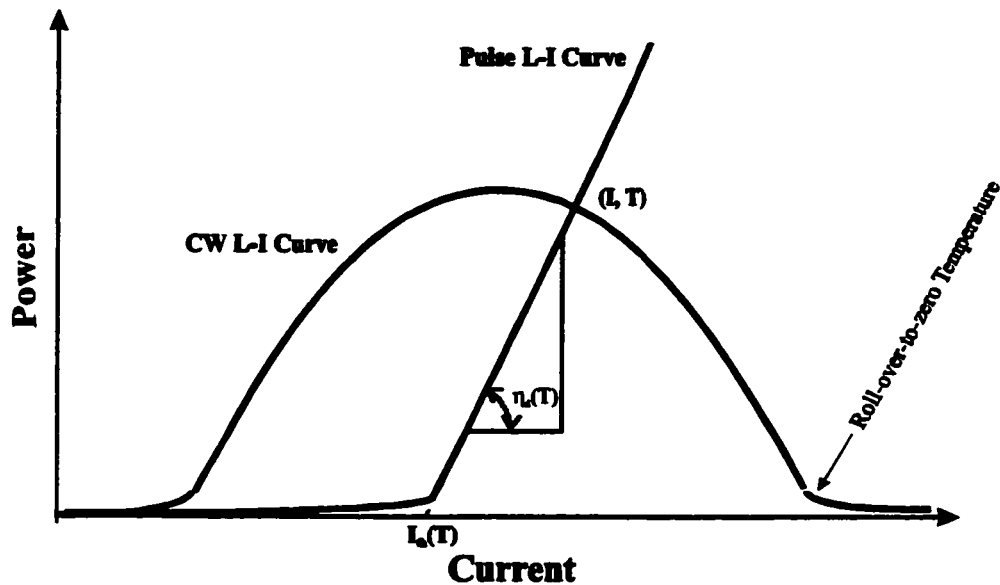


Fig.7.2.1 The schematic illustration of the L-I curve under CW operation and the L-I curve without any heating at temperature T

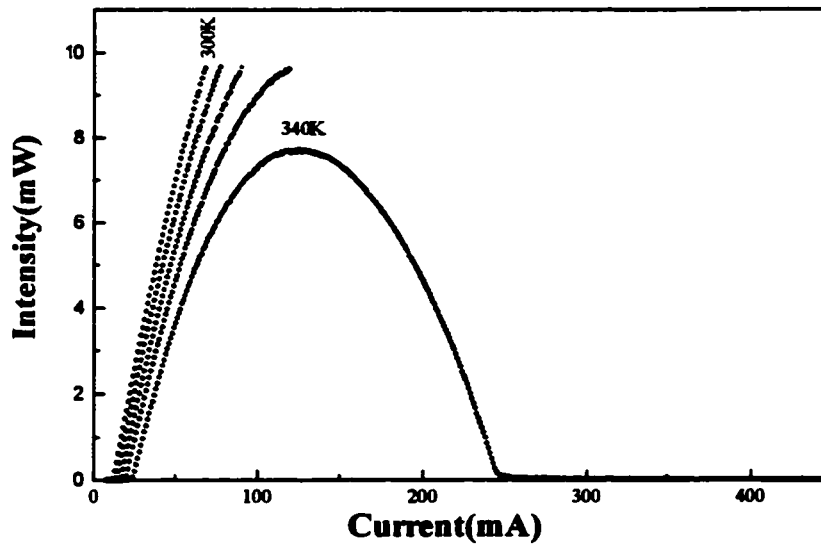
7.3 Temperature Rise Under CW Operation

The lasers investigated in this chapter are the tensile SL-MQW lasers containing three wells with varying ridge width, as used in chapter 6. The laser structure and the experimental procedure were detailed in chapter 2.

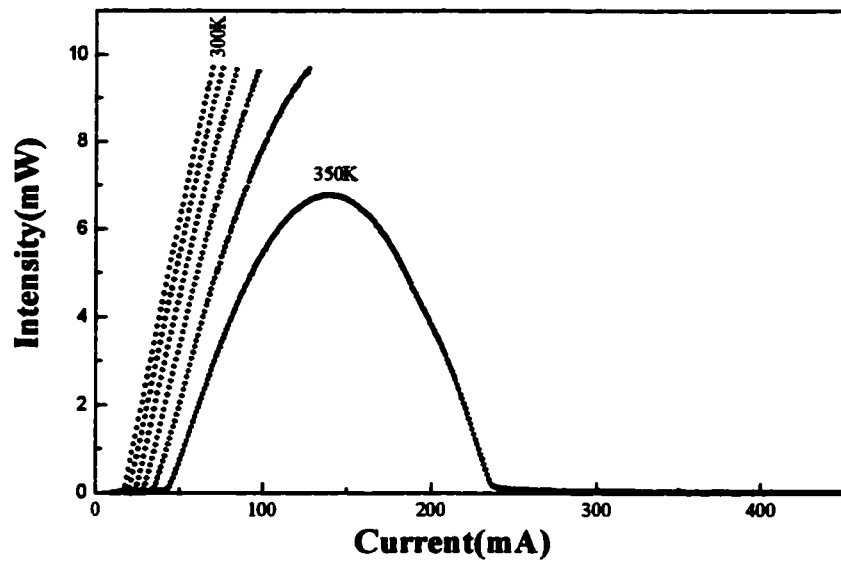
To determine the temperature rise during CW operation and then, the thermal impedance of the lasers, the L-I characteristics under CW operation are required, together with the I_{th} vs. T and η_d vs. T under short pulse operation in which heating can be ignored. The forward biased I-V characteristics under CW operation at various temperatures are needed to determine the power to be delivered to the devices.

7.3.1 Light-current Characteristics for Varying Ridge Width Laser Diode Under CW Operation

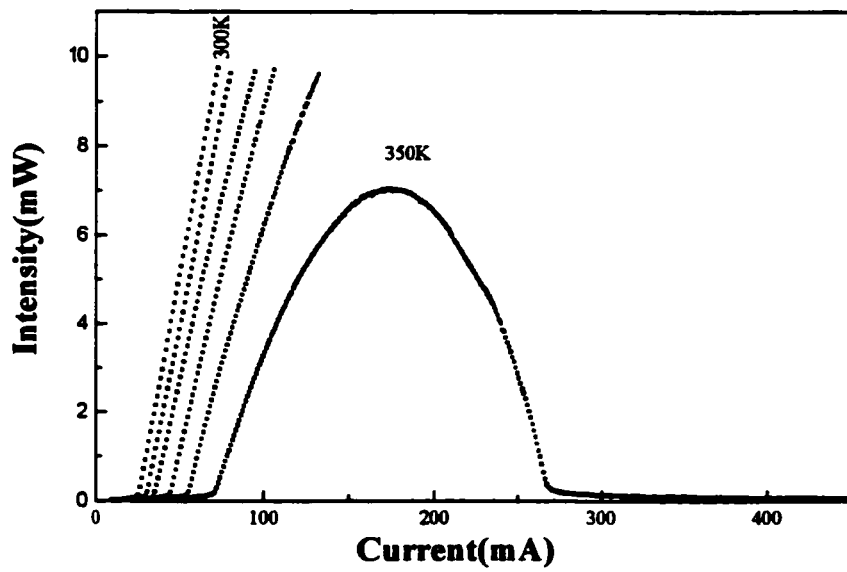
The light-current characteristics under CW operation at different temperatures up to 10 mW output power per facet for different ridge width laser diodes are shown in Fig.7.3.1(a)-(e).



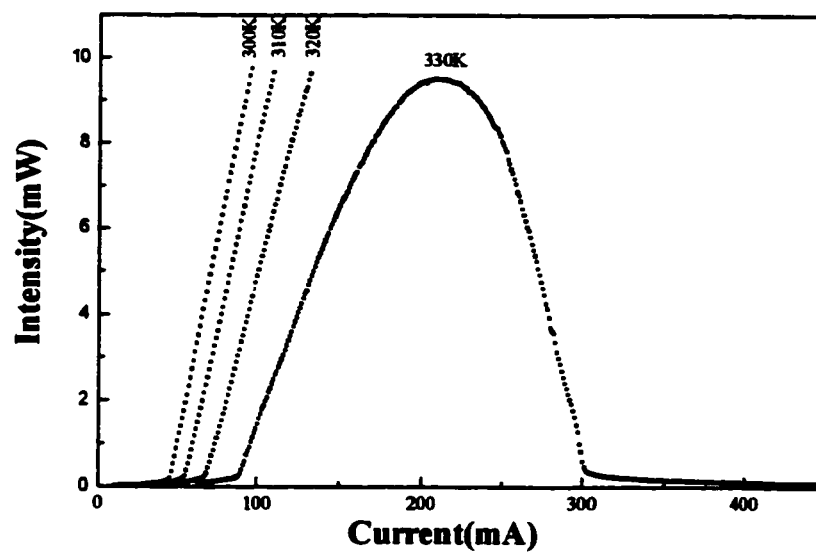
(a)



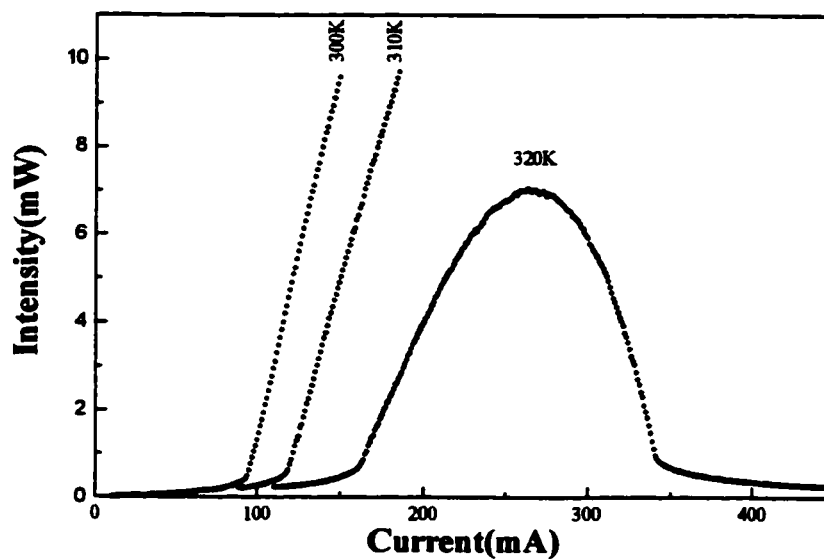
(b)



(c)



(d)



(e)

Fig.7.3.1 Light-current characteristics for (a)2 μm , (b)4 μm , (c)8 μm , (d)16 μm and (e)32 μm wide ridge waveguide lasers at different temperatures under CW operation

It is seen that initially the output power increases with the increasing driving current, reaches a maximum power, which is defined as maximum roll-over power $P_{\text{roll-over}}$, and thereafter decreases with increasing current. As seen from Fig.7.1.1, $P_{\text{roll-over}}$ decreases with increasing substrate temperature, T_{sub} . For $2\mu\text{m}$ wide laser the power output, as shown in Fig.7.3.1(a), is reduced to zero at a substrate temperature 340K and a current of 244mA. This is because at the T_{sub} , the active region of the laser is heated up to temperature T by the driving current I , and the threshold current at the temperature T is exactly equal to I . Therefore, at the current I the laser stops lasing, and the output power from the laser fades to zero.

According to (7.2.2), the driving current I , at which the output power rolls over to zero is determined by

$$I - I_{\text{th}}(T_{\text{zero}}) = 0 \quad (7.3.1)$$

where T_{zero} is defined as the roll-over-to-zero temperature, and $I_{\text{th}}(T_{\text{zero}})$ is the roll-over-to-zero current I_{zero} . The lowest substrate temperatures (defined as roll-over temperature), for which the output power rolls over at a power level below 10mW, of different ridge width lasers are listed in Table 7.3, in which it is seen that the roll-over temperature decreases with the ridge width.

Table 7.3.1 the roll over temperature for different ridge width tensile SL-MQW lasers under CW operation

ridge width(μm)	2	4	8	16	32
roll-over temperature(K)	340	350	350	330	320

7.3.2 I-V Characteristics Under CW Operation at Various Temperatures

Forward biased I-V characteristics were measured by the system shown in Fig.7.3.2 to determine the electrical power delivered to the devices under CW operation.

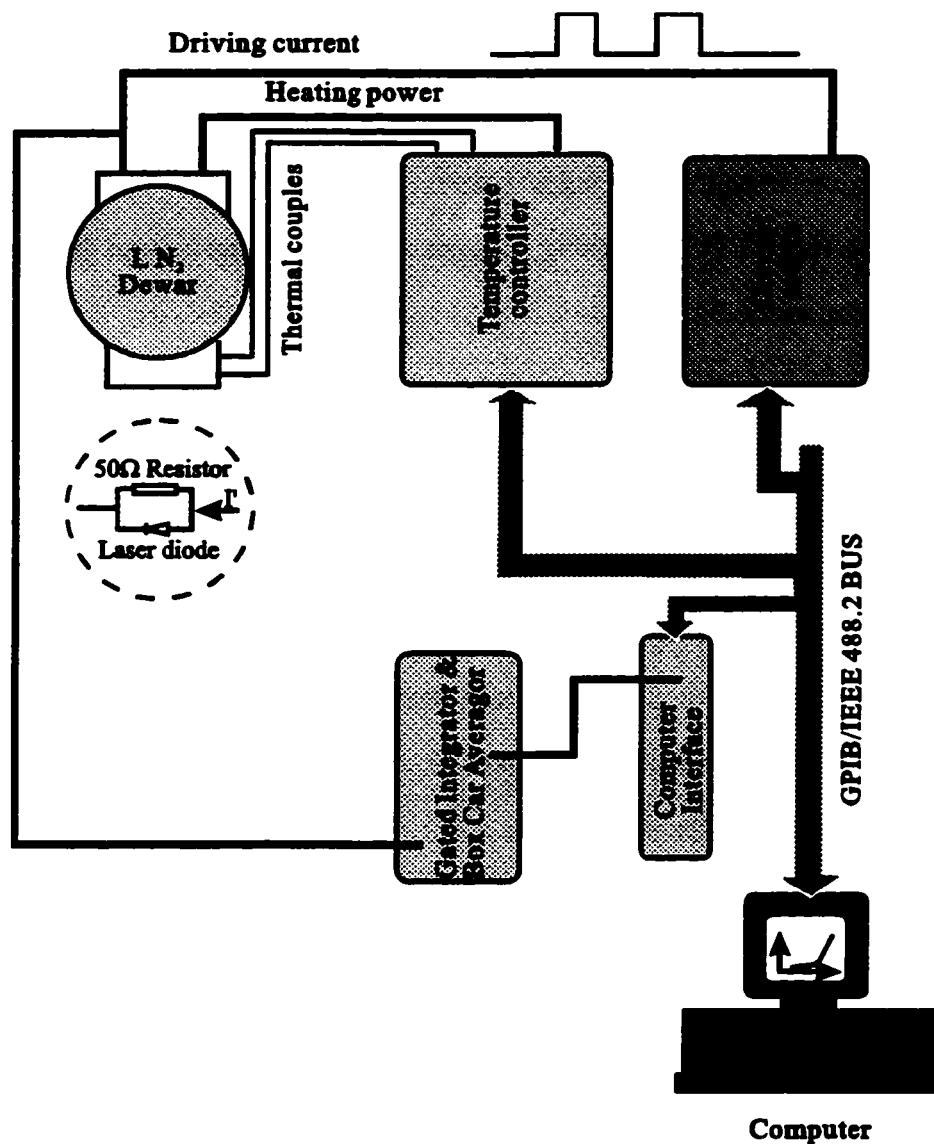


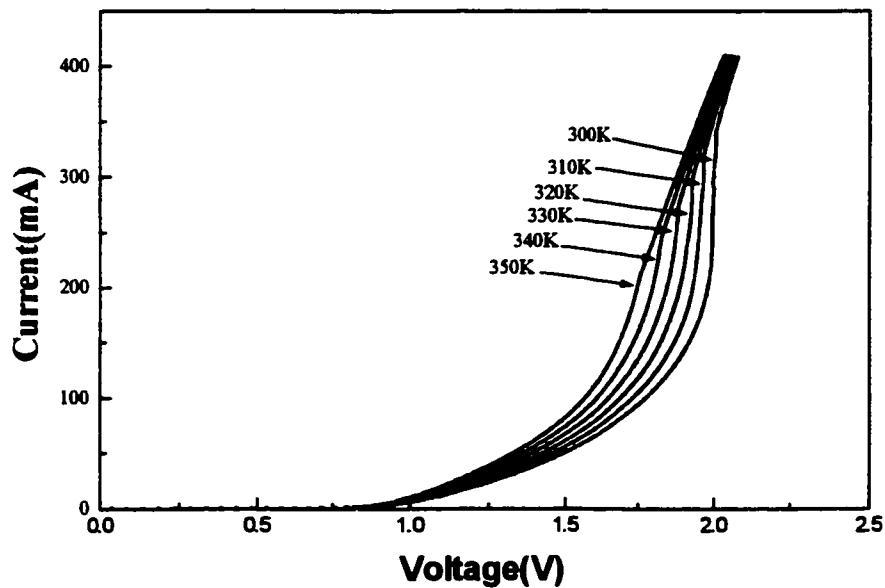
Fig. 7.3.2 Experimental set-up for I-V characterization at varying temperature under CW or pulsed operation

The set-up was a variant of the system for CW L-I measurement. A 50Ω resistor is placed in parallel with the laser diode. A current I' from the laser driver was supplied to the circuit, and the voltage V across the resistor was measured. Therefore, the current I , which flowed through the laser diode, is

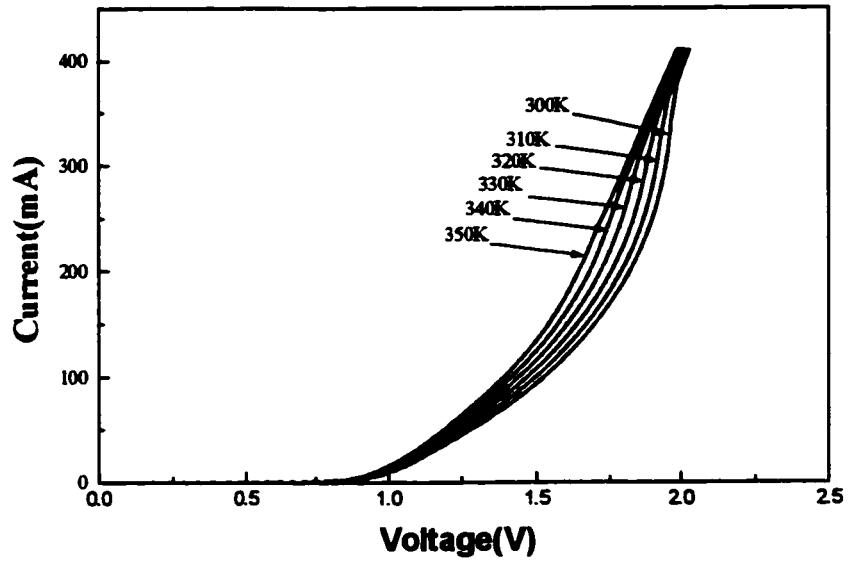
$$I = I' - (V/50) \quad (7.3.1)$$

With this arrangement, the I-V characteristics and the L-I characteristics of the laser under CW operation could be measured simultaneously.

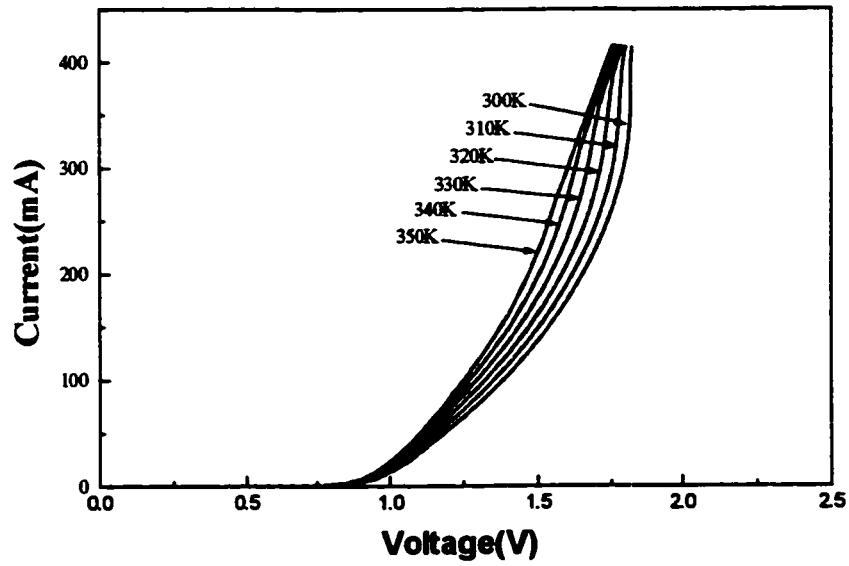
Forward biased I-V characteristics were measured with the L-I characteristics to determine the electrical power delivered to the devices under CW operation. The I-V characteristics for various ridge width lasers and with varying temperature are shown in Fig.7.3.3(a) - (e).



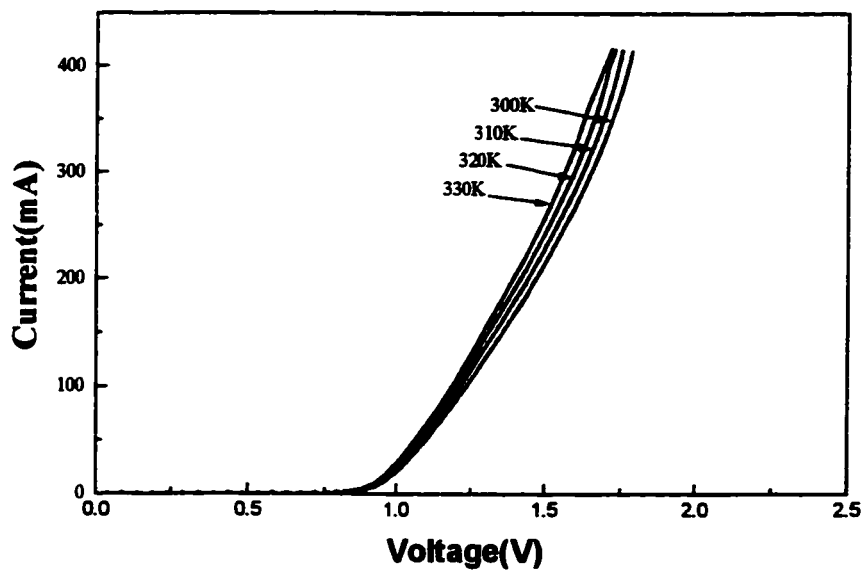
(a)



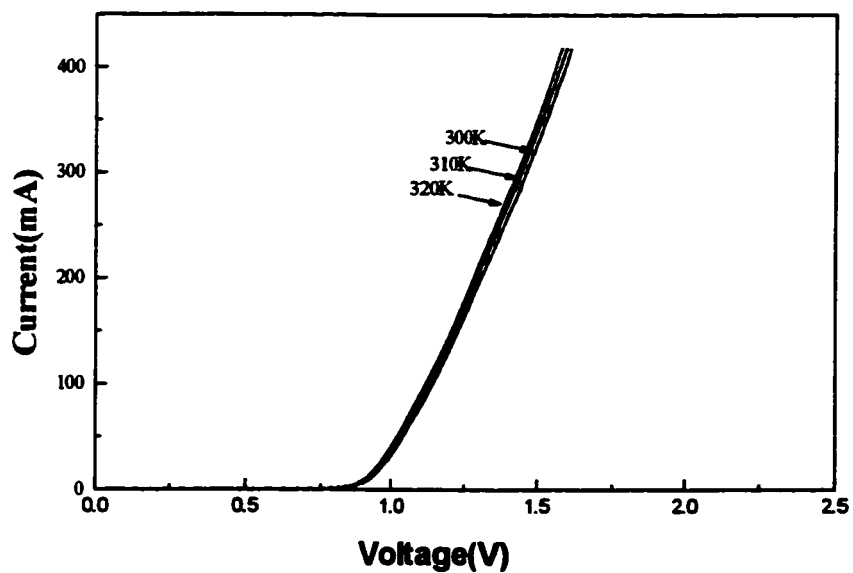
(b)



(c)



(d)

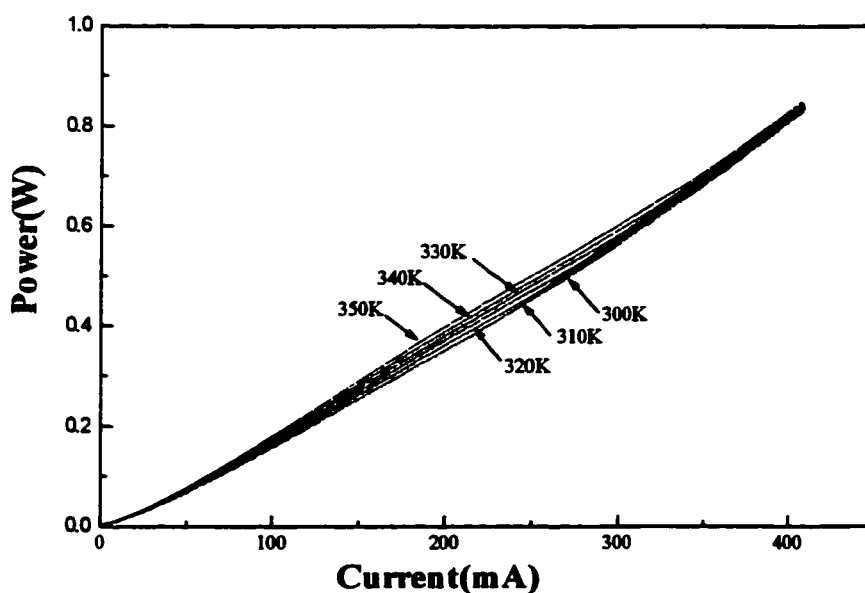


(e)

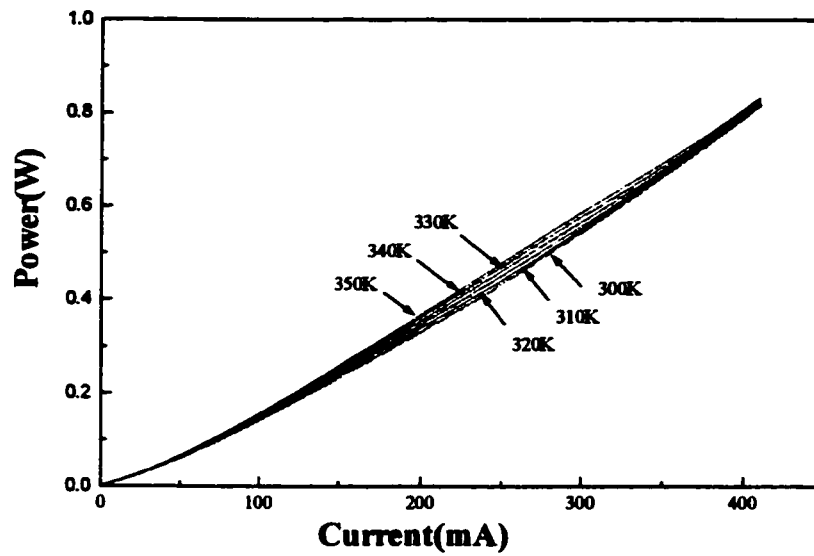
Fig.7.3.3 The current-voltage characteristics for varying ridge width lasers at different temperatures under CW operation: (a)2μm, (b)4μm, (c)8μm, (d)16μm, and (e)32μm.

The I-V curves are seen to shift to lower voltage with increasing temperature, and the temperature dependence of the narrower ridge laser is greater than the wider ridge laser. The inflection points indicated on the I-V curves by the cross signs correspond to the driving currents at which the output power rolls over to zero.

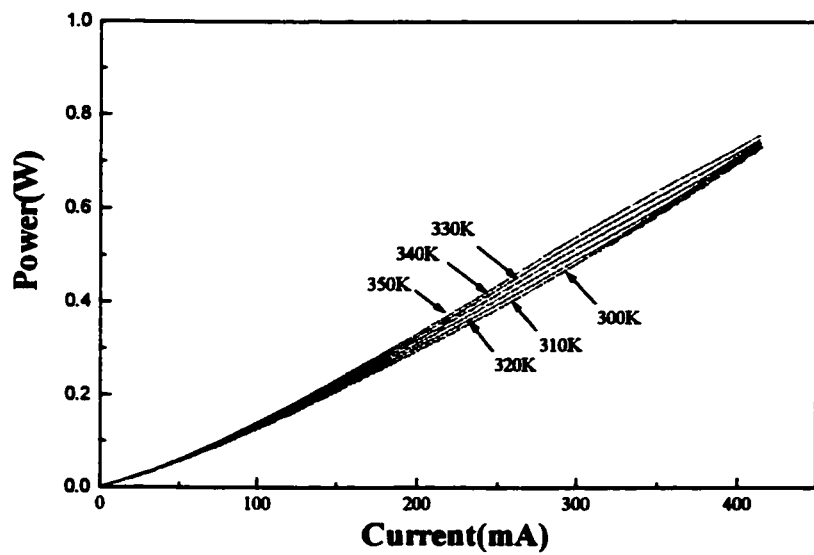
The power, which was calculated from the data shown in Fig. 7.3.3, is shown in Fig. 7.3.4 as a function of the driving current delivered to the devices at different temperatures. The power curves are seen to shift to lower current with increasing temperature. For same current to flow through the laser at same temperature, the narrower ridge width lasers needs higher power than the wider ridge width laser.



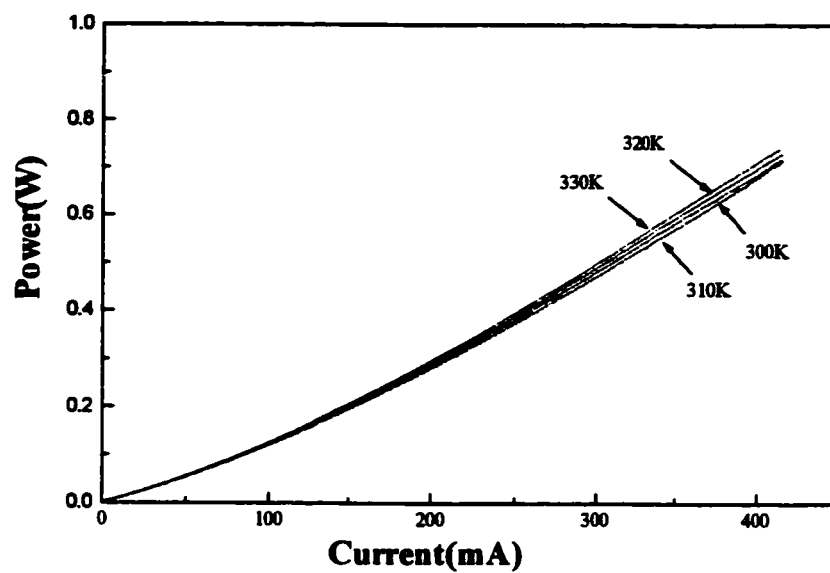
(a)



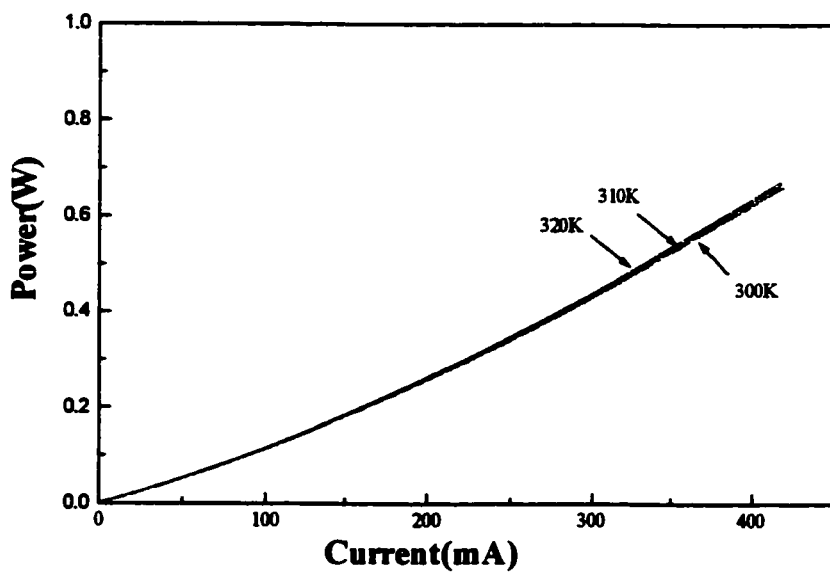
(b)



(c)



(d)

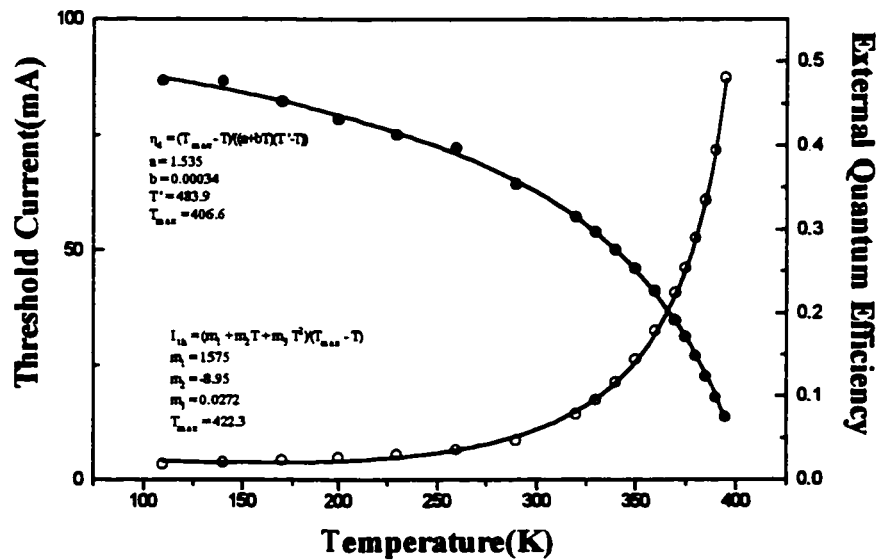


(e)

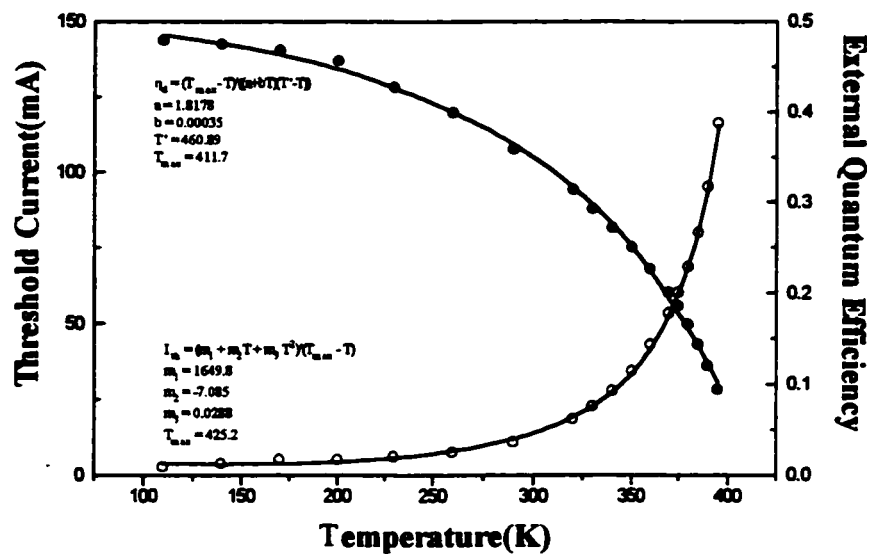
Fig.7.3.4 The electrical power as a function of driving current delivered to (a)2μm, (b)4μm, (c)8μm, (d)16μm, and (e)32μm laser diodes at different temperatures

7.3.3 Temperature Dependence of Threshold Current and External Quantum Efficiency

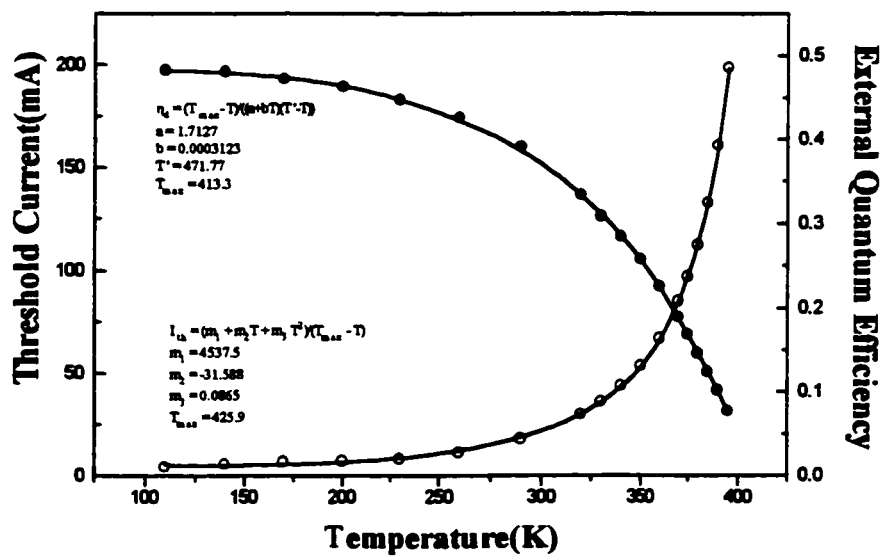
To determine the temperature rise during CW operation, the relationship of the I_{th} vs. T and η_d vs. T should be found. Since the heating in a laser diode during short pulse operation (e.g. 100ns at 10KHz used in this study) can be ignored, the intrinsic dependence of the I_{th} and η_d on temperature may be extracted from the L-I characteristics under pulse operation. The experimentally determined I_{th} vs. T and η_d vs. T under pulse operation are presented in Fig. 7.3.5. Equations (3.3.11) and (4.2.8) were used to fit the experimental results. The fitting parameters are listed in Table 7.3.2.



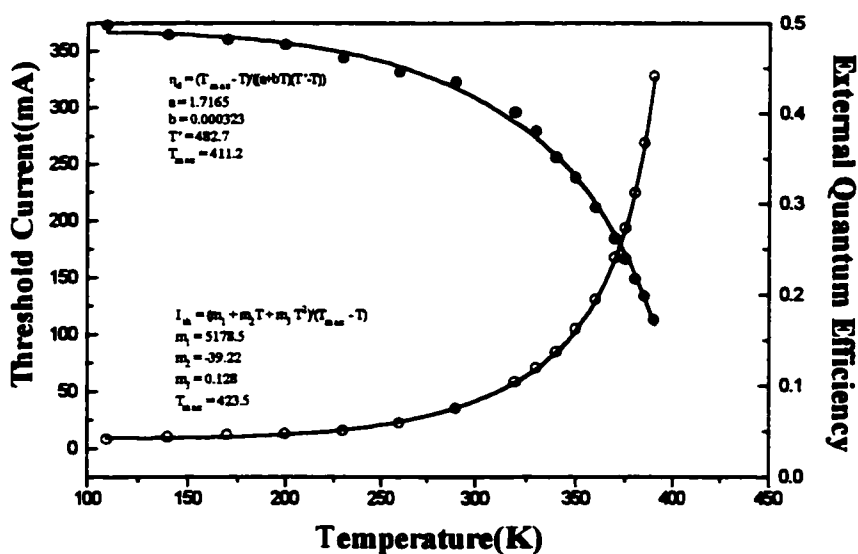
(a)



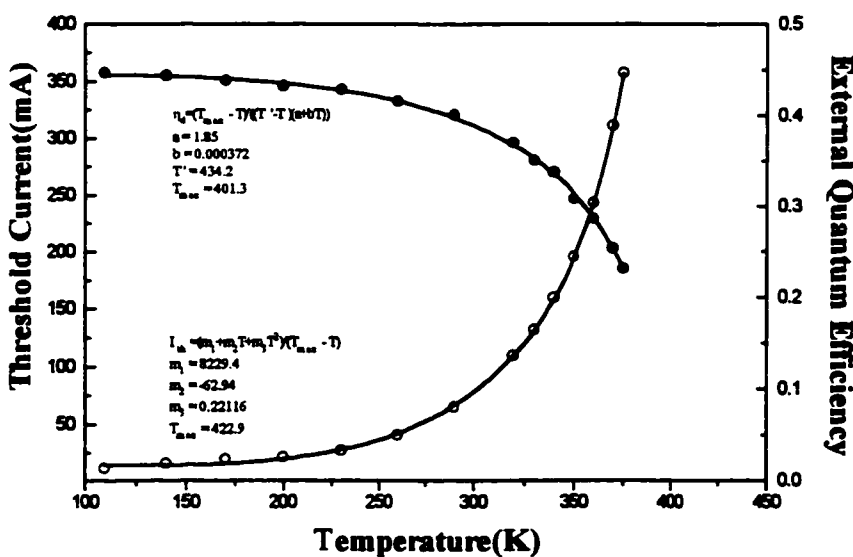
(b)



(c)



(d)



(e)

Fig.7.3.5 Experimentally determined temperature dependence of the threshold current and external quantum efficiency for (a)2 μ m, (a)4 μ m, (c)8 μ m, (d)16 μ m, and (e)32 μ m wide and 375 μ m long 1.3 μ m tensile SL-MQW lasers under 100ns at 10KHz pulses operation. The solid lines are fitting curves using (3.3.11) and (4.2.8). The insets are the fitting equations and fitting parameters.

Table 7.3.2 The fitting parameters for the threshold current and external quantum efficiency by (3.3.11) and (4.2.8)

ridge width	2(μm)	4(μm)	8(μm)	16(μm)	32(μm)
a	1.5735	1.8178	1.7127	1.7165	1.8487
b	0.00034	0.00035	0.00032	0.00032	0.00037
T'	483.87	460.89	471.77	482.68	434.19
$T_{\text{max}}(\eta_d)$	406.6	411.72	413.3	411.15	401.3
m ₁	1575	1649.8	4537.5	5178.5	8229.4
m ₂	-8.9477	-7.0853	-31.588	-39.227	-62.639
m ₃	0.0272	0.0288	0.0865	0.1278	0.2212
$T_{\text{max}}(I_{\text{th}})$	422.35	425.18	425.9	423.53	422.91

The maximum temperature obtained from fitting (3.3.11) to the experimental data for different ridge width lasers listed in Table 7.3.2 is shown in Fig.7.3.6. The solid line in Fig.7.3.6 is for eye catching and there is no apparent ridge width dependence of the maximum temperature, which is consistent with the theoretical expectation. The temperature dependence of the internal loss, which is described by the parameter b, is low in comparison to the compressive strain layer MQW lasers described in Chap. 4, and is independent of the ridge width of the lasers, as expected. The internal loss changes little with temperature for tensile strain layer MQW laser, which is consistent with the available experimental results on tensile strain layer MQW lasers [Evan, 1994], where the laser structure used is similar to one in this thesis.

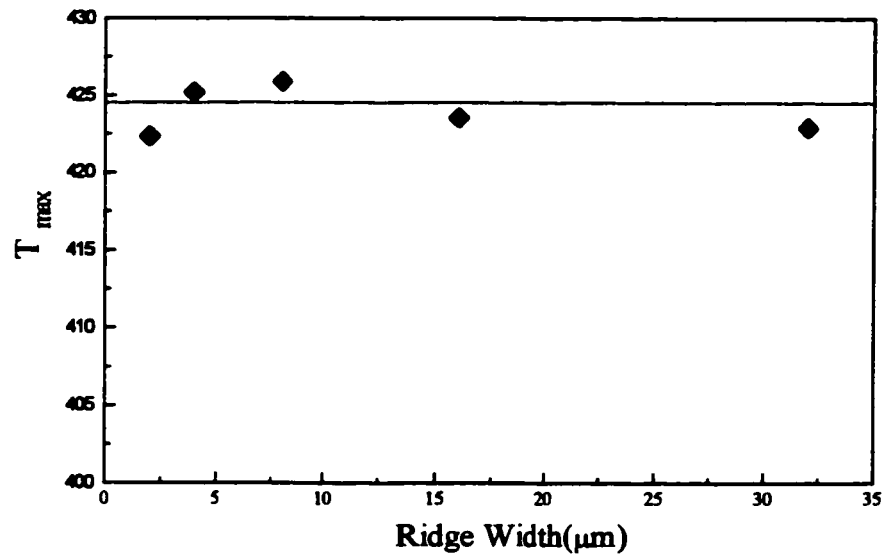


Fig.7.3.6 The dependence of T_{max} extracted from fitting (3.3.11) to the experimental data on the ridge width. The solid line is for eye-catching

The dependence of the threshold current on the ridge width at various temperatures is shown in Fig.7.3.7. The lines are fitted curves. The threshold current has an essentially linear relationship with the ridge width, which is consistent with available experimental observation [Hu, 1994]. The intercept of the fitting lines with the I_{th} axis gives the lateral leakage current [Hu, 1994]. Figure 7.3.7 shows that the lateral leakage current increases with increasing temperature. Figure 7.3.8 indicates that the external quantum efficiency is a function of temperature, but essentially independent of ridge width at constant temperature.

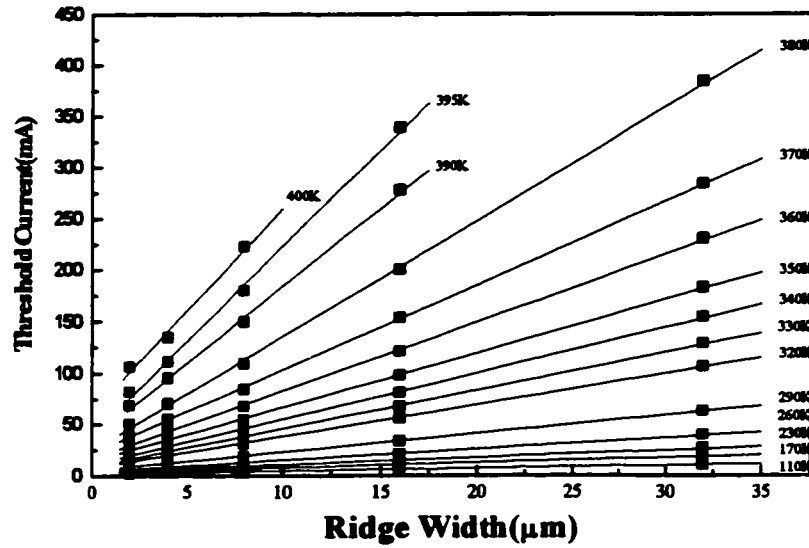


Fig. 7.3.7 The relationship of the threshold current with ridge width at various temperatures. The solid lines are linear fitting

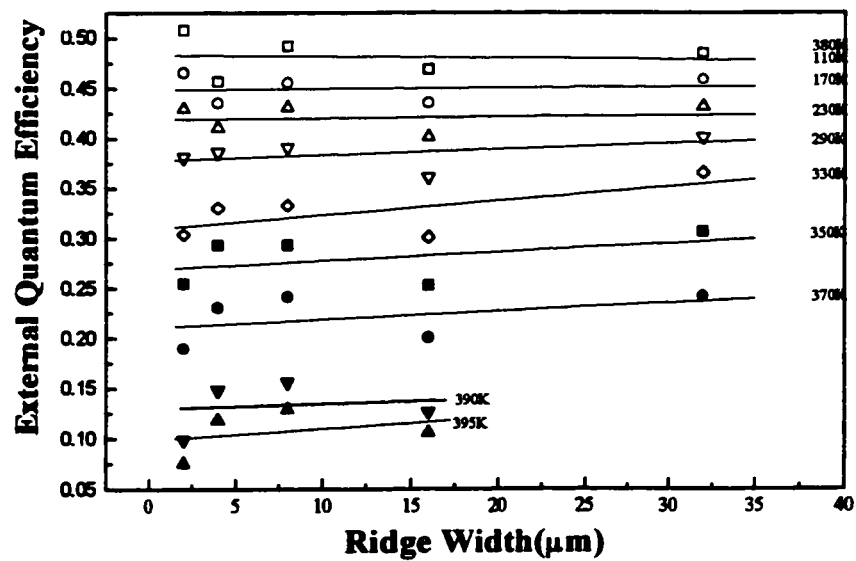
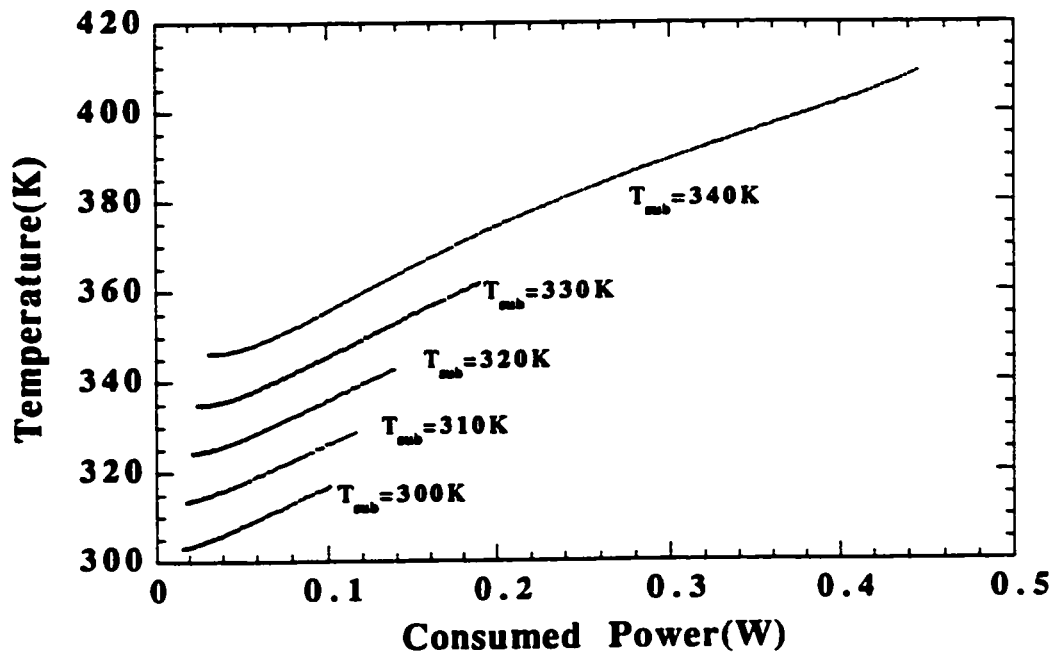


Fig. 7.3.8 The ridge width dependence of the external quantum efficiency at various temperatures

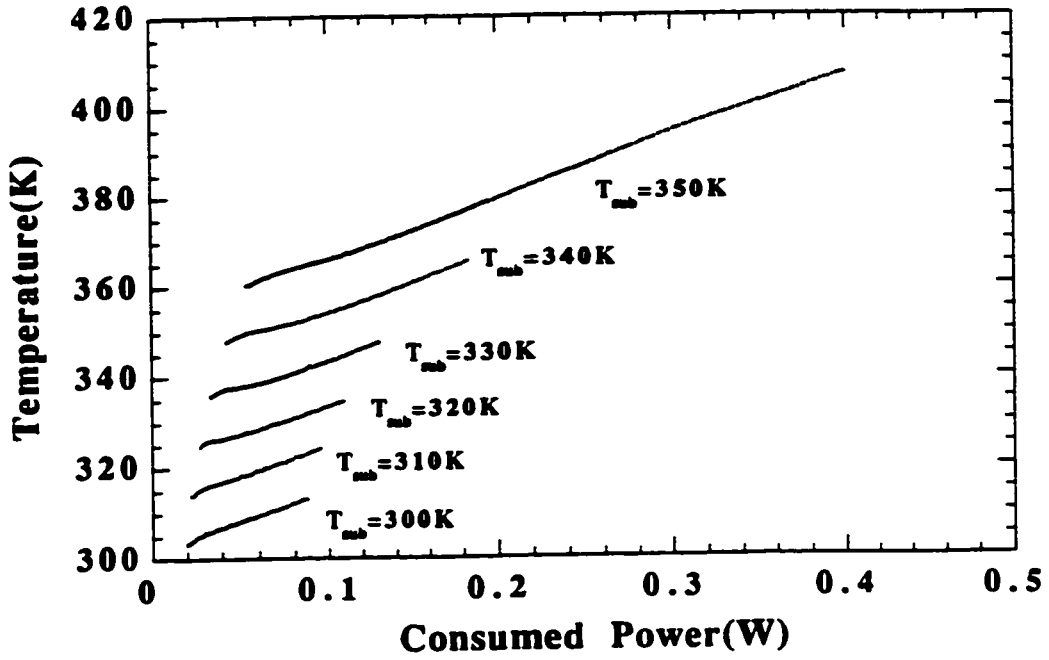
7.3.4 Thermal Impedance of Different Ridge Width Lasers

Using the measured I_{th} vs. T and η_d vs. T under 100ns at 10HKz pulse operation in (7.2.2), the temperature rises as a function of consumed power in laser diodes(the consumed power is defined here as the input power minus the output power of the laser)during CW operation at different substrate temperatures are shown in Fig. 7.3.9.

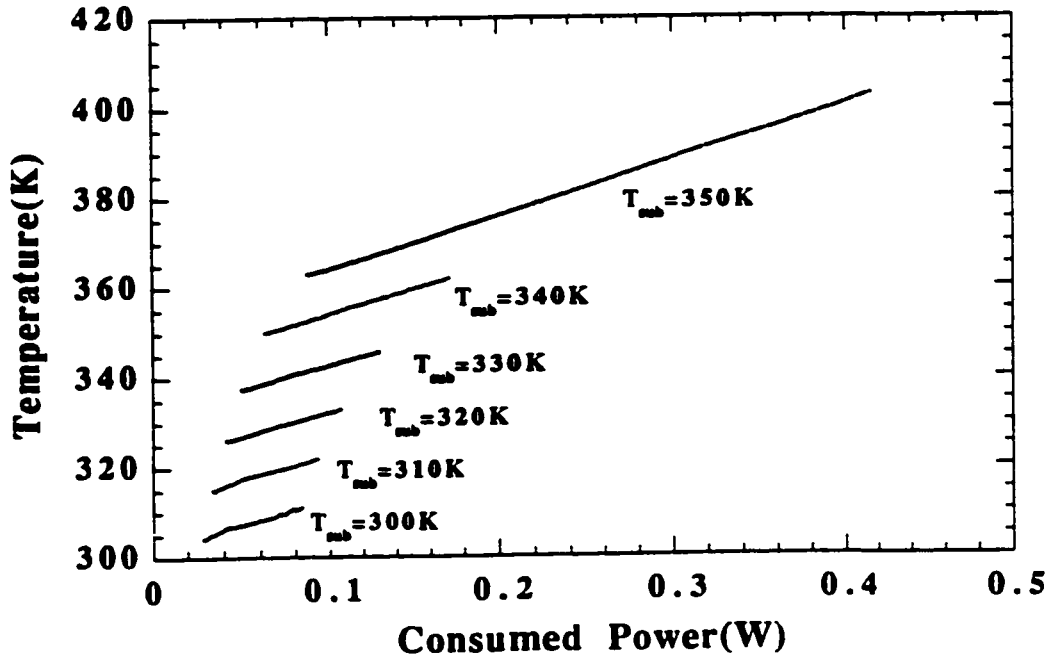
The starting point of each curve corresponds to the temperature at threshold during CW operation. The curves give the temperature T of the laser at a given consumed power and the substrate temperature, T_{sub} . The slopes of the curves at a given consumed power and temperature T determine the thermal impedances at that point.



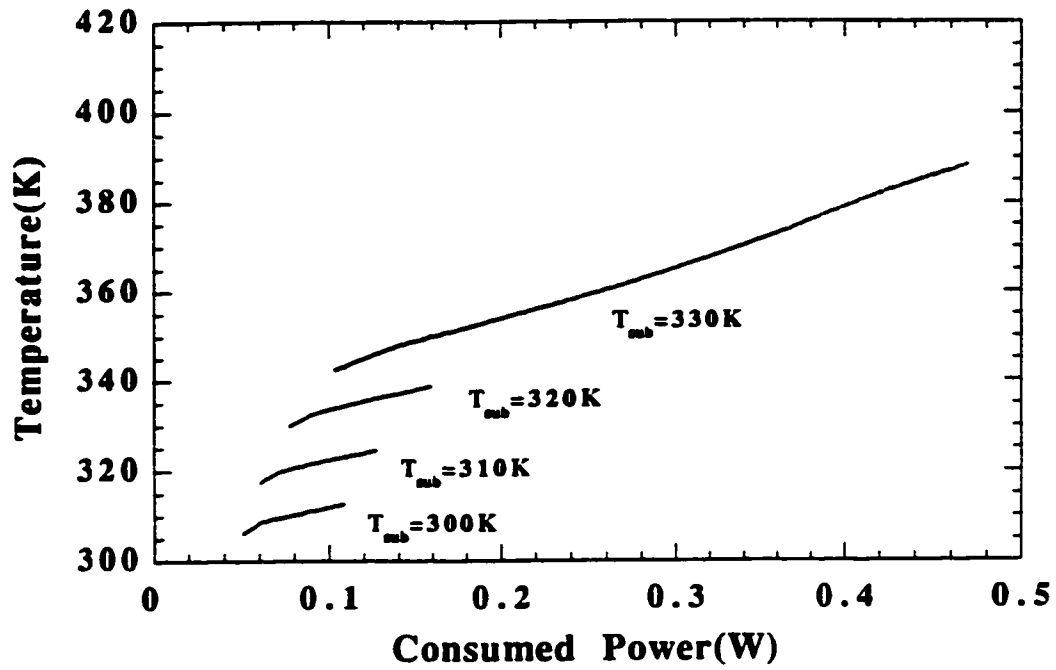
(a)



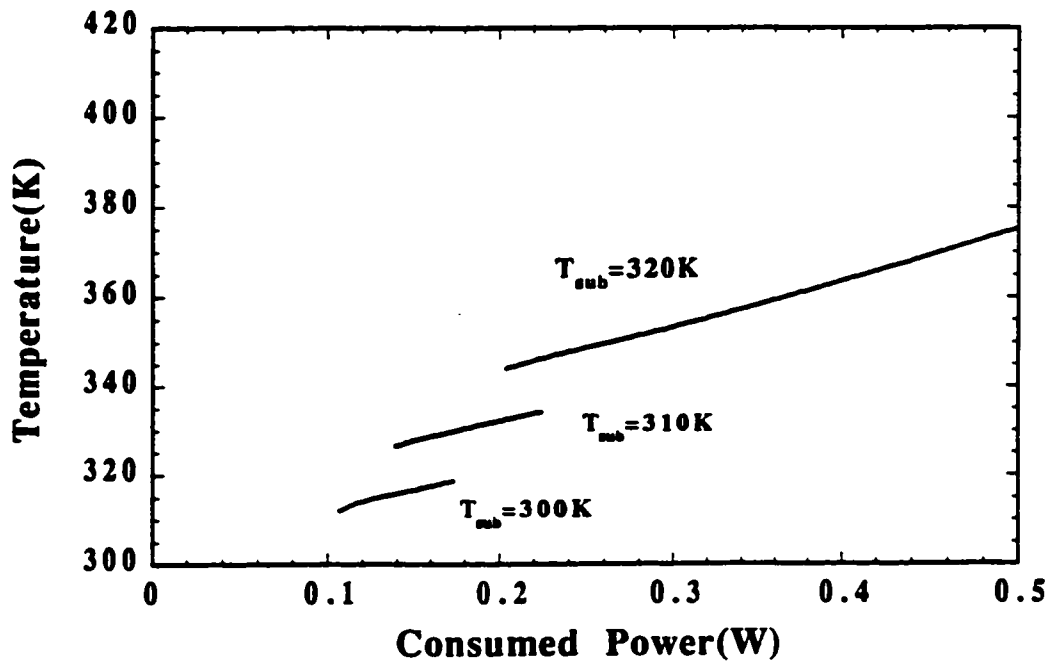
(b)



(c)



(d)



(e)

Fig.7.3.9 The temperature rise as a function of consumed power during CW operation for (a)2 μm , (b)4 μm , (c)8 μm , (d)16 μm , and (e)32 μm lasers

Table 7.3.3 lists the consumed power P_c at the roll-over-to-zero point, the lowest substrate temperature T_{sub} at which power output rolls over at a level below 10mW, and the temperature rise ΔT during whole roll-over period (from the point at which lasing begins to the point where lasing stops). These results show that T_{zero} decreases with increasing ridge width and ΔT is virtually independent of the ridge width.

Table 7.3.3 Consumed power P_c , T_{zero} , T_{sub} , and ΔT for different ridge width lasers

ridge width	2 μ m	4 μ m	8 μ m	16 μ m	32 μ m
P_c (W)	0.444	0.4	0.418	0.464	0.5
T_{zero} (K)	410	410	403	392	376
T_{sub} (K)	340	350	350	330	320
ΔT (K)	70	60	53	62	56

Since the temperature rises sublinearly with the consumed power above threshold, an average thermal impedance is used. The average thermal impedance above or below threshold are listed in Table 7.3.4. It is calculated by dividing the temperature rise by the consumed power run. Though the wider ridge lasers have the smaller thermal impedance, they have the lower maximum operating CW temperature because they have a higher temperature sensitivity of threshold current ($dI_{th}(T) / dT$), as observed experimentally.

7.4 Conclusions

The heating during CW operation limits the maximum CW operation temperature and the maximum available output power. Assuming that the external

quantum efficiency depends only on the temperature in active region of the laser, when the temperature dependence of I_{th} and η_d are known from the short pulse measurement, the temperature rise during CW operation was determined from CW L-I characteristics. Knowing the temperature rise, the thermal impedance, was calculated. A theoretical model was developed to measure the temperature rise during CW operation and the thermal impedance of different ridge width $1.3\mu\text{m}$ three-well tensile strain layer MQW lasers. In spite of the decrease of the thermal impedance with the ridge width, the wider ridge lasers have the lower roll-over substrate temperature.

Table 7.3.4 The average thermal impedance for different ridge width lasers above and below threshold

ridge width	$2\mu\text{m}$	$4\mu\text{m}$	$8\mu\text{m}$	$16\mu\text{m}$	$32\mu\text{m}$
above threshold(K/W)					
300(K)	149	134	112	113	101
310(K)	158	129	116	109	103
320(K)	155	135	109	106	105
330(K)	161	123	108	112	
340(K)	151	126	109		
350(K)		135	115		
below threshold(K/W)					
300(K)	185	167	145	122	112
310(K)	186	170	150	120	118
320(K)	196	172	147	129	119
330(K)	201	170	151	120	
340(K)	199	181	160		
350(K)		190	151		

Chapter 8

CONCLUSIONS

In this thesis extensive studies of the temperature characteristics of 1.3 μm strained layer multiple quantum well (MQW) lasers were carried out over a wide temperature range (110K to 460K). To find the intrinsic temperature characteristics of the threshold current, external quantum efficiency, and far field pattern, all experiments were carried out under short pulse (100ns @ 10kHz) operation to avoid any heating effects of the active region, except where the heating effect of the driving current on the laser was specifically studied and then the experiments were made under continuous wave operation. Two sets of lasers were used for this thesis. One set contains 5 to 14 compressively strained(0.7%) quantum wells, with a 2 μm ridge width, and was used to study the temperature dependence of the threshold current, external quantum efficiency, internal quantum efficiency and internal loss. Another set contains 3 tensile strained (1.2%) quantum wells, with varying ridge width (2 μm to 32 μm), and was used for the study of the temperature dependence of far field pattern and the heating effect of driving current on the lasers. By comparing the L-I curves measured under pulsed operation with those under CW operation, it was shown that the experiments carried out under short-pulse mode is necessary to extract the intrinsic I_{th} vs. T and η_d vs. T characteristics.

Based on assumptions that the deterioration of the optical gain with temperature dominates the temperature sensitivity of the laser performance and that the differential gain coefficient, β , decreases linearly with temperature, two formulae were derived in Chap.3 and 4 to describe the threshold current and the external quantum efficiency as functions of temperature. Excellent agreement was achieved between the theoretical analysis and the experimental data. A maximum operating temperature T_{\max} was extracted from fitting the formulae to I_{th} vs. T and η_d vs. T data. Both values of T_{\max} were found to be essentially identical, which experimentally verifies the theory and the underlying assumptions. It was found that T_{\max} is independent of the cavity length of the lasers, but increases with the number of wells until ten and then saturates for the given laser structure in this thesis.

In Chap. 5, the conventional method of determining the internal quantum efficiency and internal loss from a set of lasers with different length was examined. It was shown that the internal quantum efficiency, η_i^N , *nominal* internal quantum efficiency, is a function of temperature and has the same T_{\max} as the I_{th} and η_d , even though the true internal quantum efficiency, η_i , is independent of the temperature. It was also shown that if the phonon losses could be ignored the internal loss is virtually a linear function of temperature in agreement with experimental results.

In Chapter 6, pulse-mode experiments showed that when the temperature was raised from 110K to 390K, the far-field patterns of the 2 μm wide lasers hardly changes, which suggests that the injected carriers have little effect on the refractive index. However, for wider ridge lasers, the far field patterns are a function of temperature, which may be attributed to the spatial hole burning. The theoretical analysis and experimental results indicate that the simple slab waveguide theory is still an effective method for analyzing the lateral modes of the ridge waveguide lasers.

A technique was developed in Chapter 7 for measuring the temperature rise of the lasers during CW operation and was used to measure the temperature rise for the 1.3 μm 1.2% tensile strain layer MQW with varying ridge width. The experimental results indicate the wider ridge lasers have a smaller thermal resistance and a lower maximum CW operating temperature because it has a higher threshold current temperature sensitivity. The experimental results also indicates that T_{max} is independent of the ridge width. The internal loss of the lasers has a lower temperature dependence compared with the compressively strained MQW lasers.

APPENDIX

A.1 Band Gap of InGaAsP

In this appendix, some very useful physical parameters for the design of a compressive or tensile SL-MQW laser are summarized. At the end, a C program is attached used to calculate the quantum well composition (x and y in $\text{In}_{1-x}\text{Ga}_x\text{As}_y\text{P}_{1-y}$ quaternary material) for known strain, emission wavelength, and barrier height.

The application of strained layers in quantum well lasers has improved the performance of semiconductor lasers dramatically. The laser band structure, however, is still ambiguous. In this appendix, some recent published results of band lineup and in-plane effective mass of InGaAsP on [100] InP substrate are presented [Ishikawa, 1994].

Figure A.1 shows the conduction and valence band positions (in eV) of the binary materials relative to the InP valence band edge.

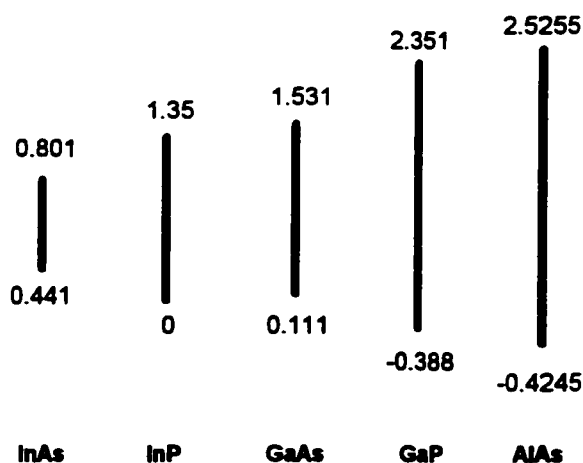


Fig.A.1 Band lineup of the binary materials which compose InGaAsP. The valence band edge energy of InP is set to zero.

Table A.I and A.II summarise some physical parameters for the binary materials, which can be used to construct the physical parameters for ternary or quaternary material.

Tab.A.I Physical Parameters of InP, InAs, GaP and GaAs

Parameter	Symbol	Unit	InP	InAs	GaP	GaAs
Lattice constant	d	Å	5.8688	6.0684	5.4512	5.5633
Bandgap energy	E_g	eV	1.35	0.36	2.74	1.42
Elastic stiffness constant	C_{11}	10^{11} dyn/cm ²	10.220	8.329	14.120	11.880
Elastic stiffness constant	C_{12}	10^{11} dyn/cm ²	5.760	4.526	6.253	5.380
Hydrostatic deformation potential for conduction band	a'	eV	4.5	4.1	7.9	6.8
Hydrostatic deformation potential for valence band	a	eV	2.9	2.5	3.0	2.7
Shear deformation potential for valence band	b	eV	-2.0	-1.8	-1.5	-1.7

Tab. A.II Bandgap nonlinearity parameter

Bandgap Nonlinearity	eV
$C_{In-Ga}(InGaP)$	0.70
$C_{In-Ga}(InGaAs)$	0.51
$C_{In-Al}(InAlAs)$	0.99
$C_{As-P}(InAsP)$	0.23
$C_{As-P}(GaAsP)$	0.30

The band gap energy of quaternary InGaAsP can be calculated by

$$\begin{aligned}
 E_g(x, y) = & xyE_g(GaAs) + (1-x)yE_g(InAs) + x(1-y)E_g(GaP) + (1-x)(1-y)E_g(InP) \\
 & + x(x-1)[yC_{In-Ga}(InGaAs) + (1-y)C_{In-Ga}(InGaP)] + y(y-1)[xC_{As-P}(GaAsP) \\
 & + (1-x)C_{As-P}(InAsP)]
 \end{aligned}$$

(A.1.1)

A.2 Energy Correction Induced by Strain

Assuming that the lattice constant of a substrate is d_s and the lattice constant of an epitaxial layer with no strain is d_e , a strain ϵ is defined as

$$\epsilon = \frac{d_e - d_s}{d_s} \quad (\text{A.2.1})$$

The energy correction in the conduction band induced by the strain can be described by

$$\Delta E_{\text{str, c}} = 2a' \frac{C_{11} - C_{12}}{C_{11}} \epsilon \quad (\text{A.2.2})$$

where a' is the hydrostatic deformation potential for the conduction band, C_{11} and C_{12} are the elastic stiffness constants. The energy corrections for the heavy and light hole valence bands are

$$\begin{aligned} \Delta E_{\text{str, c}} &= \left(2a \frac{C_{11} - C_{12}}{C_{11}} + b \frac{C_{11} + 2C_{12}}{C_{11}} \right) \epsilon \\ \Delta E_{\text{str, lh}} &= \left(2a \frac{C_{11} - C_{12}}{C_{11}} - b \frac{C_{11} + 2C_{12}}{C_{11}} \right) \epsilon \end{aligned} \quad (\text{A.2.3})$$

where a and b are the hydrostatic deformation potential and shear potential for the valence band, respectively.

A.3 Approximate Expression of Band Position

The approximate expressions of band position of InGaAs, InGaAsP are expressed as:

1) InGaAs:

$$\begin{aligned} E_c &= 1.040 - 0.0474\varepsilon + 0.003303\varepsilon^2 \\ E_{v,HH} &= 0.3331 + 0.05503\varepsilon - 0.002212\varepsilon^2 \\ E_{v,LH} &= 0.3331 - 0.01503\varepsilon - 0.003695\varepsilon^2 \end{aligned} \quad (\text{A.3.1})$$

2) InGaAsP:

a) $\varepsilon < 0$ tensile strain

$$\begin{aligned} E_c &= (0.6958 + 0.4846E_g) - 0.03031\varepsilon \\ E_{v,LH} &= (0.6958 - 0.5164E_g) - 0.03031\varepsilon \\ E_{v,HH} &= (0.6958 - 0.5164E_g) + 0.0397\varepsilon \end{aligned} \quad (\text{A.3.2})$$

b) $\varepsilon > 0$ compressive strain

$$\begin{aligned} E_c &= (0.6958 + 0.4836E_g) + 0.003382\varepsilon \\ E_{v,HH} &= (0.6958 - 0.5164E_g) + 0.003382\varepsilon \end{aligned} \quad (\text{A.3.3})$$

A.4 A computer program for the calculation of quantum well composition

Given the strain, emission wavelength, and barrier height, the following program written in C is to calculate the quantum well composition using above given parameters and formulae.

```
// This program is to determine the composition of a quantum well for desired
// wavelength, strain, width of well and barrier height
//
```

```
#include <stdio.h>
#include <stdlib.h>
#include <math.h>
```

```

#include <dos.h>

void main(void)
{
    // define variables for the composition and energy gap of well
    double wx, wy, energygapw;
    // define variables for the conduction and valence band position relative to InP
    double ECpositionw, EVpositionw;
    // define variables for the well depth of electron and hole
    double DELTAEC, DELTAEV;
    // first energy level in conduction quantum well and valence quantum well
    double ECfirstenergylevel, EVfirstenergylevel;

    //
    // Some parameters necessary for the calculation
    //

    double bx=0, by=0; // barrier's composition, no strain assumed
    double lz=3; //the well width in nm
    double expectedenergylevel=1.3; // the emission wavelength in m
    double epsilon=0; // the strain of quantum well in %

    char char-in;

    expectedenergylevel=1.24/expectedenergylevel; // convert into eV

    if (epsilon < 0) {
        char-in='L';
    }
    else char-in='H';

    // function prototype
    double firstenergylevel(double, double, double, double);
    double electronmass(double, double);
    double heavyholemass(double, double);
    double lightholemass(double, double);
    double latticeconstant(double, double);
    double energygap(double, double, double, char);

    double electronmassb=electronmass(bx, by); //electron's effective mass in barrier
    double heavymassb=heavyholemass(bx, by); // heavy hole's mass in barrier
    double lightmassb=lightholemass(bx, by); // light hole's mass in barrier
    double heavymassw=heavyholemass(wx, wy);
    double lightmassw=lightholemass(wx, wy);

```

```

switch(char_in) {
case 'L':
ECfirstenergylevel=firstenergylevel(electronmassw, electronmassb, lz,
DELTAEC);
EVfirstenergylevel=firstenergylevel(lightmassw, lightmassb, lz, DELTAEV);
break;

case 'H':
ECfirstenergylevel=firstenergylevel(electronmassw, electronmassb, lz,
DELTAEC);
EVfirstenergylevel=firstenergylevel(heavymassw, heavymassb, lz,
DELTAEV);
break;
}

// judge if the energy gap for the given wx and wy is expected
double residue2=energygapw+ECfirstenergylevel+EVfirstenergylevel
-expectedenergylevel;
ratio=residue2/residue1;
residue1=residue2;

wx=wx+0.0001;
} while ((ratio>0) || (residue1>0.001));

printf("This is the quantum well's composition and bandgap for      given
parameters, %g %g %g\n", wx, wy, energygapw);
printf("The electron and hole's masses, %g %g %g\n", electronmassw,
heavymassw, lightmassw);
printf("The electron and hole's first energy level, %g %g\n",
ECfirstenergylevel, EVfirstenergylevel);
}

// this function is to determine the energy bandgap of bulk material with strain epsilon

double energygap(double x, double y, double epsilon, char char_in)
{
double energygapwithstrain;
double aprime, a, b, c11, c12;

aprine=4.5+3.4*x-0.4*y-0.7*x*y;
a=2.9+0.1*x-0.4*y+0.1*x*y;
b=-2.0+0.5*x+0.2*y-0.4*x*y;
c11=10.220+3.9*x-1.891*y-0.39*x*y;

```

```

c12=5.760+0.493*x-1.234*y+0.361*x*y;

double DELTAEcbySTRAIN=2*aprime*(c11-c12)/c11*epsilon/100.0;
double DELTAEvbySTRAINforHH=(2.*a*(c11-
c12)/c11+b*(c11+2*c12)/c11)*epsilon/100.0;
double DELTAEvbystrainforLH=(2*a*(c11-c12)/c11-
b*(c11+2*c12)/c11)*epsilon/100.0;

switch (char_in)
{
case 'H':
energygapwithstrain=1.35+0.69*x-1.22*y- 0.21*y*x+0.7*x*x+0.23*y*y-
0.19*y*x*x+0.07*x*y*y+DELTAEcbySTRAIN+DELTAEvbySTRAI
NforHH;
break;

case 'L':
energygapwithstrain=1.35+0.69*x-1.22*y- 0.21*y*x+0.7*x*x+0.23*y*y-
0.19*y*x*x+0.07*x*y*y+DELTAEcbySTRAIN+DELTAEvbySTRAI
NforLH;
break;
}

return(energygapwithstrain);
}

// this function is to determine the lattice constant
double latticeconstant(double x, double y)
{
double latticeparameter;

latticeparameter=5.8688-0.4176*x+0.1996*y-0.0025*x*y;

return(latticeparameter);
}

// this function calculates the light hole mass in the unit of the mass of a free electron
double lightholemass(doubel x, double y)
{
double lhmass;

lhmass=0.12+0.04*x-0.096*y+0.004*x*y;

```

```

        return(lhmass);
    }

    // to calculate the heavy hole's mass

    double heavyholemass(double x, double y)
    {
        double hhmass;

        hhmass=0.6-0.06*x-0.19*y+0.15*x*y;

        return(hhmass);
    }

    // to calculate the electron's effective mass

    double electronmass(double x, double y)
    {
        double emass;

        emass=0.0765-0.116*x+0.026*y-0.059*x*y+(0.064-
        0.02*x)*y*y+(0.06+0.032*y)*x*x;

        return(emass);
    }

    // solve the quantum well with a width lz in nm, depth in ev

    double firstenergylevel(double mw, double mb, double lz, double welldepth)
    {
        double kz, f, firstlevel=0; INCREMENT=0.001;

        while(INCREMENT>=0.0001) {
            do {
                kz=5.1179*sqrt(mw*firstlevel);
                f=sqrt(firstlevel*mb)*tan(kz*lz/2)-sqrt((welldepth-
                firstlevel)*mw);
                firstlevel=firstlevel-2*INCREMENT;
                INCREMENT=INCREMENT/10.0;
            }
            return(firstlevel);
        }
    }

```

REFERENCES

- Ackerman, D.A., Shtengel, G.E., Hybertsen, M.S., Morton, P.A., Kazarinov, R.F., Tanbun-Ek, T., and Logan, R.A., "Analysis of Gain in Determining T_0 in $1.3\mu\text{m}$ Semiconductor Lasers," *IEEE J. Selected Topics in Quantum Electron.*, vol.1, pp.250-263, 1995
- Adachi, S., "Material parameters of $\text{In}_{1-x}\text{Ga}_x\text{As}_y\text{P}_{1-y}$ and related binaries," *J. Appl. Phys.*, vol. 53, pp.8775-8792, 1982
- Adachi, S., "Optical properties of $\text{In}_{1-x}\text{Ga}_x\text{As}_y\text{P}_{1-y}$ alloys," *Phys. Rev.*, vol.39, pp. 12612-12621, 1989-I
- Adachi, S., "Optical dispersion relations for GaP, GaAs, GaSb, InP, InAs, InSb, $\text{Al}_x\text{Ga}_{1-x}\text{As}$, and $\text{In}_{1-x}\text{Ga}_x\text{As}_y\text{P}_{1-y}$," *J. Appl. Phys.*, vol.66, pp.6030-6040, 1989
- Adams, A.R., Asada, M., Suematsu, Y., and Arai, A., "The temperature dependence of the efficiency and threshold current of $\text{In}_{1-x}\text{Ga}_x\text{As}_y\text{P}_{1-y}$ lasers related to intervalence band absorption." *Japanese J. Appl. Phys.*, vol. 19, pp.L621-L624, 1980
- Agrawal, G.P., "Lateral Analysis of Quasi-Index-Guided Injection Lasers: Transition from Gain to Index Guiding," *J. Lightwave Tech.*, vol. LT-2, pp. 537-543, 1984
- Agrawal, G.P., and Dutta, N.K., *Long-Wavelength Semiconductor Lasers*, van Nostrand Reinhold, New York, 1986
- Andrekson, P.A., Kazarinov, R.F., Olsson, N.A., Tanbun-Ek, T., and Logan, R.A., "Effect of thermionic Electron Emission from the Active Layer on the Internal Quantum Efficiency of InGaAsP Lasers Operating at $1.3\mu\text{m}$," *IEEE J. Quantum Electron.*, vol.32, pp.219-221, 1994
- Andrekson, P.A., Olsson, N.A., Tanbun-Ek, T., Logan, R.A., Coblenz, D. and Temkin, H., "Novel Technique for Determining Internal Loss of Individual Semiconductor Lasers," *Electron. Lett.*, vol. 28, pp.171-172, 1992
- Asada, M., Adams, A.R., Stubkjaer, K.E., Suematsu, Y., Itaya, Y., and Arai, S., "The temperature dependence of the threshold current of GaInAsP/InP DH lasers." *IEEE J. Quantum Electron.*, vol. 17, pp.611-618, 1981

- Asada, M., and Suematsu, Y., "Density-Matrix Theory of Semiconductor Lasers with Relaxation Broadening Model-Gain and Gain-Suppression in Semiconductor Lasers," *IEEE J. Quantum Electron.*, vol. QE.21 pp. 434-442, 1983
- Beernink, K.J., York, P.K., and Coleman, J.J., "Dependence of threshold current density of quantum well composition for strained-layer InGaAs-GaAs lasers by metallorganic chemical vapor deposition." *Appl. Phys. Lett.*, vol. 55, pp.2585-2587, 1989
- Bernussi, A.A., Pikal, J., and Temkin, H., "Rate equation model of high-temperature performance of InGaAsP quantum well lasers," *Appl. Phys. Lett.*, vol. 66, pp.3606-3608, 1995
- Casey, Jr. H.C., "Temperature dependence of the threshold current density in InP-Ga_{0.28}In_{0.72}As_{0.6}P_{0.4}($\lambda=1.3\mu\text{m}$) double heterostructure lasers." *J. Appl. Phys.*, vol.56, pp.1958-1964, 1984
- Champagne, Y., McCarthy, N., and R. Trembley, "Optical phase-conjugate feedback effects on gain-guided laser characteristics." *IEEE J. Quantum Electron.*, vol.25, pp.595-601, 1989
- Chik, K.D., and Richardson, B.A., "On the origin of the carrier leakage in GaInAsP/InP double-heterostructure lasers." *J. Appl. Phys.*, vol.67, pp.2660-2662, 1990
- Coleman, J.J., "Strained Layer Quantum Well Heterostructure Lasers, " in *Quantum Well Lasers*, Zory, P.S., Ed. New York: Academic Press, Inc., pp 367-413, 1993
- Coleman, J.J., Beernink, K.J., and Givens, M.E., "Threshold Current Density in Strained Layer In_xGa_{1-x}As-GaAs Quantum Well Heterostructure Lasers," *IEEE J. Quantum Electron.*, vol.28, pp.1983-2250, 1992
- Duda, E., Carballes, J., and Apruzzese, J., "Thermal Resistance and Temperature Distribution in Double-heterostructure Lasers: Calculations and Experimental Results," *IEEE J. Quantum Electron.*, vol. QE-15, pp.812-817, 1978
- Dutta, N.K., Lopata, J., Sivco, D.L., and Cho, A.Y., "Temperature dependence of threshold of strained quantum well lasers." *Appl. Phys. Lett.*, vol.58, pp.1125-1127, 1991
- Dutta, N.K., and Nelson, R.J., "The case for Auger recombination in In_{1-x}Ga_xAs_yP_{1-y}," *J. Appl. Phys.*, vol. 53, pp. 74-92, 1982
- Evans, J.D., "Effects of intentionally introduced mismatch strain on the operating characteristic and temperature performance of InGaAsP/InP Long wavelength semiconductor lasers," Ph.D Thesis, McMaster University, 1994

- Evans, J.D., Simmons, J.G., Thompson, D.A., Puetz, N., Makino, T., and Chik, G., "An Investigation into the Temperature Sensitivity of Strained and Unstrained Multiple Quantum Well, Long Wavelength Lasers: New Insight and Methods of Characterization," *J. Selected Topics in Quantum Electron.*, vol.1, pp.275-281, 1995
- Fang, W.W., Bethea, C.G., Chen, Y.K., and Chung, S.L., "Longitudinal Spatial Inhomogeneities in High-Power Semiconductor Lasers," *IEEE J. Selected Topics in Quantum Electron.*, vol.1, pp.117-127, 1995
- Garrett, B., and Whiteaway, J.E.A., "Self Stabilization of the fundamental lateral mode in index-guides semiconductor lasers," *IEE Proc. Pt.J*, vol. 134, pp.11-15, 1987
- Goodwin, A.R., Lovelace, D.H., and Selway, P.R., "Near-and Far-field emission distributions of mesa stripe geometry double heterostructure lasers," *Opto-electronics*, vol. 4, pp.311-321, 1972
- Goodwin, A.R., Peters, J.R., Pion, M., Thompson, G.H.B., and Whiteaway, J.E.A., "Threshold teperature characteristics of double heterostructure $Ga_{1-x}Al_xAs$ lasers," *J. Appl. Phys.*, vol.46, pp.3126-3131, 1975
- Hazzel, J.F., "The effect of varying barrier layer composition on the output characteristics of 1.3mm InGaAsP MQW lasers," Master Thesis, McMaster University, 1996
- Henry, C.H., "The Origin of Quantum Wells and the Quantum well laser," in *Quantum Well Lasers*, Zory, P.S. Jr., Ed. New York: Academic Press, Inc. , 1993 pp1-16
- Hess, O, Koch, S.W., and Moloney, J.V., "Filamentation and beam propagation in broad-area semiconductor lasers." *IEEE J. Quantum Electron.*, vol.31, pp.35-43, 1995
- Hirayama, H., Miyake, Y., and Asada, M., "Analysis of Current Injection Efficiency of Separate-Confinement-Heterostructure Quantum_film Lasers," *IEEE J. Quantum Electron.*, vol.28, pp.68-74, 1992
- Hirayama, H., Yoshida, J., Miyake, Y., and Asada, M., "Carrier Capture Time and Its Effect on The Efficiency of Quantum Well Lasers," *IEEE J. Quantum Electron.*, vol.30, pp.54-61, 1994
- Hirayama, H., Yoshida, J., Miyake, Y., and Asada, M., "Estimation of carrier capture time of quantum well lasers by spontaneous emission spectra," *Appl. Phys. Lett.*, vol.61, pp.2398-2400, 1992
- Hohimer, J.P., Hadley, G.R., and Owyong, A., "Mode control in broad-area diode lasers by thermally induced lateral index tailoring." *Appl. Phys. Lett.*, vol.52, pp.260-262, 1988

- Hu, S.Y., Young, D.B., Gossard, A.C., and Coldren, L.A., "The Effect of Lateral Leakage Current On the Experimental Gain/Current-Density Curve in Quantum-Well Ridge-Waveguide Lasers," *IEEE J. Quantum Electronic.*, vol.30, pp.2245-2250, 1994
- Hunziker, G., and Harder, C., "Beam quality of InGaAs ridge lasers at high output power," *App. Opt.*, vol.34, pp.6118-6122, 1995
- Ishikawa, T., and Bowers, J.E., "Band lineup and In-plane effective mass of InGaAsP or InGaAlAs on InP strained-layer quantum well." *IEEE J. Quantum Electron.*, vol.30, pp.562-570, 1994
- Ishikawa, M., Shiozawa, H., Itaya, K., Hatakoshi, G., and Uematsu, Y., "Temperature Dependence of the Threshold Current for InGaAlP Visible Laser Diodes," *IEEE J. Quantum Electron.*, vol. 27, pp. 23-28, 1991
- Ito, M., and Kimura, T., "Stationary transient thermal properties of semiconductor laser diodes." *IEEE J. Quantum Electron.*, vol.17, pp.787-795, 1981
- Jaeckel, H., Bona, G., Buchmann, P., Meier, H.P., Vettiger, P., Kozlovsky, W.J., and Lenth, W., "Very High-Power(425mW) AlGaAs SQW-GRINSCH Ridge Laser with Frequency-Doubled Output(41 mW at 428nm)," *IEEE J. Quantum Electron.*, vol.27, pp.1560-1566, 1991
- Jessop, P.E., private communication, 1995
- Joyce, W.B., "Carrier transport in double heterostructure active layers," *J.Appl.Phys.*, vol. 53, pp.7235-7239, 1982
- Kazarinov, R.F., and Pinto, M., "Carrier Transport in Laser Heterostructures," *IEEE J. Quantum Electron.*, vol. 30, pp.49-53, 1994
- Kogelnik, H., "theory of optical waveguide", in *Guidedwave Optoelectronics*, Tamir, T., New York, Springer-Verlag, pp.7-87, 1990
- Koren, v., Miller, B.I., Su, Y.K., Koch, T.L., and Bowers, J.E., "Low internal loss separate confinement heterostructure InGaAs/InGaAsP quantum well laser." *Appl/ Phys. Lett.*, vol.51, pp.1744-1746, 1987
- Laff, R.A., Comerford, L.D., Crow, J.D., and Brody, M.J., "Thermal performance and limitations of silicon-substrate packaged GaAs laser arrays." *Appl.Opt.*, vol.17, pp.778-, 1978

- Lang, R. "Lateral transverse mode instability and its stabilization in stripe geometry injection lasers," *IEEE J. Quantum Electron.* vol.15, pp.718-726, 1979
- Larsson, A., Cody, J., and Lang, R.J., "Strained-layer InGaAs/GaAs/AlGaAs single quantum well-lasers with high internal quantum efficiency." *Appl. Phys. Lett.*, vol.55, pp.2268-2270, 1989
- Lau, K.Y., "Dynamics of quantum well lasers." in *Quantum Well Lasers*, Zory, P.S., Ed., New York:Academic Press, Inc., pp.217-276, 1993
- Li, Z.M., and Bradford, T., "A Comparative Study of Temperature Sensitivity of InGaAsP and AlGaAs MQW Lasers Using Numerical Simulations," *IEEE J. Quantum Electron.*, vol. 31, pp. 1841-1847, 1995
- Lui, W.W., Yamanaka, T., Yoshikuni, Y., Seki, S., and Yokoyama, K., "Unifying explanation for recent temperature sensitivity measurements of Auger recombination effects in strained InGaAs/InGaAsP quantum well lasers." *Appl. Phys. Lett.*, vol. 63, pp.1616-1618, 1993
- Lundstrom, M., and Schuelke, R.J., "Numerical Analysis of Heterostructure Semiconductor Devices," *IEEE Transactions on Electron Devices*, vol.ED-30, 1151-1224, 1983
- Manning, J.S., "Thermal impedance of diode lasers: Comparison of experimental methods and a theoretical model," *J. Appl. Phys.*, vol. 52, pp.3179-3184, 1981
- Marciante, J.R., and Agrawal, G.P., "Nonlinear mechanisms of filamentation in broad-area semiconductor lasers." *IEEE J. Quantum Electron.*, vol.32, pp.590-596, 1996
- Masayuki Ishikawa, H. Shiozawa, K. Itaya, G. Hatakoshi, and Y. Uematsu, "Temperature Dependence of the Threshold Current for InGaAlP Visible Laser Diodes," *IEEE J. Quantum Electron.*, vol.27, pp.23-28, 1991
- Mikhelashvili, V., Tessler, N., Nagar, R., Eisenstein, G., Dentai, A.G., Chandrasakhar, S., and Joyner, C.H., "Temperature dependent loss and overflow effects in quantum well lasers." *IEEE Photon. Tech. Lett.*, vol.6, pp.1293-1295, 1994
- Morkoc, H., Sverdlov, B., and Gao, G., "Strained Layer Heterostructures, and their applications to MODFET's, HBT's, and Lasers," *Proc. of the IEEE*, vol.81, pp.493-556, 1993
- Nabiev, R.F., Vail, E.C., and Chang-Hasnain, C.J., "Temperature Dependent Efficiency and Modulation Characteristics of Al-Free 980-nm Laser Diodes," *IEEE J. Selected Topics in Quantum Electron.*, vol.1, pp.234-243, 1995

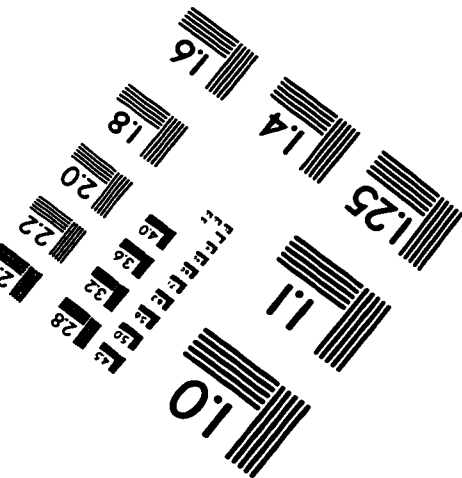
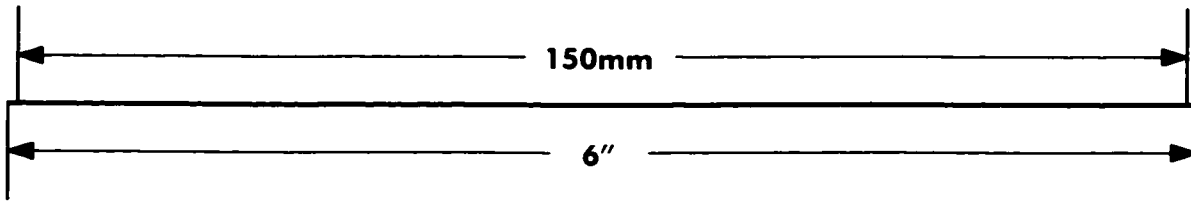
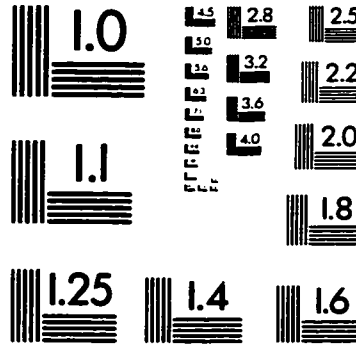
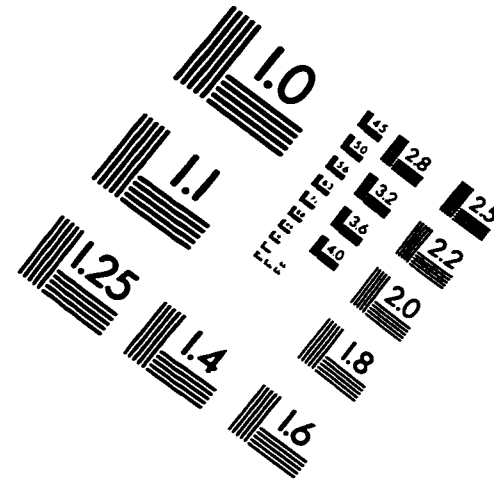
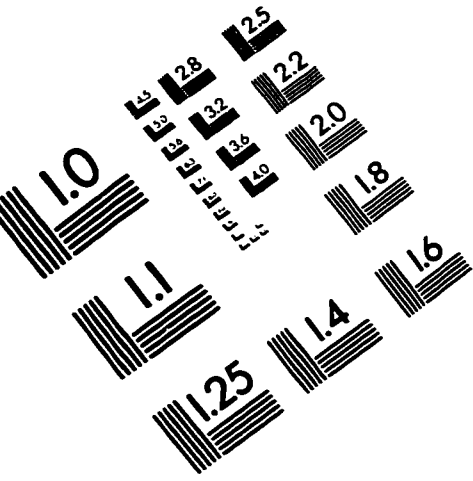
- Nappi, J., Ovtchinnikov, A., Asonen, H., Savolainen, P., and Pessa, M., "Limitations of two-dimensional passive waveguide model for $\approx 980\text{nm}$ Al-free ridge waveguide lasers," *Appl. Phys. Lett.* vol. 64, pp.2203-2205, 1994
- Nie-vesperinas, *Scattering and Diffraction in Physical Optics*(wiley, New York, 1991), sec. 6.4
- O'Gorman, J., Levi, A.F.J., Schmitt-Rink, S., Tanbun-Ek, T., Coblenz, D.L., and Logan, R.A., "On the temperature sensitivity on semiconductor lasers," *Appl. Phys. Lett.*, vol. 60, pp. 157-159, 1992
- O'Gorman, J., Levi, A.F.J., Tanbun-Ek, T., Coblenz, D.L., and Logan, R.A., "Temperature dependence of long wavelength semiconductor lasers," *Appl. Phys. Lett.*, vol. 60, pp.1058-1060, 1992
- Oohashi, H., Seki, S., Hirono, T., Sugiura, H., Amano, T., Ueki, M., Nakano, J., Yamamoto, M., Tohmori, Y., Fukuda and Yokoyama, K., "High-power and high-efficiency $1.3\mu\text{m}$ InAsP compressively-strained MQW lasers at high temperature," *Electron. Lett.*, vol.31, pp. , 1995
- O'Reilly, E.P., and Silver, M., "Temperature sensitivity and high temperature operation of long wavelength semiconductor lasers," *Appl. Phys. Lett.*, vol. 63, pp.3318-3320, 1993
- O'Reilly, E.P., and Adams, A.R., "Band-structure Engineering in Strained Semiconductor Lasers," *J. Quantum Electron.*, vol. 30, pp 366-379, 1994
- Pankove, J.I., "Temperature dependence of emission efficiency and lasing threshold in laser diode." *IEEE J. Quantum Electron.*, vol.4, pp.119-122, 1968
- Paxton, A.H., Dente, G.C., "Filament formation in semiconductor laser gain regions." *J. Appl. Phys.*, vol.70, pp.2921-2925, 1991
- Piprek, J., and Nurnberg, R., "Calculation of the temperature distribution in ridged-waveguide laser diodes." *Sov. J. Quantum Electron.*, vol.18, pp.1408-1409, 1989
- Reisinger, A.R., Zory, P.S., and Waters, R., "Cavity Length Dependence of the Threshold Behaviour in Thin Quantum Well Semiconductor Lasers," *IEEE J. Quantum Electron.*, vol.QE-23, pp.993-999, 1987
- Ritchie, S., "Thermal properties of semiconductor lasers, and the interpretation of thermal-resistance measurement." *IEE J. Solid-state & Electron Devices*, vol.3, pp.201-205, 1979

- Rideout, W., Sharfin, W.F., Koteles, E.S., Vassell, M.O., and Elman, B., "Well-Barrier Hole Burning in Quantum Well Lasers," *IEEE Photon Tech. Lett.*, vol.3, pp. 784-786, 1991
- Schatz, R., and Bethea, C.G., "Steady state model for facet heating leading to thermal runaway in semiconductor lasers," *J. Appl. Phys.*, vol.76, pp.2509-2521, 1994
- Seki, S., Lui, W.W., and Yokoyama, K., "Explanation for the temperature insensitivity of the Auger recombination rates in 1.55 μm InP-based strained layer quantum well lasers," *Appl. Phys. Lett.*, vol. 66, pp.3093-3095, 1995
- Seki, S., Yamanaka, T., Lui, W., and Yokoyama, K., "Theoretical analysis of differential gain of 1.55 μm InGaAsP/InP compressive-strained multiple-quantum well lasers," *J. Appl. Phys.*, vol.75, pp.1299-1303, 1994
- Seki, S., Yamanaka, T., Lui, W., Yoshikuni, Y., and Yokoyama, K., "Theoretical Analysis of Pure Effects of Strain and Quantum Confinement on Differential Gain in InGaAsP/InP Strained-Layer Quantum-Well Lasers," *IEEE J. Quantum Electron.*, vol. 30, pp.500-510, 1994
- Seki, S., and Yokoyama, K., "Theoretical Analysis of Temperature Sensitivity of Differential Gain in 1.5 μm InGaAsP-InP Quantum Well Lasers," *IEEE Photon. Lett.*, vol. 7, pp.251-253, 1995
- Seki, S., Yokoyama, K., and Sotirelis, P., "Theoretical Analysis of High Temperature Characteristics of 1.3 μm InP-Based Quantum Well Lasers," *IEEE J. Selected Topics in Quantum Electron.*, vol.1, pp.264-273, 1995
- Silver, M., and O'Reilly, E.P., "Optimization of Long Wavelength InGaAsP Strained Quantum Well Lasers," *IEEE J. Quantum Electron.*, vol.31, pp.1193-1200, 1995
- Smowton, P.M., and Blood, P., "GaInP-(Al_yGa_{1-y})InP 670 nm Quantum-Well Lasers for High-Temperature Operation," *IEEE J. Quantum Electron.*, vol.31, pp.2159-2164, 1995
- Suyama, M., Ogasawara, N., and Ito, R., "transient temperature variation of injection lasers." *Jap. J. Appl. Phys.*, vol.20, pp.L395-L398, 1981
- Tanaka, K., Wakao, K., Yamamoto, T., Nobuharam, H., and Fujii, T., "Dependence of differential quantum efficiency on the confinement structure in InGaAs/InGaAsP strained-layer multiple quantum well lasers." *IEEE Photo.Tech. Lett.*, vol.5, pp.602-604, 1993
- Taylor, G.W., "A new theoretical approach for the quantum well semiconductor laser," *Prog. Quantum Electron.*, vol.16, pp.73-133, 1992

- Temkin, H., Coblenz, D., Logan, R.A., van der Ziel, J.P., Tanbun-Ek, T., Yadvish, R.D., and Sergent, A.M., "Strained quaternary quantum well lasers for high temperature operation," *Appl. Phys. Lett.*, vol. 63, pp. 2321-2323, 1993
- Temkin, H., Coblenz, D., Logan, R.A., van der Ziel, J.P., Tanbun-Ek, T., Yadvish, R.D., and Sergent, A.M., "High Temperature Characteristics of InGaAsP/InP Laser Structures," *Appl. Phys. Lett.*, vol. 62, pp 2402-2404, 1993
- Thijs, P.J.A., van Dongen, T., Tiemeijer, L.F., and Binsma, J.J.M., "High-Performance $=1.3\mu\text{m}$ InGaAsP-InP Strained-Layer Quantum Well Lasers," *J. Lightwave Tech.*, vol. 12, pp.28-36, 1994
- Thijs, P.J.A., Tiemeijer, L., Binsma, J.J.M., and van Dongen, T., "Progress in Long-Wavelength Strained-Layer InGaAs(P) Quantum-Well Semiconductor Lasers and Amplifiers," *IEEE J. Quantum Electron.*, vol.30, pp.477-499, 1994
- Thompson, G.H.B., *Physics of Semiconductor Laser Devices*(Wiley, New York, 1980), chap.6
- Vail, E.C., Nabiev, R.F., and C.J. Chang-Hasnain, "Temperature Dependence of Light-Current Characteristics of $0.98\text{-}\mu\text{m}$ Al-Free Strained-Quantum-Well Lasers," *IEEE Photon. Tech. Lett.*, vol. 6, pp.1303-1305, 1994
- Wilt, D.P., and Yariv, A., "A self-consistent static model of the double-heterostructure laser," *IEEE J. Quantum Electron.*, vol. QE-17, pp.1941-1949, 1981
- Wu., C., and Yang, E.S., "Physical mechanisms of carrier leakage in DH injection lasers," *J. Appl. Phys.*, vol.49, pp.3114-3117, 1978
- Wu., C.M., and Yang, E.S., "Carrier Transport Across Heterojunction Interfaces," *Solid-State Electron.*, vol. 22, pp.241-248, 1979
- Wu., C.H., Zory, P.S., and Emanuel, M.A., "Characterization of Thin p-Clad InGaAs single-quantum-well lasers." *IEEE Photon. Tech. Lett.*, vol.7, pp.718-720, 1995
- Yano, M., Nishi, H., and Takusagawa, M., "Temperature characteristics of threshold current in InGaAsP/InP double-heterostructure lasers," *J. Appl. Phys.*, vol.51, pp.4022-4028, 1980
- Yano, M., Imai, H., and Takusagawa, M., "Analysis of threshold temperature characteristics for InGaAsP/InP double heterojunction lasers." *J. Appl. Phys.*, vol.52, pp.3172-3175, 1981

- Yariv., A., "Scaling laws and minimum threshold currents for quantum confined semiconductor lasers." *Appl. Phys., Lett.*, vol.53, pp.1033-1035, 1988
- Zah, C.E., Bhat, R., Pathak, B., Caneau, C., Favire, F.J., Andreadakis, N.C., Hwang, D.M., Koza, M.A., Chen, C.Y., and Lee, T.P., "Tensile-strained single quantum well lasers," *Electron. Lett.*, vol.27, pp.1414-1415, 1991
- Zah, C.E., Bhat, R., Pathak, B.N., Favire, F.J., Lin, W., Wang, M.C., Andreadakis, N.C., Hwang, D.M., Koza, M.A., Lee, T.P., Wang, Z., Darby, D., Flanders, D., and Hsieh, J.J., "High-performance uncooled 1.3 μ m Al_xGa_yIn_{1-x-y}As/InP strained-layer quantum-well lasers for subscriber loop applications." *IEEE J. Quantum Electron.*, vol.30, pp.511-522, 1994
- Zeng, X., and Naqwi, A., "far-field distribution of double heterostructure diode laser beams," *Appl. Optics*, Vol. 32, pp.4491-4494, 1993
- Zory, P.S., Reisinger, A.R., Waters, R.G., Mawst, L.J., Zmudzinski, C.A., Emanuel, M.A., Givens, M.E., and Coleman, J.J., "Anomalous temperature dependence of threshold for thin quantum well AlGaAs diode lasers," *Appl. Phys. Lett.*, vol.49, pp.16-18, 1986
- Zou, Y. Osinski, J.S., Grodzinski, P., Dapkus, P.D., Rideout, W.C., Sharfin, W.F., Schlafer, J., and Crawford, F.D., "Experimental study of Auger recombination, gain, and temperature sensitivity of 1.5m compressively strained semiconductor lasers," *J. quantum Electron.*, vol.29, pp.1565-1567, 1993

IMAGE EVALUATION TEST TARGET (QA-3)



APPLIED IMAGE, Inc
1653 East Main Street
Rochester, NY 14609 USA
Phone: 716/482-0300
Fax: 716/288-5989

© 1993, Applied Image, Inc., All Rights Reserved

